WL-TR-93-2061

AD-A270 660

Collaborative Research on Combustion Diagnostics and Modeling between Rolls-Royce Inc. and the United States Air Force Wright Laboratory

Alan Rose
Rolls-Royce Inc.
2849 Paces Ferry Road
Atlanta, Georgia 30339-3769

Experimental Work by:
Saad A. Ahmed
Abdollah S. Nejad
Aero Propulsion and Power Directorate
Wright Laboratory
Air Force Materiel Command
Wright Patterson Air Force Base, Ohio 45433

DTIC
ELECTE
OCT 14 1993
S E D

January 1993

Interim Report for Period 1 May 1990 - 30 November 1992

Approved for Public Release; Distribution is Unlimited

Aero Propulsion and Power Directorate
Wright Laboratory
Air Force Materiel Command
Wright-Patterson Air Force Base, Ohio 45433-7650

93-23610

93 10 6 092

NOTICE

When Government drawings, specifications, or other data are used for any purpose other than in connection with a definitely Government-related procurement, the United States Government incurs no responsibility or any obligation whatsoever. The fact that the government may have formulated or in any way supplied the said drawings, specifications, or other data, is not to be regarded by implication, or otherwise in any manner construed, as licensing the holder, or any other person or corporation; or as conveying any rights or permission to manufacture, use, or sell any patented invention that may in any way be related thereto.

This report is releasable to the National Technical Information Service (NTIS). At NTIS, it will be available to the general public, including foreign nations.

This technical report has been reviewed and is approved for publication.

Abdollah S. Nejad
Experimental Research Branch
Advanced Propulsion Division
Aero Propulsion and Power Directorate

John T. Hojnacki, Chief
Experimental Research Branch
Advanced Propulsion Division
Aero Propulsion and Power Directorate

ROBERT E. HENDERSON, Div Chief
Advanced Propulsion Division
Aero Propulsion & Power Directorate

If your address has changed, if you wish to be removed from our mailing list, or if the addressee is no longer employed by your organization please notify WL/POPT , WPAFB, OH 45433- 7251 to help us maintain a current mailing list.

Copies of this report should not be returned unless return is required by security considerations, contractual obligations, or notice on a specific document.

REPORT DOCUMENTATION PAGE

Form Approved
OMB No. 0704-0188

Public reporting burden for this collection of information is estimated to average 1 hour per response, including the time for reviewing instructions, searching existing data sources, gathering and maintaining the data needed, and completing and reviewing the collection of information. Send comments regarding this burden estimate or any other aspect of this collection of information, including suggestions for reducing this burden, to Washington Headquarters Services, Directorate for Information Operations and Reports, 1215 Jefferson Davis Highway, Suite 1204, Arlington, VA 22202-4302, and to the Office of Management and Budget, Paperwork Reduction Project (0704-0188), Washington, DC 20503.

1. AGENCY USE ONLY *(Leave blank)*

2. REPORT DATE
January 1993

3. REPORT TYPE AND DATES COVERED
Interim 1 May 1990 to 30 Nov 1992

4. TITLE AND SUBTITLE
Collaborative Research on Combustion Diagnostics and Modeling Between Rolls-Royce Inc. and the United States Air Force Wright Laboratory

5. FUNDING NUMBERS
C-F33615-90-C-2092
PE-61101
PR-2308
TA-S1
WU-XY

6. AUTHOR(S)
A. Rose

7. PERFORMING ORGANIZATION NAME(S) AND ADDRESS(ES)
Rolls-Royce Inc.
2849 Paces Ferry Rd.
Atlanta,
GA 30339-3769

Aero Propulsion and Power Directorate
Wright Laboratory
Air Force Materiel Command
WPAFB, OH 45433-7650

8. PERFORMING ORGANIZATION REPORT NUMBER

9. SPONSORING/MONITORING AGENCY NAME(S) AND ADDRESS(ES)
Aero Propulsion and Power Directorate
Wright Laboratory
Air Force Materiel Command
WPAFB, OH 45433-7650

10. SPONSORING/MONITORING AGENCY REPORT NUMBER
WL-TR-93-2061

11. SUPPLEMENTARY NOTES

12a. DISTRIBUTION/AVAILABILITY STATEMENT
Approved for public release; distribution is unlimited.

12b. DISTRIBUTION CODE

13. ABSTRACT *(Maximum 200 words)*

Diagnostic techniques are employed to investigate flows typical of a gas turbine combustor with the aim of furthering the understanding of the complex physical and chemical processes involved and using this understanding in validating and developing combustion Computational Fluid Dynamic (CFD) codes.

Detailed measurements of velocities and Reynolds stresses have been made with a Laser Doppler Velocimeter (LDV) in an axisymmetric combustor with a strongly swirling, isothermal, turbulent flow. Anomolies identified in the initial measurements were attributed to LDV signal noise problems caused by reflections off the internal combustor walls. Future LDV measurements will be taken along a vertical diameter within the combustor to minimize these noise problems.

Comparisons of the isothermal measurements with CFD predictions are presented and discussed. Both a Reynolds Stress Transport Model (RSTM) and a $k-\epsilon$ turbulence model have been employed. The RSTM out performs the $k-\epsilon$ model for this strongly swirling flow. Although the $\overline{v'w'}$ shear stress could not be measured with the current combustor configuration, the results from the modeling illustrate the important role played by the $\overline{v'w'}$ shear stress in defining the nature of the swirling flow. A new Rolls-Royce designed and manufactured water-cooled combustor, with enhanced optical access will permit the simultaneous measurement of all velocity components and all Reynolds stresses. Details of this new test section are presented.

14. SUBJECT TERMS
LDV, CFD, CARS, Flame Stabilization, Combustor Design, Swirl Swirling Flame, Turbulence, Combustion.

15. NUMBER OF PAGES
117

16. PRICE CODE

17. SECURITY CLASSIFICATION OF REPORT	18. SECURITY CLASSIFICATION OF THIS PAGE	19. SECURITY CLASSIFICATION OF ABSTRACT	20. LIMITATION OF ABSTRACT
Unclassified	Unclassified	Unclassified	UL

NSN 7540-01-280-5500

Standard Form 298 (Rev. 2-89)
Prescribed by ANSI Std. Z39-18
298-102

DTIC QUALITY INSPECTED 2

Accesion For
NTIS CRA&I ☒
DTIC TAB ☐
Unannounced ☐
Justification
By
Distribution /
Availability Codes
Dist | Avail and / or Special
A-1

Contents

Figures v

Tables vii

Preface viii

Nomenclature ix

1 Introduction 1

2 Rig Development 3
- 2.1 Imperial College Quartz Tube Combustor Rig 3
- 2.2 Wright Laboratory Isothermal Plexiglas Combustor Rig 4
  - 2.2.1 Swirler 7
  - 2.2.2 Gaseous Fuel Injector 10
- 2.3 Wright Laboratory Water-Cooled Combustor Rig 10
- 2.4 New Rolls-Royce Designed Test Section 16
- 2.5 Rig Operating Conditions 20

3 Instrumentation 22
- 3.1 Laser Velocimeter 22
- 3.2 Data Acquisition and Analysis 22
- 3.3 Coherent Anti-Stokes Raman Spectroscopy (CARS) 23

4 Fluid Dynamic Equations and CFD Modeling 24
- 4.1 Mean Flow Equations 26
  - 4.1.1 Uniform-Density Turbulent Flow 26
  - 4.1.2 Variable Density Turbulent Flow 27
  - 4.1.3 The Reynolds Stress Equations 28
  - 4.1.4 The Scalar Flux Equations 29
- 4.2 Turbulence Closure 29
  - 4.2.1 The Eddy-Viscosity Hypothesis 29
  - 4.2.2 The $k - \epsilon$ Model 30
  - 4.2.3 The Reynolds Stress Equation Closure 32
  - 4.2.4 Scalar Flux Equation Closure 36

5 Experimental Results 41
- 5.1 Isothermal LDV 41
- 5.2 Flow Instabilities 49
- 5.3 Combustion LDV 50

6 CFD Isothermal Comparisons 53

7 Program 62

8 Conclusions 71

A Conventially Averaged Equations for Constant Density Flows 76

B Isothermal CFD Predictions - Complete Results 77

List of Figures

1 The Imperial College Quartz Tube Combustor Rig 4
2 Schematic of Plexiglas Combustor 5
3 Plexiglas Combustor - Test Section 6
4 Swirl Vane Geometry 8
5 Schematic of Swirler Geometry 8
6 Fuel Injector and Swirler Assembly — Air In 9
7 Fuel Injector and Swirler Assembly — Air Out 9
8 Fuel Injector — Components 11
9 Fuel Injector — Exploded View 11
10 Wright Laboratory Combustor Facility in Building 18 12
11 Water–Cooled Stainless Steel Combustor 12
12 Water–Cooled Stainless Steel Combustor and LDV Mounted on xyz table 13
13 Schematic Detail of Swirler/Injector Housing Assembly 14
14 Swirler Housing Assembly — Air In 14
15 Swirler Housing Assembly — Air Out 15
16 New Hot Test Section – Rotating Drum and Laser Diagnostics Access, Showing 3 Velocity Component Measurements along a Vertical Radius 17
17 New Hot Test Section - Sealed Measurement Box 19
18 New Hot Test Section (Rolls-Royce Design) 20
19 Wall Distances in Function f_l 35
20 Comparison of Axial Velocity Data Measured Along a Horizontal and a Vertical Combustor Radius 41
21 Schematic of LDV Measurement Noise Problem 42
22 Comparison of Mass Flow Rates Calculated — LDV Data and Flowmeter Measurements 43
23 Measured Mean Axial Velocity at Various Axial Stations 44
24 Measured Mean Radial Velocity at Various Axial Stations 44
25 Measured Mean Swirl Velocity at Various Axial Stations 47
26 Measured Turbulent Axial Velocity at Various Axial Stations 47
27 Measured Turbulent Radial Velocity at Various Axial Stations . . . 48
28 Measured Turbulent Swirl Velocity at Various Axial Stations 48
29 Investigation of Dominant Frequency in Combustor with Changing Combustor Length 49
30 Change in Amplitude of Dominant Combustor Frequency with Changing Equivalence Ratio 50
31 LDV Combustion – Measurement Locations (Gould and Benedict) . 51
32 Measured vs. Predicted - Selected Axial Velocity Profiles 55
33 Measured vs. Predicted - Selected Radial Velocity Profiles 55

34 Measured vs. Predicted - Selected Swirl Velocity Profiles 57
35 Measured vs. Predicted - Selected Axial Reynolds Stress Profiles . . 57
36 Measured vs. Predicted - Selected Radial Reynolds Stress Profiles . 58
37 Measured vs. Predicted - Selected Swirl Reynolds Stress Profiles . . 58
38 Measured vs. Predicted - Selected Kinetic Turbulence Energy Profiles 59
39 Measured vs. Predicted - Selected Axial/Radial Reynolds Shear Stress Profiles 59
40 Measured vs. Predicted - Selected Axial/Swirl Reynolds Shear Stress Profiles 60
41 Measured vs. Predicted - Selected Radial/Swirl Reynolds Shear Stress Profiles 60
42 Actual Schedule Achieved — May to December 1990 63
43 Actual Schedule Achieved — January to June 1991 64
44 Actual Schedule Achieved — July to December 1991 65
45 Actual Schedule Achieved — January to June 1992 66
46 Actual Schedule Achieved — July to December 1992 67
47 Anticipated Schedule — 1993 70
48 Anticipated Schedule — 1994 70

List of Tables

1 Summary of Rig Operating Conditions 21
2 Diagnostics Employed 21
3 Constants Employed in $k - \epsilon$ Model 32
4 R_{ij} terms in Reynolds–Stress Equations 37
5 R_{ic} terms in the Scalar Flux Equations 39
6 Constants Employed in the Reynolds Stress Transport Model (RSTM) 40

Preface

This Interim report covers the technical effort conducted under Air Force Contract No. F33615-90-C-2092, entitled *Combustion Diagnostics and Modeling* between May 1990 and November 1992. All research done under this contract was administered under the direction of Dr. A.S. Nejad, Project Engineer, Aero Propulsion and Power Directorate, Air Force Wright Laboratory, Wright-Patterson Air Force Base, Ohio, and Mr. A. Veninger, Manager, Rolls-Royce Inc.

The author wishes to thank Dr. A.S. Nejad, Dr. S.A. Ahmed and Mr. C. Smith for their technical assistance and support. The author also wishes to acknowledge and thank Mr. K. Pesyna for his hard work in designing the new test section and providing the drawings incorporated in this report.

Nomenclature

Symbols	Definition
$\overline{C}$	Unweighted mean concentration of a general scalar
$\tilde{C}$	Density-weighted mean concentration of a general scalar
C_{ij}	Convection of Reynolds-stresses
C_{ija}	Algebraic contributions to the convection of the Reynolds-stresses
C_μ	Coefficient in the $k-\epsilon$ turbulence model
C_1, C_2, C_3, C_{p1}, C_{p2}, C_k, C_ϵ, $C_{\epsilon 1}$, $C_{\epsilon 2}$, $C_{\epsilon 3}$	Constants in turbulent-velocity-field related equations
C_{c1}, C_{c2}, C_{c3}, C_c, C_d, C_{g1}, C_{g2}	Constants in turbulent-scalar-field related equations
G	Turbulence energy generation
G_θ	Angular momentum flux
G_x	Axial momentum flux
L	Length scale
N	Number of events; Number of swirler blades
$\overline{P}$	Mean pressure
P'	Turbulent pressure fluctuation about mean
P_{ij}	Production of the Reynolds-stresses
P_{ic}	Production of the Scalar-fluxes
R	Radius of curvature of swirler blade
R_{ic}	Additional Scalar-flux equation convection, production and diffusion terms arising from transformation to axisymmetric coordinate system
R_{ij}	Additional Reynolds-stress convection, production and diffusion terms arising from transformation to axisymmetric coordinate system
S	Swirl number
S_c	Scalar source terms
U	x-direction velocity component
$\overline{U_i}$	Unweighted mean flow velocity components
$\tilde{U}_i$	Density-weighted mean flow velocity components
V	r-direction velocity component
Vol	Volumetric value of finite-volume
W	Swirl (θ-direction) velocity component
$W(t)$	Weighting factor

d	Diameter of swirler blade station
d_i	Inner swirler hub diameter
d_{ic}	Diffusion of the Scalar–fluxes
d_{ij}	Diffusion of the Reynolds–stresses
d_o	Outer swirler–hub diameter
f_l	Wall–distance function
k	Turbulence kinetic energy
l	Mixing length
m	Mass flow rate
m_a	Mass flow rate of air
m_{fu}	Mass flow rate of fuel
n_i	Unit vector
r	Radial coordinate.
t	Time
u_i'	Turbulent velocity fluctuation about unweighted mean
u_i''	Turbulent velocity fluctuation about density weighted mean
$\overline{u_i'u_j'}$	Unweighted Reynolds–stresses
$\overline{u_i''u_j''}$	Density–weighted Reynolds–stresses
$\overline{u_i'u_c'}$	Unweighted scalar–flux (general scalar)
$\overline{u_i''u_c''}$	Density–weighted scalar–flux (general scalar)
x	Axial coordinate
x_i	Spatial coordinate system
y	Cross–stream coordinate
Γ	Diffusion coefficient
Φ	General variable; Equivalence ratio
Φ_{ij}	Redistribution of the Reynolds–stresses
Φ_{ic}	Pressure/scalar–gradient interaction terms
Φ_{ic1}	Turbulence part of Φ_{ic}
Φ_{ic2}	Mean–strain part of Φ_{ic}
Φ_{ic3}	Additional pressure–driven contribution to Φ_{ic} (variable–density flows only)
Φ_{ij1}	Turbulence part of Φ_{ij}
Φ_{ij2}	Mean–strain part of Φ_{ij}
Φ_{ij3}	Additional pressure–driven contribution to Φ_{ij}
Φ_{ijw}	Wall reflection term in Φ_{ij}
δ_{ij}	Kronecker delta
ϵ	Turbulence energy dissipation rate
ϵ_{ij}	Dissipation of the Reynolds–stresses
ϵ_{ic}	Dissipation of the Scalar–fluxes
κ	Von Karman constant
μ	Dynamic viscosity
μ_t	Turbulent viscosity
$\overline{\rho}$	Mean density

ρ'	Turbulent density fluctuation about mean
σ	Prandtl number; standard deviation

Subscripts

a	Air
c	Scalar quantity
cl	Centerline
ct	Turbulent scalar
fu	Fuel
ij	Component corresponding to index i and j
k	Turbulence kinetic energy
r	Radial coordinate
t	Turbulent
x	Axial coordinate
θ	Circumferential coordinate
Φ	General variable
ϵ	Turbulence energy dissipation rate
ρ	Density
∞	Infinity

Superscripts

$-$	Unweighted average
$\tilde{}$	Mass-weighted or Favre average
$'$	Unweighted fluctuation
$''$	Mass-weighted or Favre fluctuation

Acronyms

AEDC	Arnold Engineering Development Center
BSA	Burst Spectrum Analyser
CARS	Coherent Anti-Stokes Raman Spectrosropy
CFD	Computational Fluid Dynamics
ID	Inner Diameter
LDV	Laser Doppler Velocimeter/Velocimetry
OD	Outer Diameter
PACE	Rolls-Royce Combustion CFD Code
PVC	Precessing Vortex Core
RSTM	Reynolds Stress Transport Model
SGI	Silicon Graphics Workstation
SRL	Scientific Research Laboratories
USAF	United States Air Force
WL	Wright Laboratory
WPAFB	Wright-Patterson Air Force Base

1 Introduction

Rolls-Royce has spent over two decades developing computational fluid dynamic (CFD) computer codes that describe the complex physics and chemistry in a gas turbine engine combustion chamber. The development of these codes has always depended on comparisons and analysis of the predictions with key aerodynamic and chemical constituency measurements. The hostile environment of the combustor has rendered intrusive measurements of the combusting flow field extremely difficult. Additionally, intrusive measurements by definition create distortions in the flow field, characteristic of the probe design.

Nonintrusive laser based measurement systems such as those developed and in use by the Air Force Wright Laboratory (WL) offer the potential to make in situ detailed measurements of a combusting flow field that would allow further understanding of the combustion process and upgrades to and validation of CFD codes in general. While typical laboratory flames were used during the development of these diagnostic systems, application of laser based instrumentation to more complicated combustor systems has been sought recently.

From technical exchanges between Rolls–Royce engineers and WL scientists this research collaboration was initiated to complement the use and development of CFD codes and laser diagnostics and thereby provide the benefit of a mutually improved understanding of combustion phenomena as applied to gas turbine engines. Rolls-Royce brings to this collaboration the types of combustion experiments, the corresponding measurements and analytical modeling required to bring about this improved understanding in a realistic manner consistent with gas turbine engine company experience. The Wright Laboratory provides instrumentation, rig facilities and many years of experience with such laser based diagnostic systems.

Section 2 describes the development of the experimental rigs. The combustor configuration is based on a design originally employed at Imperial College London, England. The benefits of this design are discussed and extended to the facilities made available at the Wright Laboratory. Two separate test sections have been employed at the Wright Laboratory, namely, the Plexiglas section for isothermal work and the water–cooled, stainless steel section for the hot flow investigations. The actual combustor configurations are presented including details on the swirler and gaseous fuel injector design. A new test section designed by Rolls-Royce Inc. which permits optical access for a three component LDV system for measurements in combusting flows at chamber pressures of up to 3 *atm.* has been built under contract. This section is currently being installed at the WL facility. The design was financed by Rolls-Royce Inc. and the manufacture was financed by the Wright Laboratory. This section is completed with a summary of the rig operating conditions.

Section 3 presents the nonintrusive, laser diagnostic instrumentation employed. The two–component Laser Doppler Velocimetry (LDV) equipment is described. Further instrumentation, such as the Coherent Anti–Stokes Raman Spectroscopy

(CARS) system has been built and is currently being calibrated. This will permit measurement of temperature and the concentrations of major species.

Section 4 introduces the equations typically employed in CFD modeling using PACE, the Rolls-Royce CFD code as an example. Numerical procedures are not discussed since these vary with the implementation of different CFD codes, whereas, the equations remain the same. The general mean flow equations are presented and the problem of turbulence closure is introduced.

Section 5 presents experimental results from isothermal work and some initial combustion LDV results. Some combustor instability problems were initially observed and later addressed. The combustion LDV measurements were taken as part of a summer faculty program at the Wright Laboratory and are not complete. However, the results have served an excellent purpose in raising particular experimental difficuties involved in making these kind of measurements in such a hostile flow in this configuration.

Section 6 shows the initial CFD comparisons with the isothermal measurements presented in Section 5. The CFD results with the Reynolds Stress Transport Model (RSTM) and the $k - \epsilon$ model are compared. No combustion modeling is presented in this report.

Section 7 summarizes the schedule achieved to date, discussing causes for delay in comparison to the originally defined schedule. This section finishes with a proposed schedule for the next 24 months, up to the termination of the present contract.

Section 8 concludes this report by drawing together the work done so far and how this will be used in guiding the remaining program.

2 Rig Development

This section introduces the original rig configuration intended for this work and its subsequent development as the research has progressed. Rolls-Royce has had much experience with a quartz tube combustor rig developed at Imperial College, London, England, see Wilhelmi [1]. The original intention in this collaborative research program was to use the Wilhelmi quartz tube combustor in the Wright Laboratory Facility. However, for various reasons which are outlined in Section 2.1, this was not viable, so an alternative combustor facility at the Wright Laboratory was employed and subsequently developed.

The alternative facilities included a Plexiglas rig suitable only for isothermal work and a dimensionally similar stainless steel water-cooled combustor for reacting flows. The Plexiglass rig employed a test section that permitted measurement of all three velocity components (although not simultaneously), whereas the stainless steel rig had very limited optical access which only permitted measurement of the axial and swirl velocities in both hot and cold flows, which has proved insufficient for CFD validation data.

After completion of the isothermal phase of the program it became apparent that effort should be expended in providing a test section that could provide all of the necessary data for both cold and hot flow cases. Thus, Rolls-Royce undertook and financed the design of a new test section that would combine the advantages of the Plexiglass rig and the stainless steel rig, that is, full optical access for the simultaneous measurement of all three velocity components and all of the Reynolds stresses in both hot and cold flows. Furthermore, the test section was designed to accomodate the new CARS system. This was achieved in a way that would allow the CARS and LDV systems to operate in a fully coupled fashion. This would provide the potential for simultaneous measurement of the velocities, Reynolds stresses, temperatures and species concentrations at chamber pressures up to $3atm$. The fabrication of the test section was financed by Wright Laboratory under this contract. Details of the new test section are presented in Section 2.4.

2.1 Imperial College Quartz Tube Combustor Rig

The design of the Imperial College combustor rig, Wilhelmi [1], was optimized to provide good optical access for laser diagnostic equipment yet provide a turbulent, strongly swirling flow typical of a gas turbine combustor. This led to the use of a quartz tube to confine the flow, thus, providing an axisymmetric can type combustion chamber, shown schematically in Figure 1. The use of the quartz tube, however, limited the tests to atmospheric pressures.

Essentially, the rig comprises a quartz tube supported between two flanges connected together by a series of tie bars. The air is introduced through the head flange by a built-in aerodynamic vaned swirler of $42mm$ outer diameter and a $21mm$ hub diameter. The swirler has 20 vanes with an angle of 45°. The fuel injector is lo-

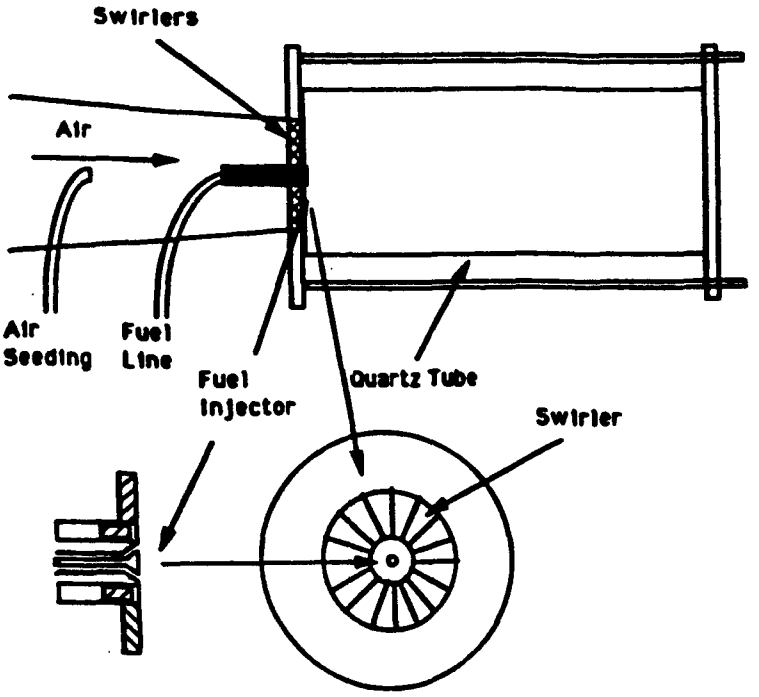

Figure 1: The Imperial College Quartz Tube Combustor Rig

cated in the center of the swirler. It is intended for gaseous propane and incorporates an annular slot of $0.9mm$ width through which fuel is injected in a conical sheet with a 90° included angle. Details of the swirler and fuel injector are discussed in Section 2.2 where they were scaled up and rebuilt in order to fit into the Wright Laboratory facility in Building 18. The temperature of the quartz tube wall was maintained below the limit of 1100°C by a cooling air film on the outside of the wall which issued from slots in the upstream flange.

Some difficulties were encountered during the operation of the quartz tube combustor. Measurements within $10mm$ from the tube walls were not possible due to optical effects caused by the curvature of the quartz wall and when measuring the radial velocity along a vertical radius in the quartz tube, the laser beams were deflected asymmetrically, causing some uncertainty in the exact position of the probe volume. Furthermore, it was observed that the seeding material caused scatches on the inside of the quartz tube which consequently needed regular cleaning and buffing. A limitiation in the operation of the quartz tube combustor was that all of the experiments were conducted at atmospheric chamber pressures for safety reasons.

2.2 Wright Laboratory Isothermal Plexiglas Combustor Rig

Since it was not practical to use the quartz tube combustor section described in Section 2.1, the research team decided to employ the combustor facility in Building 18 at the Advanced Aero Propulsion Division (WPAFB). This facility employed a stainless steel water-cooled combustion chamber of $151.2mm$ diameter, previously used by Wright Laboratory to study premixed gaseous flames, Ahmed et al. [2].

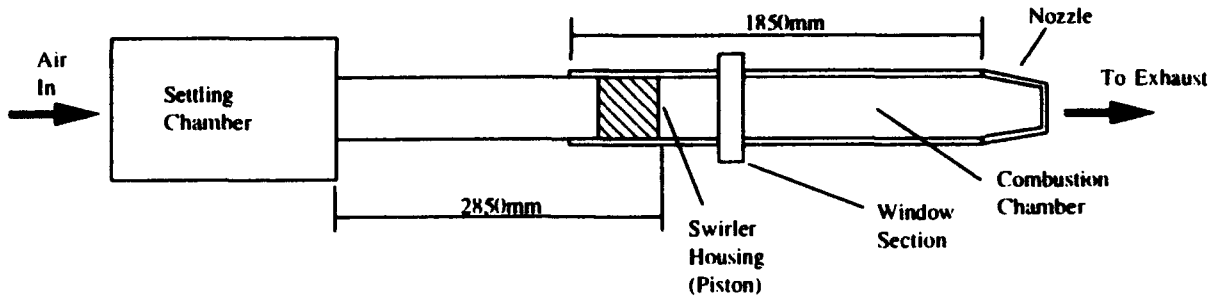

Figure 2: Schematic of Plexiglas Combustor

During initial isothermal measurements, mass flow anomalies were detected when the values derived from the integrated axial velocity profiles were compared with the flowmeter measurements. Consequently, these isothermal measurements were repeated in a dimensionally similar rig made of Plexiglass, which was the original prototype to the stainless steel water–cooled rig. This Plexiglas rig was previously employed by Wright Laboratory for studying confined isothermal swirling flows, Nejad et al. [3]. Using the Plexiglass test section enabled more detailed measurements and eventually helped to address the mass flow anomolies.

The specially designed optical test section employed in the isothermal combustor rig allowed measurement of all three velocity components, normal stresses and two shear stresses with a simultaneous two–component LDV system. This rig comprised two parts, namely, the inlet assembly and the combustion chamber, see Figure 2. The inlet assembly consisted of a $300mm$ diameter settling chamber, a Plexiglas inlet pipe ($2850mm$ in length and $101.6mm$ ID), and a cylindrical Teflon swirler housing ($104.5mm$ ID, $152.4mm$ OD, and $154mm$ in length). A transition section which enabled the swirler to be mounted, was incorporated in this housing. In order to examine the characteristics of the flow upstream of the swirler with LDV (when the fuel injection system is not mounted), a flat $38 \times 38mm$, optical quality, quartz window was installed in the inlet pipe $50.8mm$ upstream of the swirler housing, Figure 3a. The window was replaced by a plug with the same radius of curvature as the inlet pipe when measurements in the combustor were performed, thereby eliminating inlet flow disturbances. A unique feature of the design was the capability of positioning the dump plane (swirler housing) relative to the measurement station in the combustion chamber. This was accomplished by supporting the entire inlet assembly on a traversing mechanism controlled by a stepping motor. Throughout the experiments, the inlet average velocity (assuming simple plug flow across the pipe) was monitored with a flowmeter located far upstream of the swirler housing.

The combustion chamber section consisted of a Plexiglas tube ($152.4mm$ ID and $1850mm$ in length) terminating into a larger pipe (exhauster). The measurement

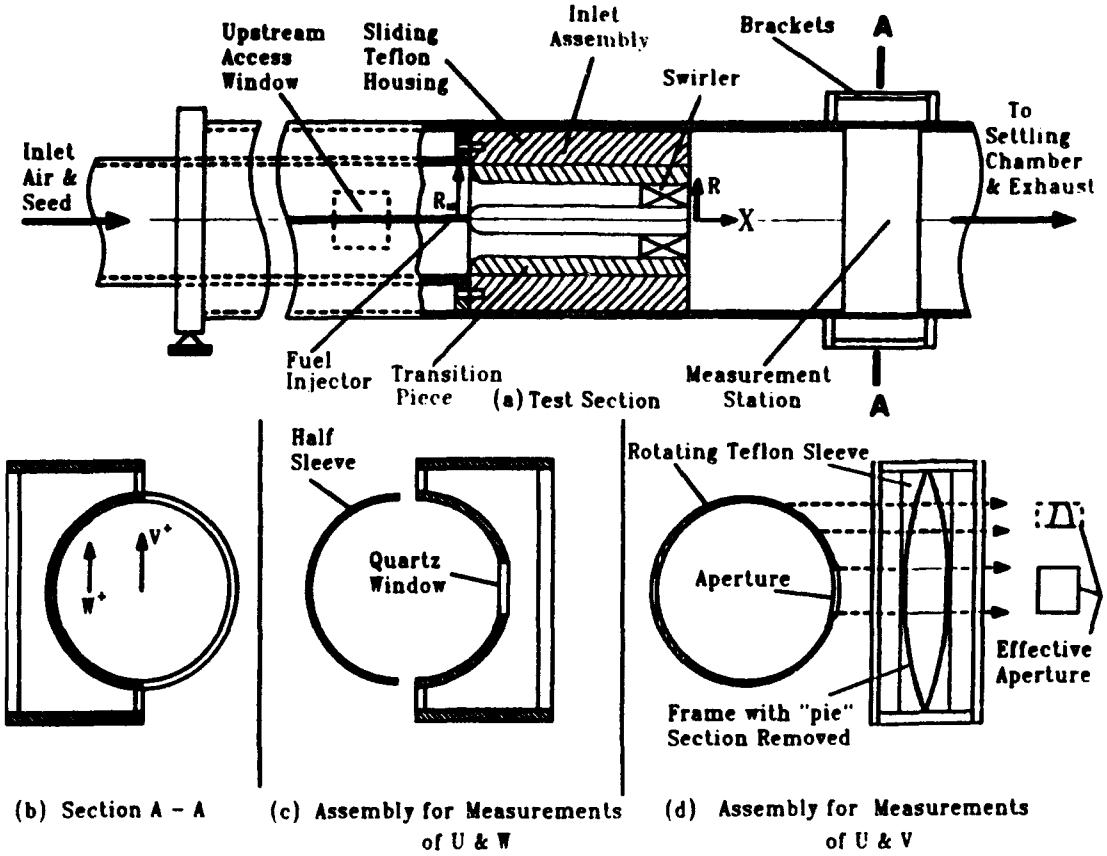

Figure 3: Plexiglas Combustor - Test Section

station, Figure 3, was designed to accept two different window assemblies. One was designed to provide optical access for traversing in the horizontal plane along the combustor diameter. The second window assembly was designed for traversing in the vertical plane along the combustor diameter. By traversing a two component LDV system in the vertical and horizontal planes, the three components of the velocity vector can be realized, Figure 3b. However, this would be done during two entirely separate experiments carefully maintaining the same running conditions and "melding" the results on the assumption of axisymmetry. The common factor between these necessary two experiments is the axial velocity, which is closely monitored to check the running conditions and ensure the validity of the axisymmetric flow assumption. This test section together with the two component LDV is not capable of measuring the $\overline{v'w'}$ shear stress.

Although the Plexiglas combustor makes efficient use of the two component LDV system, the preferred option would be the use of a fully simultaneous three component LDV system. This would enable measurement of all of the velocities and Reynolds stresses (including $\overline{v'w'}$) at the same time and same point in space. A new test section would be required in order to admit a third laser beam. Such a test section has now been made, see Section 2.4.

The current experiments were conducted with a 40% contraction nozzle at the combustor exit. There is also a plug assembly at the combustor exit that may be inserted in order to increase the chamber pressure (for the same mass flow).

Figure 3c shows the experimental setup when velocity measurements were made in the horizontal plane. This assembly consisted of a flat 38x38mm optical quality

quartz window installed in a frame fabricated from 152.4mm ID Plexiglas. The frame was bonded to two brackets and attached to the combustor section as shown in Figure 3a. A 40mm–wide half–sleeve, fabricated from 152.4mm ID Teflon, was located in the combustor wall recess to ensure a smooth flow passage. The whole assembly was sealed with vacuum grease to prevent leakage. Figure 3d shows the arrangement for performing velocity measurements in the vertical plane. This assembly consisted of a frame, fabricated from 154.4mm ID Plexiglas, with an elliptically shaped section removed from it, and a rotating Teflon sleeve, 40mm wide, 2mm thick and 152.4mm ID, with a $30 \times 20mm$ centrally located rectangular aperture. The assembly was mounted in the combustor section as described previously. The frame/sleeve combination provided the minimum optical access opening as the LDV was traversed in the vertical plane, while simultaneously minimizing flow disturbance.

2.2.1 Swirler

The swirler geometry was based on the design employed by Wilhelmi [1]. However, the Wright Laboratory Plexiglas combustor described in Section 2.2 has a diameter of 152.4mm, compared to the quartz tube combustor diameter of 101.6mm. Thus, in order to retain similarity between the two research programs, the ratio of the swirler diameter to the combustor diameter was kept the same for the new swirler design, that is, the new swirler diameter was scaled up by a factor of 1.5 from that used by Wilhelmi [1]. In order to maintain similarity in the velocity fields, it was also appreciated that the mass flow rates should be scaled up by a factor of 2.25 from those values used by Wilhelmi [1]. The rig operating conditions are summarized later in Section 2.5.

The aim of the swirler design is to provide a mean airflow turning angle of 45°. To achieve this with a constant radial profile, constant vane chord and no twist, for ease of manufacture, the design procedure of Buckley et al. [4] was employed. The equation used to calculate the required radius of curvature was:

$$\theta\left(\frac{cN}{\pi d}\right)^{\frac{1}{2}} + \left(2\sin^{-1}\frac{c}{2R}\right)\left[0.21 + 0.002\sin^{-1}\frac{c}{2R} - \left(\frac{cN}{\pi d}\right)^{\frac{1}{2}}\right] = 0 \qquad (1)$$

where, c is the blade chord, N is the number of blades in the swirler assembly, θ is the mean airflow turning angle, R is the radius of curvature of the blade and d is the diameter at the specified blade station, see Figure 4.

An optimum value of $R = 40.5mm$ was calculated with the use of a spreadsheet using the following values $c = 34.5mm$ $N = 20$ $\theta = 45°$ $d = 31.5 \rightarrow 63mm$, that is, values varying from the inner to the outer swirler hub diameters.

Figure 5 shows a schematic of the swirler and Figures 6 and 7 show the fuel-injector/swirler assembly. Swirl strength is generally characterized by the swirl number S, which for unconfined flows is defined as the ratio of the angular momentum flux to the axial momentum flux multiplied by some characteristic length scale

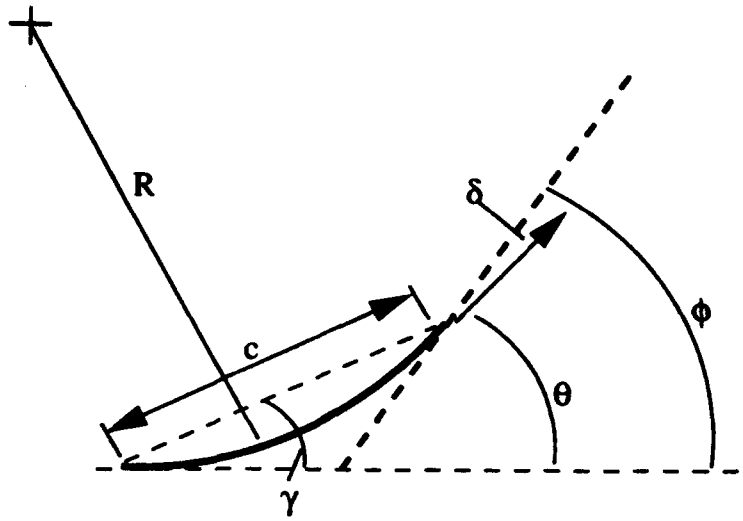

Figure 4: Swirl Vane Geometry

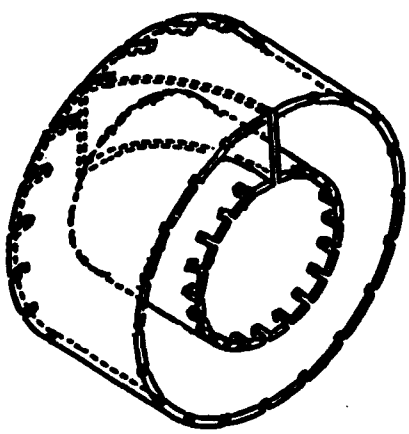

Swirler length	= 31.5mm
Vane radius	= 40.0mm
Vane thickness	= 0.76mm
Inner hub OD	= 35.1mm
Outer hub ID	= 61.0mm

Figure 5: Schematic of Swirler Geometry

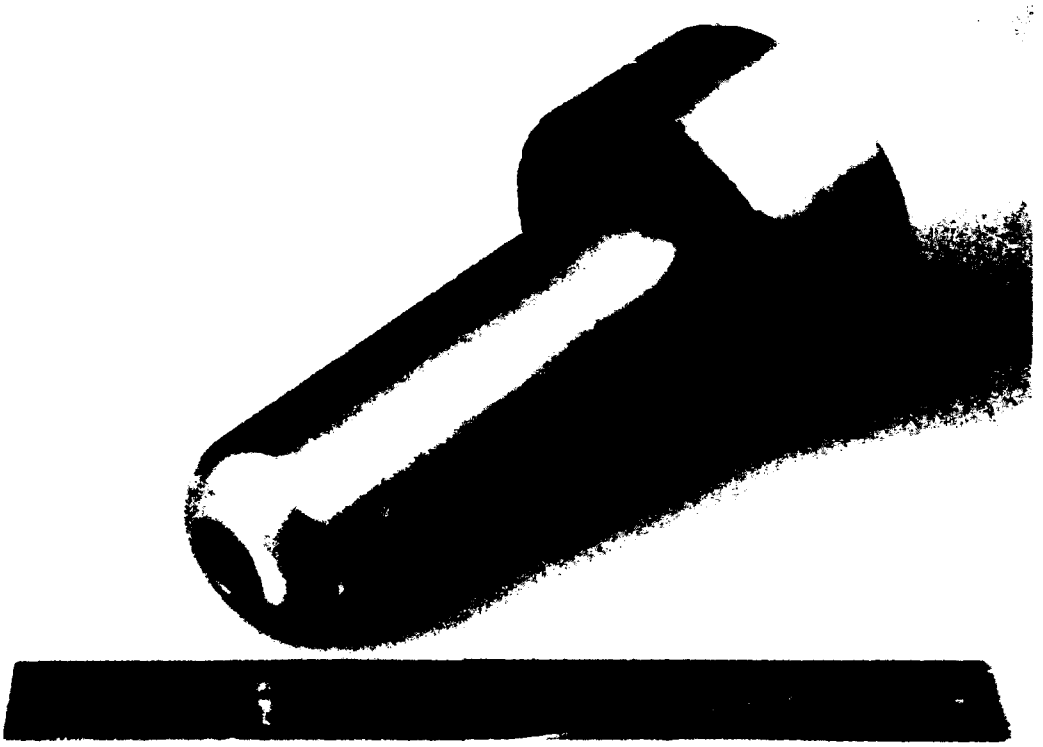

Figure 6: Fuel Injector and Swirler Assembly — Air In

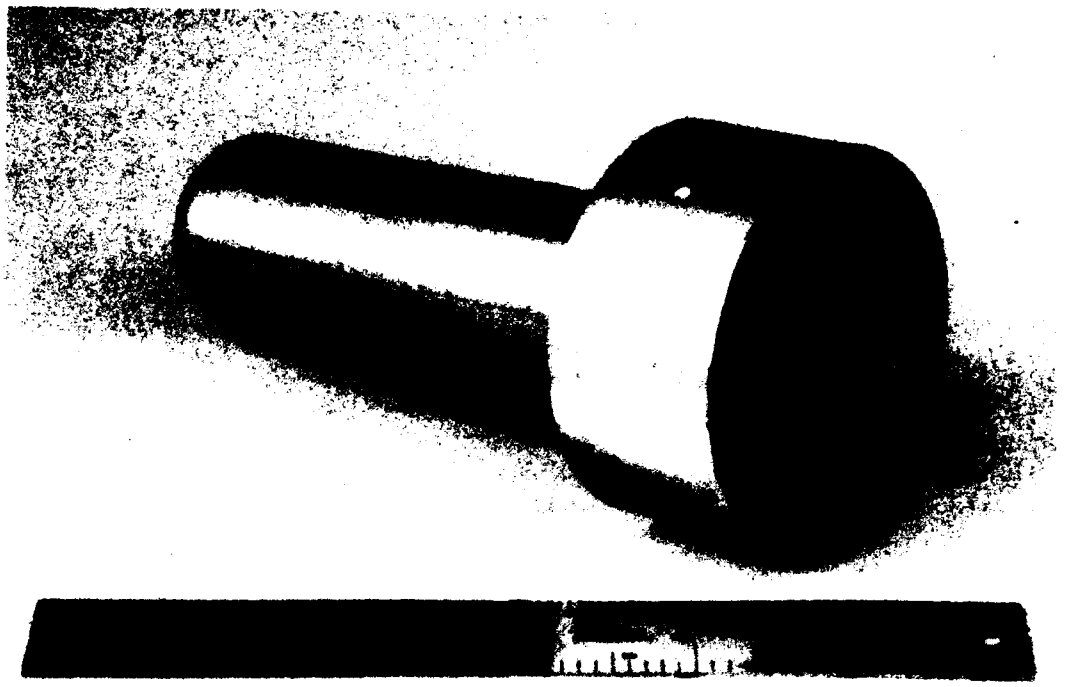

Figure 7: Fuel Injector and Swirler Assembly — Air Out

L (in this study, the swirler OD):

$$S = \frac{G_\theta}{G_x L} \tag{2}$$

It has been suggested by Beer and Chigier [5], that the swirl number is only dependent on the swirler geometry. For an annular swirler with an inner hub diameter d_i, outer hub diameter d_o and a constant swirl vane angle θ:

$$S = \frac{2}{3}\left[\frac{1-\left(\frac{d_i}{d_o}\right)^3}{1-\left(\frac{d_i}{d_o}\right)^2}\right]\tan\theta \tag{3}$$

this expression takes no account of the radial pressure gradient or the turbulent stress terms. The swirler employed in this study does not have a constant vane angle, however, if the mean airflow turning angle of 45° is used for the value of θ, we can calculate a swirl number of 0.81 compared to a swirl number of 0.78 employed by Wilhelmi [1].

2.2.2 Gaseous Fuel Injector

Propane is being used as the fuel in this research program to avoid laser diagnostic problems associated with fuel spray droplets and sooting. However, it is anticipated that a liquid fuel such as kerosene will be investigated in the future.

Figures 8 and 9 show the detail of the fuel injector components. A modular approach to the fuel injector design was employed. The bluff body 90° cone injector exit can easily be replaced with an alternative design. This "pintle" can be centrally aligned with the use of three small grub screws or inserted further into the injector body if higher fuel penetration velocities are required. The fuel settling chamber shown with eight small drilled holes can also be replaced, for example, by a unit designed to impart swirl to the fuel prior to injection.

2.3 Wright Laboratory Water–Cooled Combustor Rig

The Plexiglas rig and the water-cooled rig are dimensionally identical and operate in the same manner. However, the water-cooled rig does not employ the same optical test section and thus, only two velocity components, two normal stresses and one shear stress may be measured with the same two-component LDV system on this rig. The water cooled rig was previously used by Wright Laboratory for studying gaseous premixed flames, see Ahmed et al [2]. A new fuel supply line had to be installed coaxial to the swirl air supply line to enable the study of turbulent diffusion flames, required for this research program.

Figure 10 gives an overall view of the Wright Laboratory combustor facility in Building 18. Figure 11 shows the actual combustor and Figure 12 shows the combustor rig with the LDV mounted on an xyz table. As in the Plexiglas rig described

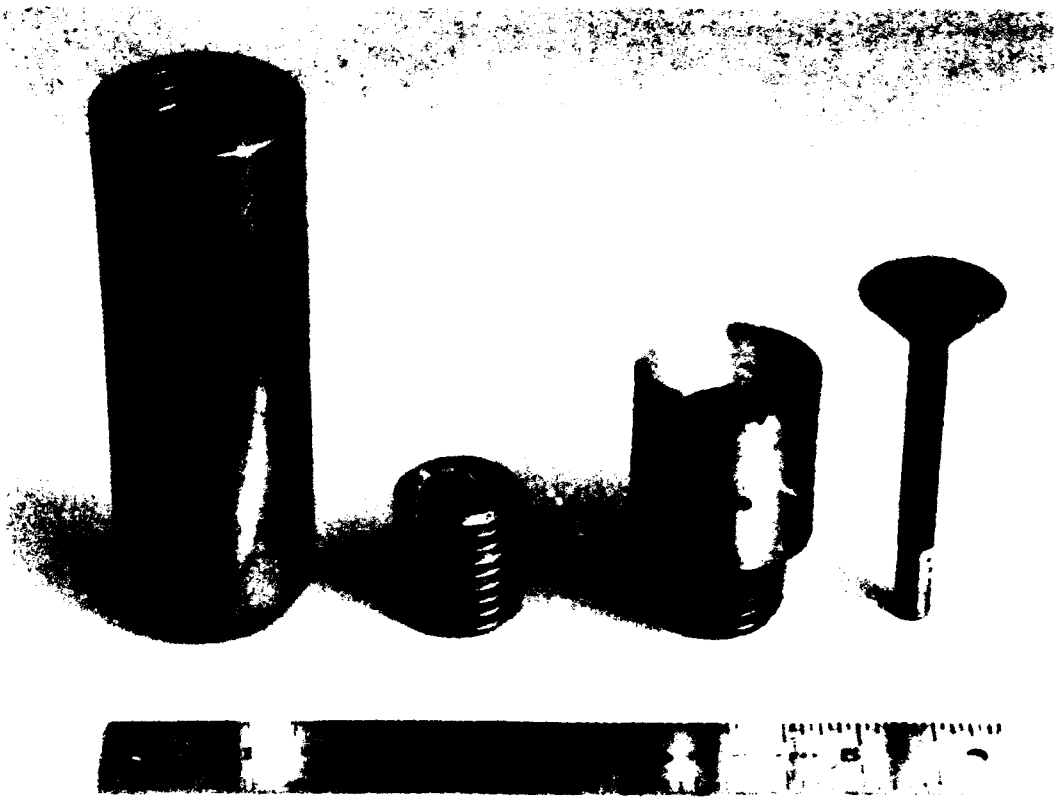

Figure 8: Fuel Injector — Components

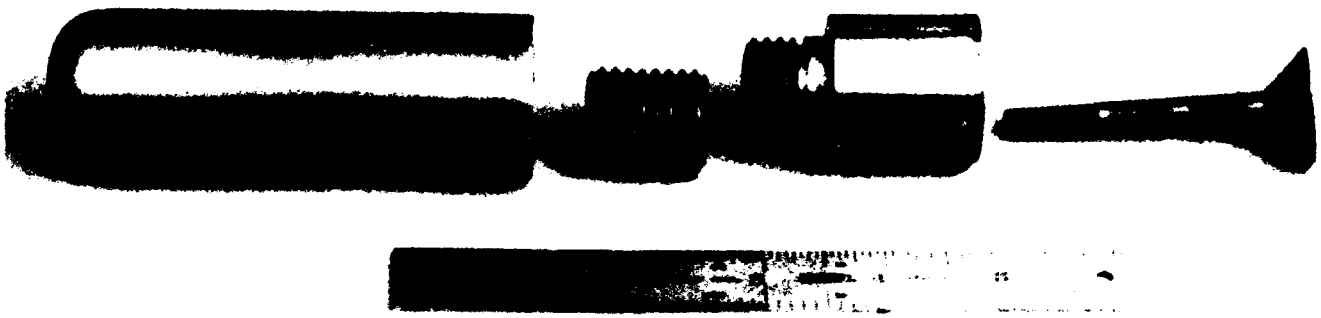

Figure 9: Fuel Injector — Exploded View

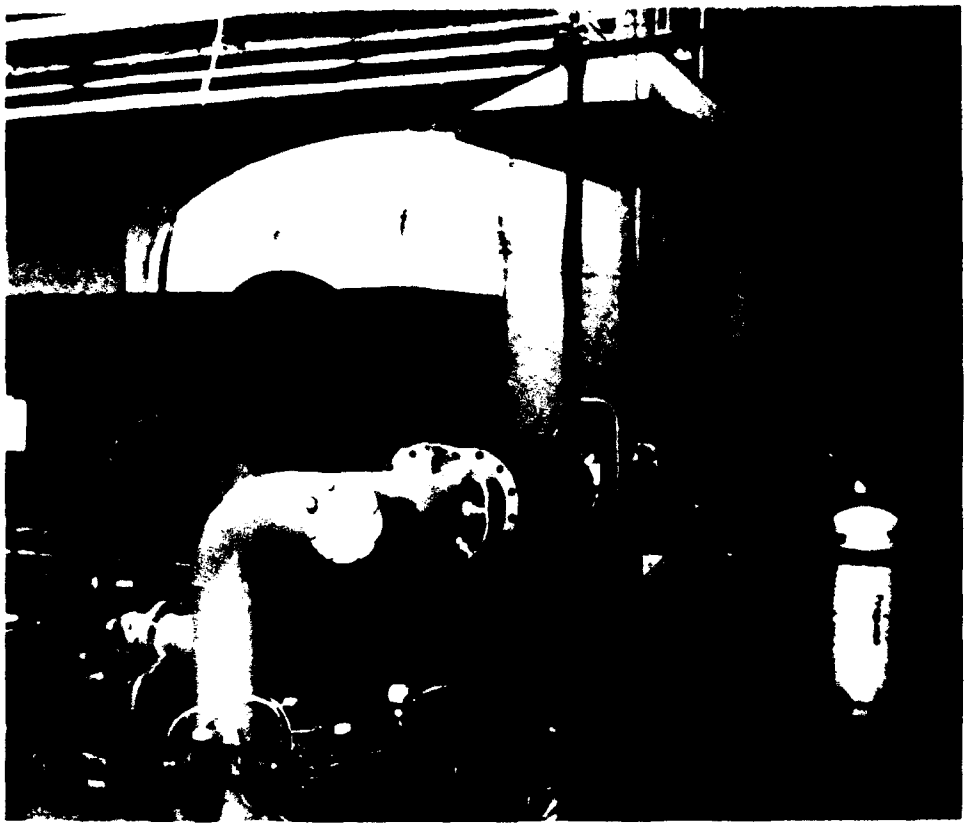

Figure 10: Wright Laboratory Combustor Facility in Building 18

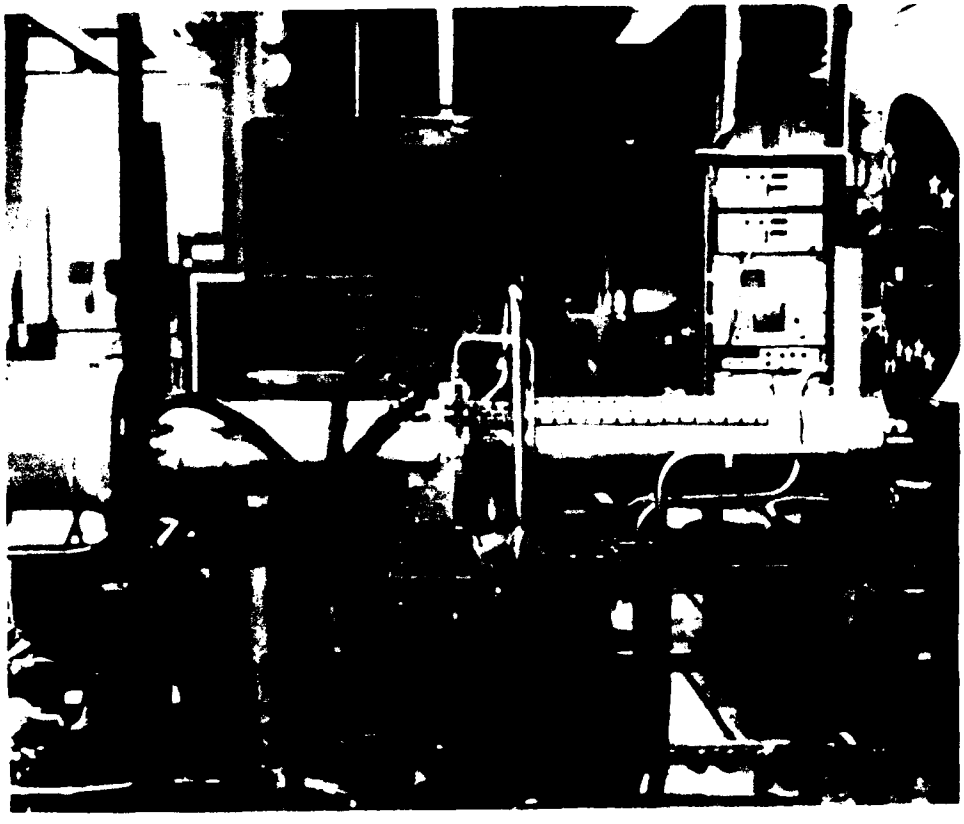

Figure 11: Water Cooled Stainless Steel Combustor

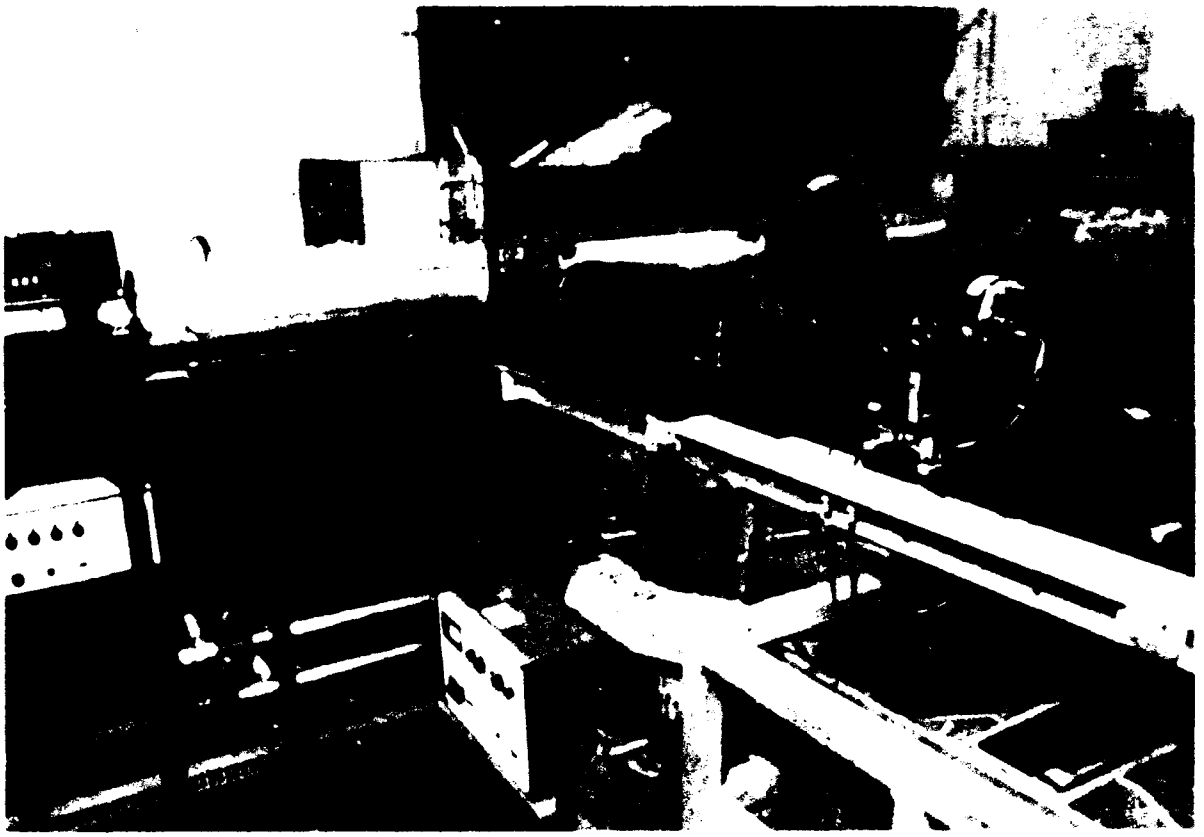

Figure 12: Water-Cooled Stainless Steel Combustor and LDV Mounted xyz table

in section 2.2, the fuel injector and swirler are mounted in a piston arrangement, shown schematically in Figure 13. The actual swirler housing assembly used in both the Plexiglas and water cooled rig is shown in Figures 14 and 15.

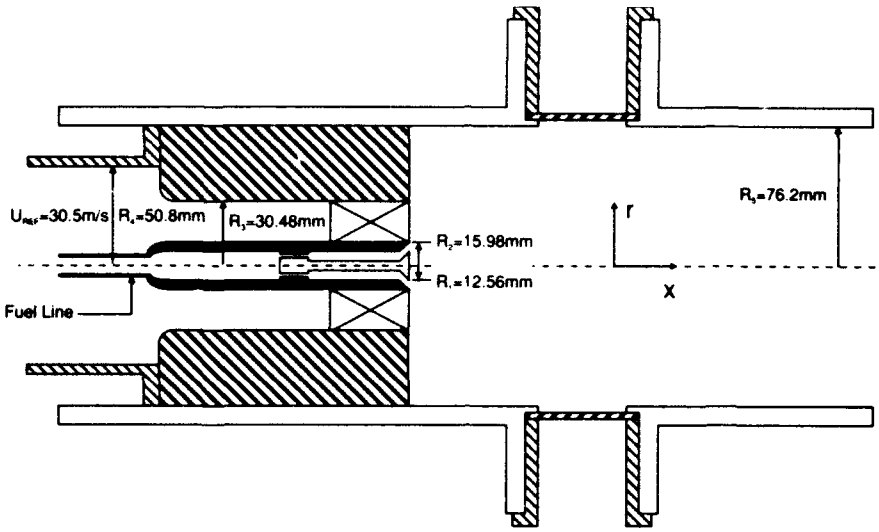

Figure 13: Schematic Detail of Swirler/Injector Housing Assembly

Figure 14: Swirler Housing Assembly — Air In

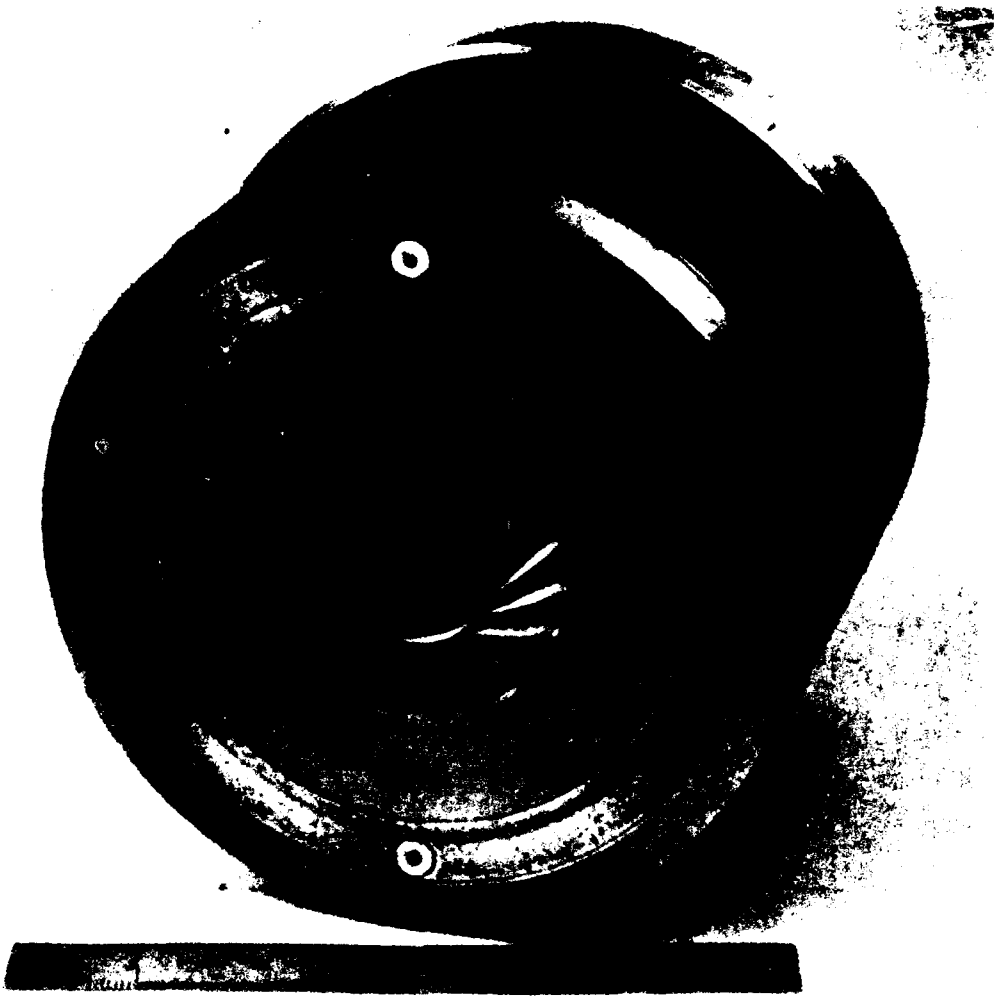

Figure 15: Swirler Housing Assembly — Air Out

2.4 New Rolls-Royce Designed Test Section

The new test section design had to address the following requirements:

1. Suitable for combusting flows up to chamber pressures of $3atm$
2. Provide optical access which would permit the simultaneous measurement of:
   - 3 mean velocities (LDV)
   - Reynolds stresses (LDV)
   - temperatures (CARS)
   - species concentrations (CARS)
3. Reduce rig down-time caused by dirty optical windows
4. Minimize flow disturbances caused by optical access ports
5. Minimize laser beam distortion by employing flat, optical quality windows
6. Automate the movement of the test section in accordance with the movement of the laser diagnostic systems on their respective xyz tables
7. Fit into the Wright Laboratory facility with minimum interference

The heart of the new test section is a rotating water-cooled drum with optical access ports. The drum may be rotated in unison with the movement of the laser diagnostic systems on their xyz tables. This allows a laser probe volume to map out a full quadrant of the circular cross-section of the combustor, see Figure 16.

The drum is fabricated out of three annular sections. In the center section a hole has been cut through the wall. This hole has been cut to the minimum dimensions required to allow optical access for a back scatter two-component LDV system which focuses the laser beams (blue and green channels) through an 18° included cone angle. There is also a slot cut into the drum wall which traverses from the LDV hole to a point 110° further around the drum circumference. This slot is intended for the third channel incoming laser beams (possibly red or violet) of a future three component LDV system; the scattered signal would be collected back through the LDV hole. Such an LDV system has not yet been procured for this program and until then the slot will remain covered with a close fitting plug. Opposite the LDV hole there is another similarly dimensioned hole cut into the drum wall which will remain plugged until the use of the CARS or a forward scattering LDV system. If the CARS and LDV are operated in a coupled fashion, then the CARS beams fit coaxially within the blue and green LDV beams.

The center drum section containing the optical access holes is welded between two annular sections which contain an array of baffles between the inner and outer walls. The baffles are used to ensure uniform water-cooling. Water is supplied via

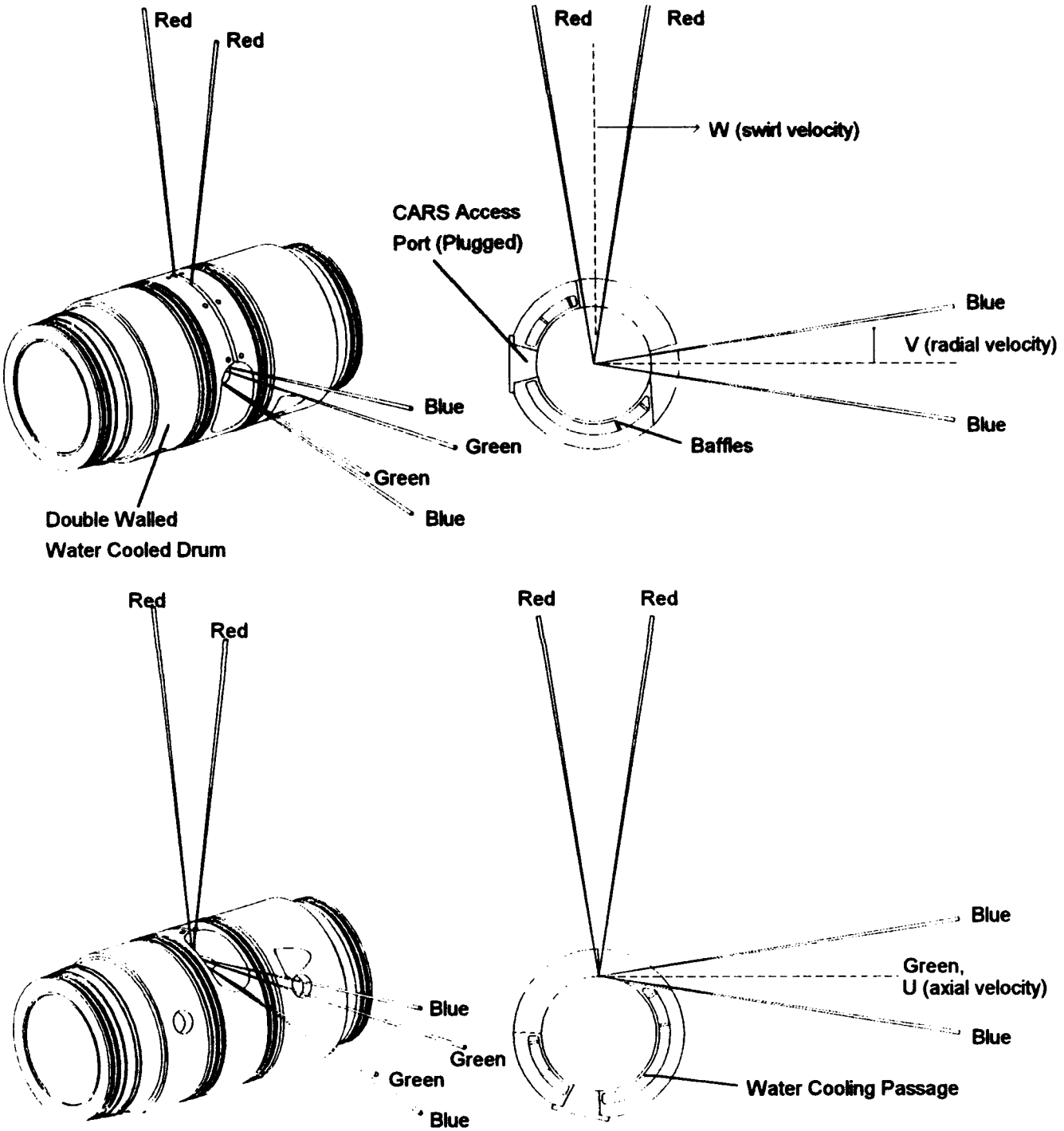

Figure 16: New Hot Test Section – Rotating Drum and Laser Diagnostics Access, Showing 3 Velocity Component Measurements along a Vertical Radius

flexible hoses connected to the rigid inlet and outlet pipes screwed into the wall of the drum. Since the drum rotates in order to obtain access to particular measurement stations, great care was taken to specially profile the rigid inlet and outlet water cooling pipes in order to avoid interference with other rig components. The drum as a whole is supported between two end plates via sealed bearings. Surrounding the optical access holes is a square air tight box connected to the drum through sealed O-rings, see Figure 17. Installed on three sides of this box are flat, optical quality quartz windows. The whole of the box is sealed to ensure that the pressure inside the combustor remains equal to the pressure inside the box and hence minimizes flow disturbance near the optical access holes.

The new test section design has incorporated two major improvements in an effort to ensure accurate and speedy data acquisition. First, it has been observed in the past that dirty optical windows can indeed affect the LDV results, hence it is very important to keep them as clean as practicably possible. In the WL water-cooled combustor, rig operations were frequently interrupted in order to clean the windows, which soon becomes a very tedious process. Thus, an air purge system has been incorporated to keep the windows as clean as possible. The purge system is to be operated during the period when the LDV is being moved from one measurement point to another. At the point of measurement the purge system will then be switched off and the LDV data acquisition immediately performed after ensuring stable running conditions. Second, the drum itself may be rotated by a stepper motor via a specially designed gear incorporated into the drum structure. It will essentially be possible to do the following automatically:

- move the LDV probe volume to any point within the measurement quadrant rotating the drum accordingly
- switch off the air purge
- acquire data
- turn on the air purge
- move to the next measurement point

An isometric of the complete test section is shown in Figure 18.

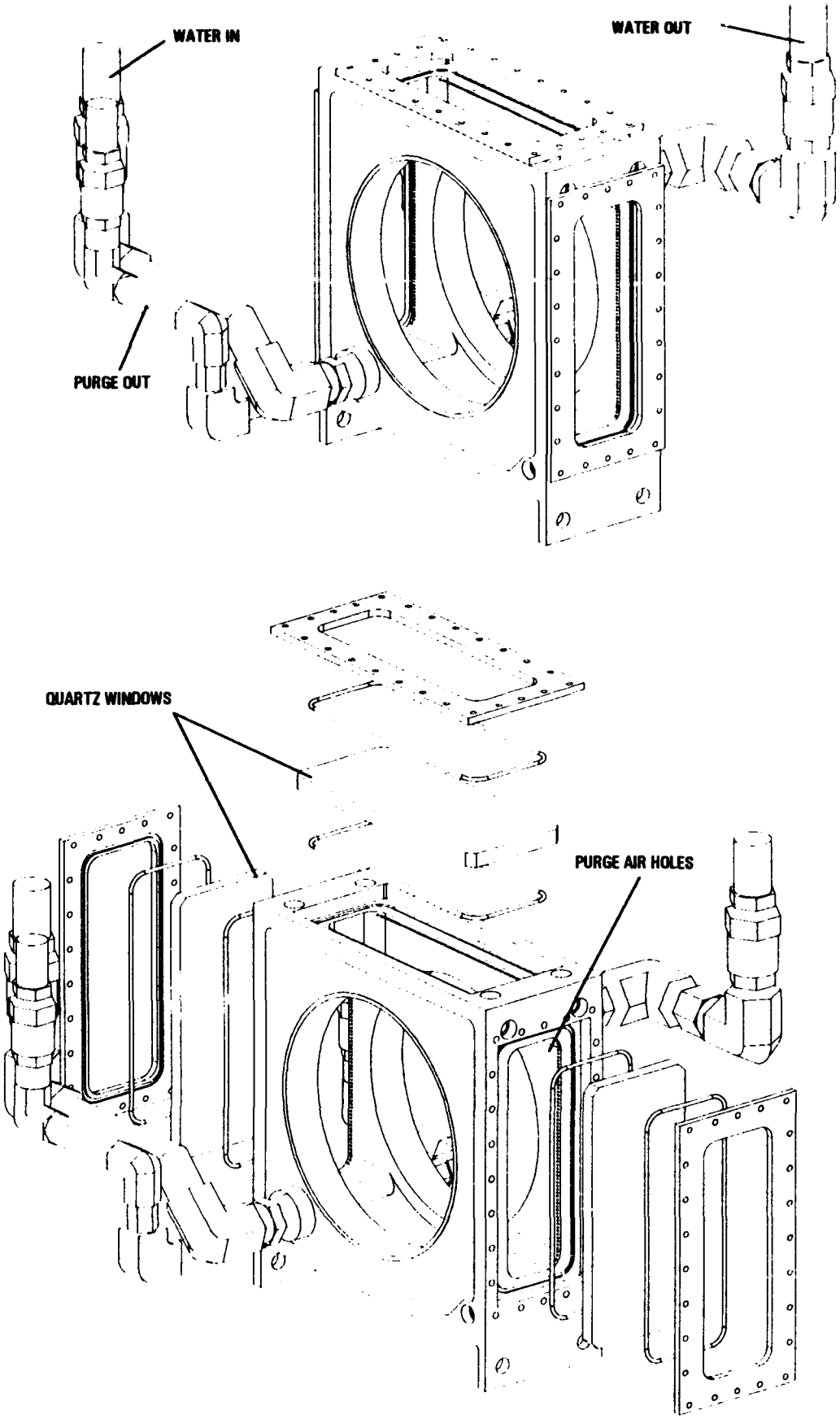

Figure 17: New Hot Test Section - Sealed Measurement Box

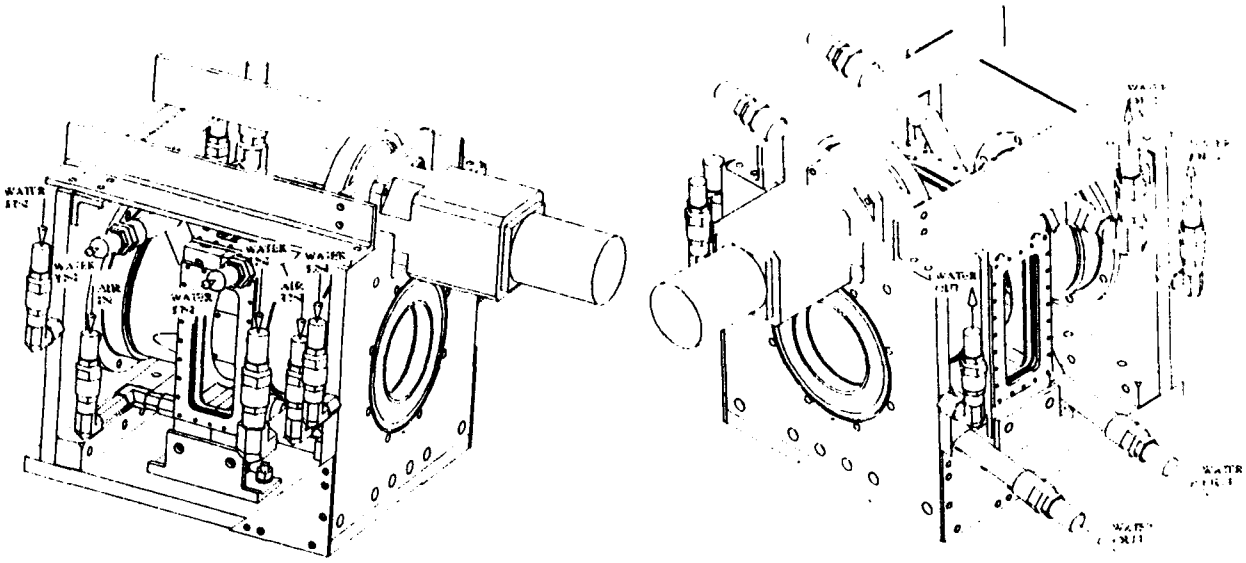

Figure 18: New Hot Test Section (Rolls-Royce Design)

2.5 Rig Operating Conditions

The rig operating conditions are summarized in Table 1 with the diagnostics employed in each experiment further detailed in Table 2.

No air heater is available on the WL facility at present, hence, only one inlet air temperature was employed. Wilhelmi [1] employed an equivalence ratio of 0.65, however, when this value was used on the WL facility a flow instability was observed, see Section 5.2. This was traced back to the combustor air inlet ductwork and was observed to be augmented within the combustor at higher equivalence ratios. Since modifying the ductwork to eradicate this instability, it was thought prudent to simply lower the equivalence ratio. Thus, an equivalence ratio of 0.45 was employed and no further problems were experienced.

The two-component LDV system mentioned in A and B of Table 2 is in fact the same system. Different quantities measured are due to the use of the different test sections employed in the Plexiglas and stainless steel rigs. The use of the new Rolls-Royce designed test section will allow all of the measurements quoted in A of Table 2 to be repeated for the combusting case.

Table 1: Summary of Rig Operating Conditions

Experiment	P (atm)	T_{in} (K)	m_{air} (kg/s)	m_{fuel} (kg/s)	AFR	Φ	Diagnostics
Isothermal	1.0	293	0.083	0.0	—	—	A
Propane Fuel	1.0	293	0.091	0.0026	34.91	0.45	B

where;

P is the chamber pressure

T_{in} is the inlet air temperature

m_{air} is the inlet air mass flow rate

m_{fuel} is the inlet fuel mass flow rate

AFR is the air to fuel ratio

Φ is the equivalence ratio

Table 2: Diagnostics Employed

Diagnostics	Arrangement	Measured Quantities
A	Two-component LDV	$\overline{U}$ $\overline{V}$ $\overline{W}$ $\overline{u'^2}$ $\overline{v'^2}$ $\overline{w'^2}$ $\overline{u'v'}$ $\overline{u'w'}$
B	Two-component LDV	$\overline{U}$ $\overline{W}$ $\overline{u'^2}$ $\overline{w'^2}$ $\overline{u'w'}$

3 Instrumentation

This section introduces the instrumentation used on the WL facility.

3.1 Laser Velocimeter

Velocity measurements were performed with a TSI Inc. 9100-7 four-beam, two color, backscatter fiber-optic LDV system. This system was equipped with two TSI 9180-3A frequency shifters to provide directional sensitivity. The entire optics were mounted on a three-axis traversing table with a resolution of $0.0025mm$. Some of the features of the optical setup were as follows:

1. The system was configured so that the fringe inclinations were at 45.67° and 135.17° to the combustor centerline.

2. The approximate measurement volume dimensions based on $1/e^2$ intensity points were $390\mu m$ length and $60\mu m$ diameter.

A chemical seeder developed by Craig et al. [6], which produced micron size Titanium dioxide particles was used in this study. To approach a uniformly seeded flow, the particles were introduced into the upstream settling chamber.

3.2 Data Acquisition and Analysis

Doppler signals from the photomultipliers were processed by two TSI burst counters, Models 1990 B&C with low and high pass filters set at 20MHz and 100MHz, respectively, on each processor. Typical validated data rates, with comparison settings of 1% and fringe counts of 16, were between 1,000 and 5,000/sec. With the implementation of a $20\mu sec$ coincidence window (the time between two Doppler bursts), the subsequent coincidence data transfer rate ranged between 500 and 2,500/sec. To reduce statistical uncertainties in the calculation of the higher order moments of turbulent fluctuations, 50,000 realizations per channel were collected at each measurement location. Later on, this number was reduced to 5,000 since it was proved that 5,000 realizations were sufficient for accurate estimation of all the statistical moments. In some rare cases of very low data rates, the sample size could be further relaxed to 2,000 or 1,000 realizations. Data transfer to the dedicated mini-vax computer system was accomplished in DMA mode, at a maximum rate of 1 megabyte/sec, through a custom made interface. Double precision (48-bit) calculations of all statistical moments using standard formulae were made at each measurement location. In most cases, the data were sufficiently noise-free to avoid the use of cut-off limits (within the 3 sigma rule) on the calculated velocity histograms.

The problem of velocity bias in LDV measurements has been examined thoroughly by many investigators. This error arises from the fact that counter type

signal processors make discrete velocity measurements from individual realizations of seed particles passing through the measurement volume. In a uniformly seeded flow, the number of particles per unit time passing through the measurement volume is proportional to the flow rate through that volume, and simple arithmetic averaging of an ensemble of realizations will produce results biased toward values greater than the true temporal mean. This effect is more pronounced in highly turbulent flows, and a number of different schemes have been proposed for its removal. The method adopted in the current study used the time between individual realizations (particle interarrival time) as a weighting factor [7] for bias correction. The integrity of the system and the data acquisition software were checked in a simple free jet experiment, reported by Ahmed et al. [8]. The uncertainty of the measured mean velocities was determined using the techniques described by Snyder et al. [9]. The uncertainty ΔU is determined by the relation:

$$\Delta U = \pm 1.96 \frac{\sigma_u}{\sqrt{N}} \tag{4}$$

For 95% confidence level, the constant 1.96 is used; σ_u is an estimator for the true standard deviation and N is the sample size (5,000). From the above relation, the maximum uncertainties of the mean quantities (i.e., $\overline{U}, \overline{V}, \overline{W}$) due to random errors were found to be 2.0, 1.8 and 1.1% of the upstream centerline velocity, respectively.

The inlet flow conditions were the same as reported earlier [7], where the measurements were made in the horizontal plane $95mm$ upstream of the swirler housing assembly. The inlet flow profile was shown to be a fully developed pipe flow with axial turbulence intensity of 5% at the center, increasing to 9.5% near the wall. As expected, the tangential velocity was insignificant. The swirl turbulence intensity increased from 4% at the center to 8% at the wall.

3.3 Coherent Anti–Stokes Raman Spectroscopy (CARS)

A further addtion to the WL rig capabilities is currently coming on line. That is, the CARS instrument, which will permit the nonintrusive measurement of temperature and later concentrations of major species. This instrumentation has been designed and built by Dr. Larry Goss of Scientific Research Laboratories, under finance from WL and the Arnold Engineering and Development Center (AEDC). Details are expected to be reported in the near future.

4 Fluid Dynamic Equations and CFD Modeling

The aim of this section is to document the relevant equations used in the CFD models. This program of research does anticipate detailed combustion diagnostic measurements. However, the combustion phase of the program has not yet been completed and, therefore, the turbulence equations for variable density flows and chemistry models will not be covered in this report.

The extremely wide range of length and time scales associated with high Reynolds number turbulent flows, coupled with the constraints of present day computing resources demand that mathematical models developed to predict them be based on a statistical approach. In the case of flows where the density variations are weak, the method commonly used is to decompose all velocities, scalars and the pressure into respective time-mean and fluctuating components. After this decomposition, averaging the resultant equations in time leads to equations for individual mean velocity components and scalar properties, which involve unknown double correlations between turbulent velocity fluctuations alone, or between velocity and scalar fluctuations. Two general routes are available to close the equation set, namely, to model the correlations indirectly via an eddy-viscosity approach, such as the $k-\epsilon$ model, or to obtain them from modelled forms of their own transport equations, such as the Reynolds Stress Transport Model (RSTM).

If density variations are large then the approach may be extended to include the decomposition of the density variable. This leads to second- and third-moment correlations containing density fluctuations, in addition to the second-moment fluctuating velocity correlations encountered in the averaged equations for constant density flows. These terms are large in number and an approach to reducing the complexity of these equations is to use an alternative method of decomposition and averaging, namely the mass-weighted formulation suggested by Favre [10]. This modified averaging procedure results in mean flow equations describing variable density situations which are formally identical to their constant density counterparts. However, all velocities, scalar properties and related correlations, appear as mass-weighted rather than unweighted time-average quantities. The approach used in presenting these equations is that of Hogg [11], which is an excellent reference. Further details may be found in References [1], [12] and [13].

As already mentioned, statistical methods are commonly used to describe the mean quantities. The expected value of any dependent variable is based on the probability distribution of that variable. It is not absolutely defined, but can be weighted or based on special conditions. Two types of averages are commonly used, these being the unweighted average and the density weighted average or mass-weighted average, suggested by Favre [10].

The *weighted* time average of a random variable $\phi(x_i, t)$, as a function of the position and time is defined as:

$$\overline{\phi(x)} = \lim_{\Delta t \to \infty} \frac{1}{\Delta t} \int_t^{t+\Delta t} \phi(x_i, t) W(t) dt \tag{5}$$

where $W(t)$ is a weighting factor. Using a unit value of weighting factor results in the average value of ϕ as being a simple time mean value, hence, *unweighted decomposition* consists of rewriting the instantaneous values of ϕ as the sum of a time mean part $\overline{\phi}$ and a fluctuating component ϕ':

$$\phi(x_i, t) = \overline{\phi}(x_i) + \phi'(x_i, t) \tag{6}$$

For a stationary flow the mean value of ϕ that is, $\overline{\phi}$ is independent of the time. By definition the time average of the unweighted fluctuation $\overline{\phi'} = 0$. The Favre density or mass weighted average of the random variable ϕ arises from the use of a weighting factor $(\rho/\overline{\rho})$:

$$\tilde{\phi(x)} = \lim_{\Delta t \to \infty} \frac{1}{\Delta t} \int_t^{t+\Delta t} \frac{\rho(x_i, t)}{\overline{\rho}(x_i)} \phi(x_i, t) dt \tag{7}$$

$$\overline{\rho}(x_i) = \lim_{\Delta t \to \infty} \frac{1}{\Delta t} \int_t^{t+\Delta t} \rho(x_i, t) dt \tag{8}$$

from equation 7:

$$\overline{\rho}(x_i)\tilde{\phi}(x_i) = \overline{\rho(x_i, t)\phi(x_i, t)} \tag{9}$$

Thus, the *density weighted decomposition* involves a representation of the instantaneous value of ϕ as a density weighted mean value $\tilde{\phi}$ and a fluctuation about that mean of ϕ'':

$$\phi(x_i, t) = \tilde{\phi}(x_i) + \phi''(x_i, t) \tag{10}$$

$$\tilde{\phi}(x_i, t) = \frac{\overline{\rho(x_i, t)\phi(x_i, t)}}{\overline{\rho(x_i)}} \tag{11}$$

Note that $\overline{\rho(x_i, t)\phi''(x_i, t)} = 0$ but $\overline{\phi''(x_i, t)} \neq 0$.

Using the above equations, a further equation describing the relationship between the product of the fluctuating components of two variables may be derived:

$$\overline{\phi_i''\phi_j''} = \overline{\phi_i'\phi_j'} - \frac{1}{\overline{\rho}^2} \overline{\rho'\phi_i'}\,\overline{\rho'\phi_j'} + \frac{1}{\overline{\rho}} \overline{\rho'\phi_i'\phi_j'} \tag{12}$$

This expression indicates the degree of simplification achieved by mass averaging relative to unweighted averaging.

4.1 Mean Flow Equations

The aim of this section is to introduce the equations governing both unweighted and density-weighted mean flow properties for turbulent flows in Cartesian-tensor notation. All swirling flow predictions discussed in this report are calculated within a two-dimensional axisymmetric framework, therefore, the mean field transport equations for the conservation of mass, momentum and a scalar, expressed in cylindrical polar coordinates with swirl are given in Appendix A.

4.1.1 Uniform–Density Turbulent Flow

The equations describing the conservation of mass, transport momentum and a scalar are as follows.

Conservation of mass:

$$\frac{\partial \rho}{\partial t} + \frac{\partial \rho U_i}{\partial x_i} = 0 \tag{13}$$

Conservation of momentum, neglecting external body forces:

$$\frac{\partial \rho U_i}{\partial t} + \frac{\partial \rho U_i U_j}{\partial x_j} = -\frac{\partial p}{\partial x_i} + \frac{\partial}{\partial x_j}\mu\left(\frac{\partial U_i}{\partial x_j} + \frac{\partial U_j}{\partial x_i} - \frac{2}{3}\delta_{ij}\frac{\partial U_k}{\partial x_k}\right) \tag{14}$$

where δ_{ij} is the Kronecker delta:

$$\delta_{ij} = \begin{cases} 0 & \text{if } i \neq j \\ 1 & \text{if } i = j \end{cases}$$

Conservation of a scalar:

$$\frac{\partial \rho C}{\partial t} + \frac{\partial \rho U_j C}{\partial x_j} = \frac{\partial}{\partial x_j}\frac{\mu}{\sigma_c}\frac{\partial C}{\partial x_j} + S_c \tag{15}$$

S_c represents the source of the scalar C. These equations describe the relationship between the instantaneous values of the various flow properties. For steady turbulent flows, equations governing the mean velocity components and the time-mean value of any conserved scalar may be obtained by introducing unweighted decomposition into equations 13, 14 and 15:

$$\frac{\partial \rho \overline{U_i}}{\partial x_i} = 0 \tag{16}$$

$$\frac{\partial \rho \overline{U_i}\,\overline{U_j}}{\partial x_j} = -\frac{\partial \overline{p}}{\partial x_i} + \frac{\partial}{\partial x_j}\mu\left(\frac{\partial \overline{U_i}}{\partial x_j} + \frac{\partial \overline{U_j}}{\partial x_i}\right) - \frac{\partial}{\partial x_j}\left(\rho\,\overline{u_i' u_j'}\right) \tag{17}$$

$$\frac{\partial \rho \overline{U_j}\,\overline{C}}{\partial x_j} = -\frac{\partial}{\partial x_j}\frac{\mu}{\sigma_c}\frac{\partial \overline{C}}{\partial x_j} - \frac{\partial}{\partial x_j}\left(\rho\,\overline{u_j' c'}\right) + \overline{S}_c \tag{18}$$

These equations differ from those for laminar flow through the appearance of second moment correlations in the momentum and scalar equations involving the turbulent velocity and scalar fluctuations, known as the *Reynolds stresses* and the *scalar fluxes*, respectively. The stresses and fluxes appearing in the time averaged equations of motion provide the link through which the turbulence is able to influence the mean velocity field.

4.1.2 Variable Density Turbulent Flow

If unweighted decomposition is applied to all flow dependent variables, including density, which appear in the high Reynolds number versions of the transport equations, we get:

$$\frac{\partial}{\partial x_j}\left[\overline{\rho}\,\overline{U}_j + \overline{\rho' u'_j}\right] = 0 \tag{19}$$

$$\frac{\partial}{\partial x_j}\left[\overline{\rho}\,\overline{U_i}\,\overline{U_j} + \overline{U_j}\,\overline{\rho' u'_i}\right] = -\frac{\partial \overline{p}}{\partial x_i} - \frac{\partial}{\partial x_j}\left[\overline{U_i}\,\overline{\rho' u'_j} + \overline{\rho}\,\overline{u'_i u'_j} + \overline{\rho' u'_i u'_j}\right] \tag{20}$$

$$\frac{\partial}{\partial x_j}\left[\overline{\rho}\,\overline{U_j}\,\overline{C} + \overline{U_j}\,\overline{\rho' c'}\right] = -\frac{\partial}{\partial x_j}\left[\overline{C}\,\overline{\rho' c'} + \overline{\rho}\,\overline{u'_j c'} + \overline{\rho' u'_j c'}\right] + \overline{S_c} \tag{21}$$

These equations contain both second- and third-order correlations involving turbulent density fluctuations, in addition to the Reynolds stresses and scalar fluxes encountered in the constant density flow equations. All of these correlations must be evaluated in order to solve the equations.

By adopting the Favre density weighting decomposition, for high Reynolds number[1] turbulent flows, we obtain the following equations:

$$\frac{\partial}{\partial x_j}\left(\overline{\rho}\tilde{U}_j\right) = 0 \tag{22}$$

$$\frac{\partial}{\partial x_j}\left(\overline{\rho}\tilde{U}_i\tilde{U}_j\right) = -\frac{\partial \overline{p}}{\partial x_i} - \frac{\partial}{\partial x_j}\left(\overline{\rho}\,\widetilde{\overline{u''_i u''_j}}\right) \tag{23}$$

$$\frac{\partial}{\partial x_j}\left(\overline{\rho}\tilde{U}_j\tilde{C}\right) = -\frac{\partial}{\partial x_j}\left(\overline{\rho}\,\widetilde{\overline{u''_j c''}}\right) + \tilde{S}_c \tag{24}$$

This technique effectively "hides" all correlations containing density fluctuations which would appear if unweighted averaging was used with the density variable.

[1] The Reynolds number is assumed high enough for viscous effects (which are included in PACE) to be negligible in comparison to the other terms in the conservation equations.

4.1.3 The Reynolds Stress Equations

The Reynolds stresses $\overline{u_i'u_j'}$ appear as unknown second moment correlations in the time averaged momentum equation 17. A set of equations for the Reynolds stress can be derived by subtracting the time averaged momentum equation from the decomposed instantaneous momentum balance. This equation is then multiplied by u_j' and added to the corresponding product of an equation for u_j' multiplied by u_i'. Time averaging the resultant form then yields an equation for the Reynolds stresses:

$$\begin{aligned}\rho\overline{U_k}\frac{\partial\overline{u_i'u_j'}}{\partial x_k} &= -\left[\rho\overline{u_j'u_k'}\frac{\partial\overline{U_i}}{\partial x_k} + \rho\overline{u_i'u_k'}\frac{\partial\overline{U_j}}{\partial x_k}\right] \\ &\quad -\frac{\partial}{\partial x_k}\left[\rho\overline{u_i'u_j'u_k'}\right] - \left[\overline{u_i'\frac{\partial p'}{\partial x_j}} + \overline{u_j'\frac{\partial p'}{\partial x_i}}\right] \\ &\quad +\overline{u_j'\frac{\partial}{\partial x_k}\left[\mu\left[\frac{\partial u_i'}{\partial x_k} + \frac{\partial u_k'}{\partial x_i}\right]\right]} + \overline{u_i'\frac{\partial}{\partial x_k}\left[\mu\left[\frac{\partial u_j'}{\partial x_k} + \frac{\partial u_k'}{\partial x_j}\right]\right]}\end{aligned} \tag{25}$$

which can be rewritten in the following form:

$$\begin{aligned}\underbrace{\rho\overline{U_k}\frac{\partial\overline{u_i'u_j'}}{\partial x_k}}_{A} &= -\underbrace{\left[\rho\overline{u_j'u_k'}\frac{\partial\overline{U_i}}{\partial x_k} + \rho\overline{u_i'u_k'}\frac{\partial\overline{U_j}}{\partial x_k}\right]}_{B} \\ &\quad \underbrace{-\frac{\partial}{\partial x_k}\left[\rho\overline{u_i'u_j'u_k'} - \mu\left[\frac{\partial\overline{u_i'u_j'}}{\partial x_k} + \overline{u_j'\frac{\partial u_k'}{\partial x_i}} + \overline{u_i'\frac{\partial u_k'}{\partial x_j}}\right]\right] - \frac{\overline{\partial p'u_j'}}{\partial x_i} - \frac{\overline{\partial p'u_i'}}{\partial x_j}}_{C} \\ &\quad \underbrace{+\overline{p'\left[\frac{\partial u_i'}{\partial x_j} + \frac{\partial u_j'}{\partial x_i}\right]}}_{D} \underbrace{-2\mu\overline{\frac{\partial u_i'}{\partial x_k}\frac{\partial u_j'}{\partial x_k}} - \mu\left[\overline{\frac{\partial u_i'}{\partial x_k}\frac{\partial u_k'}{\partial x_j}} + \overline{\frac{\partial u_j'}{\partial x_k}\frac{\partial u_k'}{\partial x_i}}\right]}_{E}\end{aligned} \tag{26}$$

Convection of the Reynolds stress $\overline{u_i'u_j'}$ is represented by term A and according to equation 26 is balanced by the four processes on the RHS of the equation. The grouped terms represent production (B), diffusion (C), pressure-strain interaction (D) and dissipation (E) of the stresses respectively. Note that these are exact equations and no assumptions have been made at this point. Both the convection and production terms contain only the stresses themselves and mean velocities. As transport equations are solved for all of these quantities, no modeling is required in either term. The remaining three groups of terms all contain unknown correlations which require modeling to close the equations.

4.1.4 The Scalar Flux Equations

A transport equation for the scalar fluxes $\overline{u_i'c'}$ can be obtained in a similar manner to that used for the Reynolds stresses. The exact transport equation for the scalar fluxes can be written in the following form:

$$\underbrace{\rho\overline{U_k}\frac{\partial\overline{u_i'c'}}{\partial x_k}}_{A} = \underbrace{-\left[\rho\overline{u_k'c'}\frac{\partial\overline{U_i}}{\partial x_k} + \rho\overline{u_i'u_k'}\frac{\partial\overline{C}}{\partial x_k}\right]}_{B}$$
$$\underbrace{-\frac{\partial}{\partial x_k}\left[\rho\overline{u_i'u_k'c'}\right] - \frac{\partial\overline{p'c'}}{\partial x_i}}_{C}$$
$$\underbrace{+\overline{p'\frac{\partial c'}{\partial x_i}}}_{D} \underbrace{-\left[\frac{\mu}{\sigma_c}+\mu\right]\overline{\frac{\partial u_i'}{\partial x_k}\frac{\partial c'}{\partial x_k}} - \mu\overline{\frac{\partial c'}{\partial x_k}\frac{\partial u_k'}{\partial x_i}}}_{E} \tag{27}$$

The convection (term A) of the scalar fluxes is balanced by the four terms on the RHS of this equation representing processes of production (B), diffusion (C), pressure–scalar gradient interaction (D) and dissipation (E). The production terms contained in group B show that the fluxes are generated by gradients in the mean scalar field and also gradients in the mean velocity field. The convection and production terms contain only known quantities and unlike the remaining terms require no modeling.

4.2 Turbulence Closure

From equations 26 and 27 it has become apparent that there are some terms which are unknown, namely, the correlations between the fluctuating quantities such as pressure. Turbulence closure is the approach used to model the unknown terms and thereby close the fluid dynamic equations, that is, provide the same number of equations as there are unknown variables in order to solve the problem. In this program both a $k-\epsilon$ and Reynolds Stress Transport Model (RSTM) are used; these will now be introduced.

4.2.1 The Eddy–Viscosity Hypothesis

Boussinesq [14],[15] suggested that for a turbulent flow, the Reynolds stresses may be assumed to vary linearly with the local mean rate of strain in a similar manner to laminar stresses in a Newtonian fluid. The proportionality factor in this relation is known as the *turbulent viscosity* of the fluid, μ_t, which unlike the laminar viscosity, is a flow–dependant variable. Thus we get:

$$-\rho\overline{u_i'u_j'} = \mu_t\left[\frac{\partial\overline{U_i}}{\partial x_j} + \frac{\partial\overline{U_j}}{\partial x_i} - \frac{2}{3}\delta_{ij}\frac{\partial\overline{U_k}}{\partial x_k}\right] - \frac{2}{3}\rho k \tag{28}$$

Similarly, the scalar-fluxes can be modelled in terms of mean scalar gradients using the eddy-diffusivity hypothesis, which following the definition of a suitable flow property related Prandtl-number, yields:

$$-\rho\overline{u_i'c'} = \frac{\mu_t}{\sigma_{ct}}\frac{\partial\overline{C}}{\partial x_i} \tag{29}$$

Substitution of equations 28 and 29 into equations 16, 17 and 18 yields the following time averaged momentum and mean scalar conservation equations for constant density turbulent flows:

$$\frac{\partial}{\partial x_j}\left[\rho\overline{U_i}\,\overline{U_j}\right] = -\frac{\partial P}{\partial x_i} + \frac{\partial}{\partial x_j}\left[\mu + \mu_t\right]\left[\frac{\partial\overline{U_i}}{\partial x_j} + \frac{\partial\overline{U_j}}{\partial x_i}\right] \tag{30}$$

$$\frac{\partial}{\partial x_j}\left[\rho\overline{U_j}\,\overline{C}\right] = \frac{\partial}{\partial x_j}\left[\frac{\mu}{\sigma_c} + \frac{\mu_t}{\sigma_{ct}}\right]\frac{\partial\overline{C}}{\partial x_j} + \overline{S_c} \tag{31}$$

For convenience, the pressure in equation 30 has been redefined to include the turbulence–energy term appearing in the Boussinesq approximation shown in equation 28. The true pressure term can be recovered after analysis if required.

By use of the Boussinesq approximation the closure problem has been reduced to evaluating a single turbulent viscosity rather than the larger task of assigning values to each and every component of the Reynolds stress tensor.

4.2.2 The $k-\epsilon$ Model

The $k-\epsilon$ turbulence model [16] relies on the outcome of transport equations for both turbulence energy, k, and its dissipation rate, ϵ, to evaluate a turbulent viscosity μ_t:

$$\epsilon \propto \frac{k^{1.5}}{l} \tag{32}$$

$$\mu_t = C_\mu\rho\frac{k^2}{\epsilon} \tag{33}$$

where, l is a turbulence length scale and:

$$k = \frac{1}{2}\overline{u_i'u_j'}\delta_{ij} \tag{34}$$

A transport equation for k can consequently be obtained by contracting the Reynolds stress equation 26. This involves setting the tensor subscript j to i (or multiplying by δ_{ij}) and dividing the final results by two, to give:

$$\underbrace{\rho\overline{U_k}\frac{\partial k}{\partial x_k}}_{A} = \underbrace{-\rho\overline{u_i'u_k'}\frac{\partial \overline{U_i}}{\partial x_k}}_{B}$$
$$\underbrace{-\frac{\partial}{\partial x_k}\left[\rho\overline{u_i'u_i'u_k'} - \mu\left[\frac{\partial k}{\partial x_k} + \overline{\frac{\partial u_i'u_k'}{\partial x_k}}\right]\right] - \overline{\frac{\partial P'u_i'}{\partial x_i}}}_{C}$$
$$\underbrace{-\mu\overline{\frac{\partial u_i'}{\partial x_k}\left[\frac{\partial u_i'}{\partial x_k} + \frac{\partial u_k'}{\partial x_i}\right]}}_{D} \tag{35}$$

The convection of the turbulence energy (A) is balanced by the processes of production (B), diffusion (C) and dissipation (D).

With the exception of convection, the terms appearing in equation 35 cannot be accommodated in their exact form, because at this level of closure only mean velocities, the turbulence energy and its dissipation rate are available. Therefore, the terms grouped in B and C require modeling.

Group B describing the generation of k contains an unknown second-moment correlation which can be eliminated by a direct application of the Boussinesq eddy-viscosity assumption given in equation 28. Group B can be rewritten for constant density flow as:

$$B \rightarrow +\mu_t\frac{\partial \overline{U_i}}{\partial x_k}\left[\frac{\partial \overline{U_i}}{\partial x_k} + \frac{\partial \overline{U_k}}{\partial x_i}\right] \tag{36}$$

The diffusion terms in group C are modelled collectively as the product of a gradient in the turbulent energy field and the eddy-viscosity, which is the appropriate exchange coefficient since k is intimately linked to the velocity. Thus, the modelled form of the diffusion term is:

$$C \rightarrow +\frac{\partial}{\partial x_k}\frac{\mu_t}{\sigma_k}\frac{\partial k}{\partial x_k} \tag{37}$$

with $\sigma_k = 1$.

Finally, the dissipation terms of group D, represented by ϵ, require no modeling in the k-equation, as a transport equation is solved for this quantity. Consequently, the modelled form of equation 35 can be written:

$$\rho\overline{U_k}\frac{\partial k}{\partial x_k} = +\frac{\partial}{\partial x_k}\frac{\mu_t}{\sigma_k}\frac{\partial k}{\partial x_k} + \mu_t\frac{\partial \overline{U_i}}{\partial x_k}\left[\frac{\partial \overline{U_i}}{\partial x_k} + \frac{\partial \overline{U_k}}{\partial x_i}\right] - \rho\epsilon \tag{38}$$

An equation for the turbulence energy dissipation rate is required to complete the $k-\epsilon$ turbulence model. An exact equation can be derived but for simplicity an

Table 3: Constants Employed in $k - \epsilon$ Model

Source	C_μ	$C_{\epsilon 1}$	$C_{\epsilon 2}$	σ_k	σ_ϵ	σ_c
Launder and Spalding	0.09	1.44	1.92	1.0	1.22	
Jones	0.09	1.44	1.92	1.0	1.3	0.9

intuitive model is used which draws on an analogy with the k-equation, that is, a balance between convection, diffusion, production and dissipation, with coefficients determined by reference to certain limiting cases.

Turbulence energy is generated by energy transfer from the mean flow to the large scale motion and then on to finer scales, so any equation describing ϵ must have a mechansim which allows it to increase to counter a rise in k. In addition, the dissipation rate equation must contain a mechanism through which ϵ can decrease quickly enough to prevent k from becoming negative in regions of flow where energy transfer from the mean motion is small. A transport equation for ϵ, which includes these features, together with the processes of convection and diffusion can be written in the following form:

$$\rho \overline{U_k} \frac{\partial \epsilon}{\partial x_k} = + \frac{\partial}{\partial x_k} \frac{\mu_t}{\sigma_\epsilon} \frac{\partial \epsilon}{\partial x_k} + C_{\epsilon 1} \frac{\epsilon}{k} \left[\mu_t \frac{\partial \overline{U_i}}{\partial x_k} \left[\frac{\partial \overline{U_i}}{\partial x_k} + \frac{\partial \overline{U_k}}{\partial x_i} \right] \right] - C_{\epsilon 2} \rho \frac{\epsilon^2}{k} \tag{39}$$

The constants used to solve the $k - \epsilon$ equations suggested by Launder and Spalding [16] after an extensive evaulation of free turbulent flows are shown in Table 3. Table 3 also shows the constants recommended by Jones [17] after a degree of computer optimization; these constants are used in this study.

4.2.3 The Reynolds Stress Equation Closure

In this type of closure, the differential forms of the Reynolds Stress equations are solved for each component of the stress tensor. This type of model is often referred to as a *Differential-Stress Model.*

The Differential-Stress Model described here is Gibson and Launder's [18] simplified version of the high Reynolds number Reynolds Stress transport closure of Launder et al. [19]. The exact form of the Reynolds transport equation 26 is rewritten:

$$C_{ij} = P_{ij} + d_{ij} + \Phi_{ij} + \rho \epsilon_{ij} \tag{40}$$

where C_{ij} represents the convection of stress $\overline{u_i' u_j'}$, given by:

$$C_{ij} = \rho \overline{U_k} \frac{\partial \overline{u_i' u_j'}}{\partial x_k} \tag{41}$$

and P_{ij} is the production of stress $\overline{u_i'u_j'}$:

$$P_{ij} = -\left[\rho\overline{u_j'u_k'}\,\frac{\partial \overline{U_i}}{\partial x_k} + \rho\overline{u_i'u_k'}\,\frac{\partial \overline{U_j}}{\partial x_k}\right] \tag{42}$$

At this level of closure, transport equations are solved for all quantities appearing in the convection and production terms of equation 40 and so, no modeling is required for these processes. However, the remaining three terms contain unknown quantities which need to be modelled.

Diffusion d_{ij}

The diffusive transport terms appearing in equation 26 comprise three sources, namely, the explicit triple–moment velocity correlations, viscous effects and correlations of fluctuating pressure. In this work we are considering only high Reynolds number flows where diffusion due to viscosity–related processes is assumed negligible everywhere except in the near wall region where empirical laws are employed.

Very little information is available that would throw light on the effect of the pressure correlation terms, consequently this term is neglected. The remaining term is the triple velocity correlation. Chou [20] proposed a transport equation for this term; however, it is very complex. Hanjalic and Launder [21] derived the following governing transport equation for the triple correlation term:

$$\overline{u_i'u_j'u_k'} = -C_k\frac{k}{\epsilon}\left[\overline{u_i'u_m'}\frac{\partial\overline{u_j'u_k'}}{\partial x_m} + \overline{u_j'u_m'}\frac{\partial\overline{u_i'u_k'}}{\partial x_m} + \overline{u_k'u_m'}\frac{\partial\overline{u_i'u_j'}}{\partial x_m}\right] \tag{43}$$

This has been simplified further by Daly and Harlow's [22] tensor turbulent transport coefficient, gradient–diffusion model:

$$d_{ij} = \frac{\partial}{\partial x_k}\left[\rho\overline{u_i'u_j'u_k'}\right] = \frac{\partial}{\partial x_k}\,C_k\,\rho\,\frac{k}{\epsilon}\,\overline{u_k'u_m'}\,\frac{\partial\overline{u_i'u_j'}}{\partial x_m} \tag{44}$$

which, at the present, is a very popular model. The use of this model would require the summation of many terms per Reynolds stress equation, thus, the simpler scalar turbulent viscosity, gradient diffusion model of Shir [23] is used in PACE:

$$d_{ij} = \frac{\partial}{\partial x_k}\left[\rho\overline{u_i'u_j'u_k'}\right] = \frac{\partial}{\partial x_k}\,C_s\,\rho\,\frac{k^2}{\epsilon}\,\frac{\partial\overline{u_i'u_j'}}{\partial x_m} \tag{45}$$

Pressure–Strain Interaction

Chou [20] showed that the pressure–strain correlation at a point well removed from a rigid surface can be expressed exactly as:

$$\overline{\frac{P''}{\rho}\left[\frac{\partial u_i'}{\partial x_j'} + \frac{\partial u_j'}{\partial x_i'}\right]} = \underbrace{-\frac{1}{4\pi}\int_{Vol}\overline{\left[\frac{\partial^2 u_l'u_m'}{\partial r_l r_m}\right]^*\left[\frac{\partial u_i'}{\partial r_j} + \frac{\partial u_j'}{\partial r_i}\right]}\frac{d\,Vol}{|\underline{r}|}}_{\Phi_{ij1}}$$

$$\underbrace{-\frac{1}{2\pi}\frac{\partial \overline{U_l}}{\partial x_m}\int_{Vol}\overline{\frac{\partial u'_m{}^*}{\partial r_l}\left[\frac{\partial u'_i}{\partial r_j}+\frac{\partial u'_j}{\partial r_i}\right]\frac{d\,Vol}{|\underline{r}|}}}_{\Phi_{ij_2}} \tag{46}$$

In the above equation an asterisk denotes a quantity which is evaluated at a position removed from the point in question, by the vector $\underline{r}$. r_i is the Cartesian component of $\underline{r}$ in the i'th direction. As $\underline{r}$ increases, the distance between the two points grows larger and the above equation shows that the pressure–strain correlation tends to zero. The redistribution process arises from two contributions. The term Φ_{ij_1}, represents the interaction purely between the turbulence quantities, and this term is modelled separately from the second part, Φ_{ij_2}, which reflects the turbulence/mean–strain interaction. Both of these terms tend to promote isotropization between normal stresses and a compatible reduction in the level of shear stress.

From Rotta [24] we have:

$$\Phi_{ij_1} = -C\rho\frac{\epsilon}{k}\left[\overline{u'_iu'_j} - \frac{\delta_{ij}}{3}\,\overline{u'_ku'_k}\right] \tag{47}$$

The coefficent C_1 has been given a wide range of values (0.6-3.0), but, the actual values adopted depends on the model used for Φ_{ij_1}. In this work, C_1 is taken to be equal to 1.8.

From Naot et al. [25] we have the simple Isotropization of Production Model for Φ_{ij_2}:

$$\Phi_{ij_2} = -C_2\left[P_{ij} - \frac{1}{3}\delta_{ij}P_{kk}\right] \tag{48}$$

This model is used in this work with C_2 equal to 0.6.

Equation 46 applies only to a point well removed from a rigid surface. If the expression for this redistribution term is extended to include near–wall effects, the complete equation would include additional surface integral terms.

The correction terms suggested by Shir [23] and Gibson and Launder [18], are used to account for the influence of the walls on the pressure–strain correlation. Separate corrections are made to both Φ_{ij_1} and Φ_{ij_2}, which are given below:

$$\Phi_{ij_1,w} = Cp_1\rho\frac{\epsilon}{k}\left[\overline{u'_ku'_m}n_kn_m\delta_{ij} - \frac{3}{2}\overline{u'_ku'_i}n_kn_j - \frac{3}{2}\overline{u'_ku'_j}n_kn_i\right]f_l \tag{49}$$

$$\Phi_{ij_2,w} = Cp_2\left[\Phi_{km_2}n_kn_m\delta_{ij} - \frac{3}{2}\Phi_{ik_2}n_kn_j - \Phi_{jk_2}n_kn_i\right]f_l \tag{50}$$

where suffix $l = k$ with no summation implied, and n_i is a unit vector normal to the wall. The function f_l relates the turbulence length scale to the distance from the wall and is given as:

$$f_l = \frac{C_\mu}{\kappa}\frac{k^{1.5}}{\epsilon}\frac{l}{x_l} \tag{51}$$

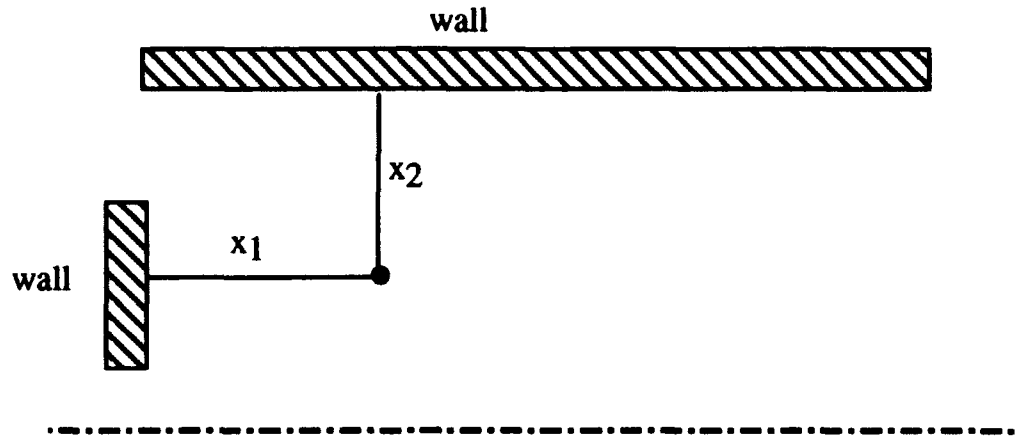

Figure 19: Wall Distances in Function f_l

where x_1 and x_2 are defined in Figure 19. This formulation does not allow for any wall–to–wall interaction, and assumes that the wall influences on the redistribution process are simply a function of the normal distance from that boundary.

For the axisymmetric flow studied here, where we have a wall which encircles the flow normal to the principal flow direction, f_l should strictly be a function of some average distance from the surrounding solid boundary. However, since wall–corrections are poorly understood they were considered to be of negligible importance. Thus, f_l was calculated from the above equation for this initial phase of modeling. Depending on the outcome of the experimental measurements, this could be an area to redress at a later stage.

The complete model from the pressure–strain interaction process becomes:

$$\Phi_{ij} = \Phi_{ij_1} + \Phi_{ij_2} + \Phi_{ijw} \tag{52}$$

Dissipation ϵ_{ij}

In many models the dissipation term is related to turbulence kinetic energy. Since dissipation arises from fine scale motions, it can be assumed to be an isotropic process, thus, from Rotta [24] we have:

$$\epsilon_{ij} = \frac{2}{3}\,\delta_{ij}\,\epsilon \tag{53}$$

However, this approximation fails in near–wall, two dimensional turbulence.

Adopting the compact presentation used by Hogg [11] allows the Cartesian tensor form and the two–dimensional axisymmetric form to be presented simultaneously. In the following equation, setting $\beta = 0$ yields the Cartesian tensor form of the equations. By setting $\beta = 1$, the transformed equation is obtained, where R_{ij}

accounts for the additive fragments of convection, production and diffusion which are shown in Table 4, and which arise due to the combined effects of the coordinate transformation and the presence of swirl. The common equation is given below as:

$$\begin{aligned}\frac{1}{r\beta}\frac{\partial}{\partial x_k}\left[\rho r\beta\overline{U_k}\ \overline{u_i'u_j'}\right] = \frac{1}{r\beta}\frac{\partial}{\partial x_k}&\left[r\beta C_k\rho\overline{u_k'u_l'}\frac{k}{\epsilon}\frac{\partial\overline{u_i'u_j'}}{\partial x_l}\right]\\ &-\rho\overline{u_i'u_k'}\frac{\partial\overline{U_j}}{\partial x_k}-\rho\overline{u_j'u_k'}\frac{\partial\overline{U_i}}{\partial x_k}\\ &-C_1\rho\frac{\epsilon}{k}\left[\overline{u_i'u_j'}-\frac{1}{3}\delta_{ij}\overline{u_k'u_k'}\right]\\ &-C_2\left[P_{ij}^*-\frac{1}{3}\delta_{ij}P_{kk}{}^*\right]\\ &+\Phi_{ij_w}-\frac{2}{3}\rho\delta_{ij}\epsilon+\beta R_{ij}\end{aligned}\tag{54}$$

The isotropization of production model, which forms part of the above model differs from that previously presented in that P_{ij} now appears as $P_{ij}{}^*$, where this quantity is defined as:

$$P_{ij}^* = P_{ij} - C_{ija}\tag{55}$$

and C_{ija} represents the additional algebraic convection terms appearing in the equation for stress $\overline{u_i'u_j'}$, and given in Table 4.

4.2.4 Scalar Flux Equation Closure

The modeling of the unknown correlations appearing in the scalar flux equations 15 is now considered. Adopting a similar approach to that used in modeling the unknown correlations in the Reynolds stress transport equations, the scalar flux equation can be re–written as:

$$C_{ic} = P_{ic} + d_{ic} + \Phi_{ic}\tag{56}$$

where, C_{ic} is the convection and P_{ic} the production of the flux $\overline{u_i'c'}$, which are given by:

$$C_{ic} = \rho\overline{U_k}\frac{\partial\overline{u_i'c_i'}}{\partial x_k}\tag{57}$$

$$P_{ic} = -\rho\overline{u_k'c'}\frac{\partial\overline{U_i}}{\partial x_k} - \rho\overline{u_i'u_k'}\frac{\partial\overline{C}}{\partial x_k}\tag{58}$$

At this level of closure, none of the terms in the two above equations require modeling and both can be treated exactly. However, PACE does not solve transport equations for the scalar fluxes ($\overline{u_i'c'}$), and instead models the turbulent transport of a scalar by a scalar turbulent viscosity diffusion model Hinze [26]:

$$\rho\overline{u_i'c'} = \frac{\mu_t}{\sigma_t}\frac{\partial\overline{c}}{\partial x_i}\tag{59}$$

Table 4: R_{ij} terms in Reynolds-Stress Equations

$\overline{u_i' u_j'}$	Convection	Production	Diffusion
$\overline{u'^2}$	—	—	—
$\overline{v'^2}$	$+ 2\rho\overline{v'w'}\,\frac{\overline{W}}{r}$	$+ 2\rho\overline{v'w'}\,\frac{\overline{W}}{r}$	$+ 2C_k\rho\,\frac{k}{\epsilon}\,\frac{(\overline{w'^2})^2}{r^2}$
	$-2\,\frac{\partial}{r\partial r}\left[C_k\rho\,\frac{k}{\epsilon}\,(\overline{v'w'})^2\right] - 2\,\frac{\partial}{\partial x}\left[C_k\rho\,\frac{k}{\epsilon}\,\overline{u'w'}\,\frac{\overline{v'w'}}{r}\right] - 2C_k\rho\,\frac{k}{\epsilon}\,\frac{\overline{w'^2}}{r^2}\,\overline{v'^2}$		
	$-2\,C_k\rho\,\frac{k}{\epsilon}\,\frac{\overline{u'w'}}{r}\,\frac{\partial\overline{v'w'}}{\partial x}$		$- 2C_k\rho\,\frac{k}{\epsilon}\,\frac{\overline{v'w'}}{r}\,\frac{\partial\overline{v'w'}}{\partial r}$
$\overline{w'^2}$	$- 2\rho\overline{v'w'}\,\frac{\overline{W}}{r}$	$- 2\rho\overline{w'^2}\,\frac{\overline{V}}{r}$	$+ 2C_k\rho\,\frac{k}{\epsilon}\,\overline{w'^2}\,\frac{\overline{v'^2}}{r^2}$
	$+ 2\,\frac{\partial}{r\partial r}\left[C_k\rho\,\frac{k}{\epsilon}\,(\overline{v'w'})^2\right] + 2\,\frac{\partial}{\partial x}\left[C_k\rho\,\frac{k}{\epsilon}\,\overline{u'w'}\,\frac{(\overline{v'w'})}{r}\right] - 2C_k\rho\,\frac{k}{\epsilon}\,\frac{(\overline{w'^2})^2}{r^2}$		
	$+ 2\,C_k\rho\,\frac{k}{\epsilon}\,\frac{\overline{u'w'}}{r}\,\frac{\partial\overline{v'w'}}{\partial x}$		$+ 2C_k\rho\,\frac{k}{\epsilon}\,\frac{1}{r}\,\overline{v'w'}\,\frac{\partial\overline{v'w'}}{\partial r}$
$\overline{u'v'}$	$+ \rho\overline{u'w'}\,\frac{\overline{W}}{r}$	$+ \rho\overline{u'w'}\,\frac{\overline{W}}{r}$	$- C_k\rho\,\frac{k}{\epsilon}\,\overline{w'^2}\,\frac{\overline{u'v'}}{r^2}$
	$- \frac{\partial}{\partial x}\left[C_k\rho\,\frac{k}{\epsilon}\,\frac{(\overline{u'w'})^2}{r}\right] - \frac{\partial}{r\partial r}\left[C_k\rho\,\frac{k}{\epsilon}\,\overline{v'w'}\,\overline{u'w'}\right] - C_k\rho\,\frac{1}{r}\,\frac{k}{\epsilon}\left[\overline{u'w'}\,\frac{\partial\overline{u'w'}}{\partial x} + \overline{v'w'}\,\frac{\partial\overline{u'w'}}{\partial r}\right]$		
$\overline{v'w'}$	$- \rho(\overline{v'^2} - \overline{w'^2})\,\frac{\overline{W}}{r}$	$- \rho\overline{v'w'}\,\frac{\overline{V}}{r} + \rho\overline{w'^2}\,\frac{\overline{W}}{r}$	$+ C_k\rho\,\frac{k}{\epsilon}\,\frac{1}{r}\,\overline{v'w'}\,\frac{\partial}{\partial r}(\overline{v'^2} - \overline{w'^2})$
	$\frac{\partial}{\partial x}\left[C_k\rho\,\frac{k}{\epsilon}\,\overline{u'w'}\,\frac{(\overline{v'^2}-\overline{w'^2})}{r}\right] + \frac{\partial}{r\partial r}\left[C_k\rho\,\frac{k}{\epsilon}\,\overline{v'w'}\,(\overline{v'^2}-\overline{w'^2})\right] - 4C_k\rho\,\frac{k}{\epsilon}\,\frac{1}{r}\,\overline{v'w'}\,\frac{\overline{w'^2}}{r}$		
	$+ C_k\rho\,\frac{1}{r}\,\frac{k}{\epsilon}\,\overline{u'w'}\,\frac{\partial(\overline{v'^2}-\overline{w'^2})}{\partial x}$		
$\overline{u'w'}$	$- \rho\overline{u'v'}\,\frac{\overline{W}}{r}$	$- \rho\overline{u'w'}\,\frac{\overline{V}}{r}$	$+ C_k\rho\,\frac{k}{\epsilon}\,\frac{1}{r}\,\overline{v'w'}\,\frac{\partial\overline{u'v'}}{\partial r}$
	$\frac{\partial}{\partial x}\left[C_k\rho\,\frac{k}{\epsilon}\,\overline{u'w'}\,\frac{\overline{u'v'}}{r}\right] + \frac{\partial}{r\partial r}\left[C_k\rho\,\frac{k}{\epsilon}\,\overline{v'w'}\,\overline{u'v'}\right] + C_k\rho\,\frac{k}{\epsilon}\,\frac{\overline{u'w'}}{r}\,\frac{\partial\overline{u'v'}}{\partial x} - C_k\rho\,\frac{k}{\epsilon}\,\overline{w'^2}\,\frac{\overline{u'w'}}{r^2}$		

Diffusion d_{ic}

As in the Reynolds stress modeling, the diffusive effects related to the pressure and velocity are neglected. Diffusive transport of the fluxes is considered only to be influenced by the triple correlation $\overline{u_i' u_j' c'}$. However, although a number of approaches have been employed to model the transport equation for this correlation, they have generally been regarded as being too complex for practical applications. The model used in this work is that based on the Daly and Harlow [22] gradient-diffusion approximation. Thus, the diffusive transport of the scalar fluxes is modelled by:

$$D_{ic} = \frac{\partial}{\partial x_k} C_c \rho \frac{k}{\epsilon} \overline{u_k' u_m'} \frac{\partial \overline{u_i' c'}}{\partial x_m} \tag{60}$$

Pressure–Scalar Gradient Interaction Φ_{ic}

Following the same method as used by Chou [20], an expression for the pressure–scalar gradient interaction term can be obtained from the Poisson equation, in the form of the two point correlation given below:

$$\begin{aligned} \overline{\frac{P'}{\rho} \frac{\partial c'}{\partial x_i}} = & \underbrace{\frac{1}{4\pi} \int_{Vol} \overline{\left[\frac{\partial^2 u_l' u_m'}{\partial r_l r_m} \right]^* \frac{\partial c'}{\partial r_i}} \frac{dVol}{|\underline{r}|}}_{\Phi_{ic_1}} \\ & - \underbrace{\frac{1}{2\pi} \frac{\partial \overline{U_l}}{\partial x_m} \int_{Vol} \overline{\frac{\partial u_m'}{\partial r_l}^* \frac{\partial c'}{\partial x_i}} \frac{dVol}{|\underline{r}|}}_{\Phi_{ic_2}} \end{aligned} \tag{61}$$

As in the Reynolds stress equations, the two components of the above equation are modelled separately, one part being concerned with interaction between turbulence quantities, the other term reflecting turbulence/mean-strain interaction.

The turbulent part of the interaction process, Φ_{ic_1}, is modelled following the proposal of Monin [27]:

$$\Phi_{ic_1} = -C_{c_1} \rho \frac{\epsilon}{k} \overline{u_i' c'} \tag{62}$$

The second part of the interaction term is also modelled using identical assumptions to those applied to its counterpart in the pressure–strain term giving:

$$\Phi_{ic_2} = C_{c_2} \rho \overline{u_k' c'} \frac{\partial \overline{U_i}}{\partial x_k} \tag{63}$$

In contrast to the model for Φ_{ij}, that for Φ_{ic} in this work is not augmented by a correction term to account for near-wall effects.

By adopting the same notation as that used in equation 54, the complete modelled form of the scalar flux equation can now be presented in both Cartesian tensor

Table 5: R_{ic} terms in the Scalar Flux Equations

$\overline{u'_i c'}$	Convection	Production	Diffusion
$\overline{u'c'}$	—	—	—
$\overline{v'c'}$	$+\rho\overline{w'c'}\,\frac{\overline{W}}{r}$	$+\rho\overline{w'c'}\,\frac{\overline{W}}{r}$	$-\frac{\partial}{\partial x}C_c\rho\left(\frac{k}{\epsilon}\frac{\overline{u'w'}}{r}\overline{w'c'}\right)-\frac{\partial}{r\partial r}C_c\rho\left(\frac{k}{\epsilon}\overline{v'w'}\,\overline{w'c'}\right)$ $-C_c\rho\frac{k}{r\epsilon}\left(\overline{u'w'}\frac{\partial\overline{w'c'}}{\partial x}+\overline{v'w'}\frac{\partial\overline{w'c'}}{\partial r}+\overline{w'^2}\frac{\overline{v'c'}}{r}\right)$
$\overline{w'c'}$	$-\rho\overline{v'c'}\,\frac{\overline{W}}{r}$	$-\rho\overline{w'c'}\,\frac{\overline{V}}{r}$	$\frac{\partial}{\partial x}C_c\rho\left(\frac{k}{\epsilon}\frac{\overline{u'w'}}{r}\overline{v'c'}\right)+\frac{\partial}{r\partial r}C_c\rho\left(\frac{k}{\epsilon}\rho\overline{v'w'}\,\overline{v'c'}\right)$ $+C_c\rho\frac{1}{r}\frac{k}{\epsilon}\left(\overline{u'w'}\frac{\partial\overline{v'c'}}{\partial x}+\overline{v'w'}\frac{\partial\overline{v'c'}}{\partial r}-\overline{w'^2}\frac{\overline{w'c'}}{r}\right)$

form, ($\beta = 0$), and that describing a two-dimensional axisymmetric swirling flow, ($\beta = 1$), through the following equation:

$$\begin{aligned}\frac{1}{r\beta}\frac{\partial}{\partial x_k}\left[\rho r\beta\overline{U_k}\,\overline{u'_i c'}\right] = \frac{1}{r\beta}\frac{\partial}{\partial x_k}\left[r\beta C_c\rho\overline{u'_k u'_m}\frac{k}{\epsilon}\frac{\partial\overline{u'_i c'}}{\partial x_m}\right]\\ -\rho\overline{u'_i c'}\frac{\partial\overline{U_i}}{\partial x_k}-\rho\overline{u'_i u'_k}\frac{\partial\overline{C}}{\partial x_k}\\ -C_{c_1}\rho\frac{\epsilon}{k}\overline{u'_i c'}\\ -C_{c_2}\rho\overline{u'_k c'}\frac{\partial\overline{U_i}}{\partial x_k}+\beta R_{ic}\end{aligned} \tag{64}$$

where R_{ic} contains the "additive" fragments of convection, production and diffusion arising in the scalar flux equation due to the coordinate transformation, which is given in Table 5.

Finally, it should be said that the turbulence energy dissipation rate, ϵ, appearing in the modeling of the diffusion, redistribution and dissipation of the stresses and fluxes, is determined from its own transport equation which, for two-dimensional, axisymmetric flow, takes the form:

$$\frac{1}{r}\frac{\partial}{\partial x_k}\left[\rho r\overline{U_k}\epsilon\right] = \frac{1}{r}\frac{\partial}{\partial x_k}\left[C_\epsilon r\rho\overline{u'_k u'_m}\frac{k}{\epsilon}\frac{\partial\epsilon}{\partial x_m}\right]+C_{\epsilon 1}\frac{\epsilon}{k}P_{kk}-C_{\epsilon 2}\rho\frac{\epsilon^2}{k} \tag{65}$$

Table 6: Constants Employed in the Reynolds Stress Transport Model (RSTM)

C_1	C_2	C_{p1}	C_{p2}	C_k	C_s	C_ϵ	$C_{\epsilon 1}$	$C_{\epsilon 2}$	C_c	C_{c1}	C_{c2}	κ
1.8	0.6	0.5	0.3	0.22	0.0578	0.18	1.44	1.92	0.11	3.0	0.5	0.42

The values of all of the constants appearing in the Reynolds stress, scalar flux and dissipation equations, used in this work are given in Table 6.

5 Experimental Results

This section presents the isothermal and the initial combustion measurements. General flow features are described and difficulties encountered in the data acquisition process are discussed.

5.1 Isothermal LDV

The first task was to examine the flow to see if it could be considered axisymmetric; this would reduce the future work load required for data acquisition and considerably aid CFD comparisons. Thus, four sets of data were collected, these being, the mean velocities ($\overline{U}, \overline{V}, \overline{W}$), the Reynolds normal stresses ($\overline{u'^2}$, $\overline{v'^2}$, $\overline{w'^2}$) and the Reynolds shear stresses ($\overline{u'v'}, \overline{u'w'}$) along two horizontal and two vertical radii. All of the LDV data was recorded together with upstream flow parameters.

It was observed that the LDV data taken from any of the four radii were very similar, as anticipated, due to the deliberately chosen axisymmetric combustor configuration. A comparison of the mean axial flow velocity measured along a horizontal and a vertical radius is shown in Figure 20. There are some small discrepancies in the region where the swirl air jet impinges on the combustor wall.

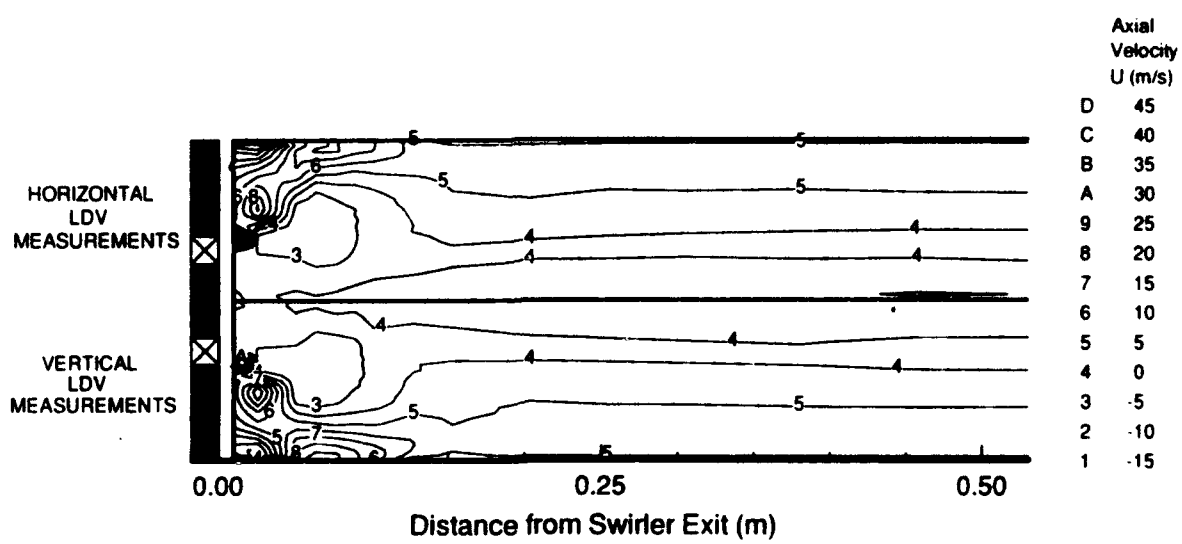

Figure 20: Comparison of Axial Velocity Data Measured Along a Horizontal and a Vertical Combustor Radius

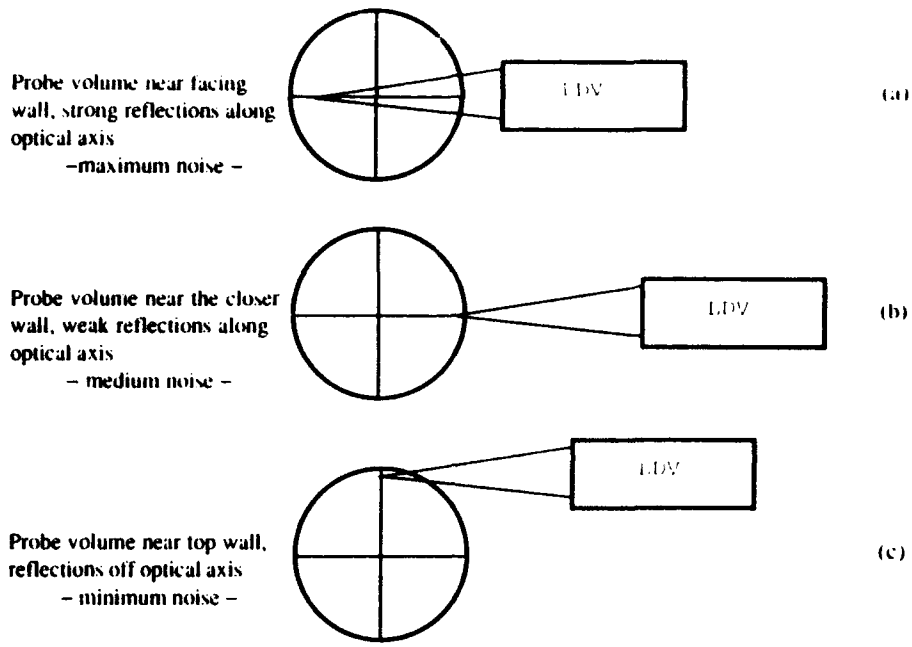

Figure 21: Schematic of LDV Measurement Noise Problem

Near–wall velocities measured along a horizontal radius were marginally smaller than those corresponding velocities measured on a vertical radius. The discrepancies were attributed to signal noise problems caused by reflections off the combustor internal wall at various locations, as shown schematically in Figure 21. The greatest noise problem is experienced when the probe volume is on the horizontal diameter and close to the opposing combustor wall, Figure 21a. Here, strong reflections off the combustor wall, caused by the intensity and closeness of the probe volume to the wall, are propogated back down the LDV optical axis to the collection optics. Figure 21b shows the probe volume position still on the horizontal diameter but further away from the opposing wall. This position still experiences signal noise problems but not as much as the near wall position due to weaker reflections. The LDV probe position at the top of the vertical diameter such as that illustrated in Figure 21c experiences no problems with signal noise since the wall reflections are not along the optical axis. These observations were confirmed when flowmeter measurements were compared with the integrated axial velocity profiles. Integrated velocity profiles collected on vertical radii gave a much closer match to the flowmeter measurements compared to data collected from the horizontal radii. Furthermore, the velocity data collected from the horizontal radius nearer to the LDV gave a closer match to the flowmeter data when compared to the other horizontal radius.

This near wall signal noise problem has clear implications for the future combustion measurement phase. It is now known that the most reliable data are obtained along a vertical radius. Thus, in the future, when a full three–component LDV system is made available, the probe volume should ideally track along a vertical radius

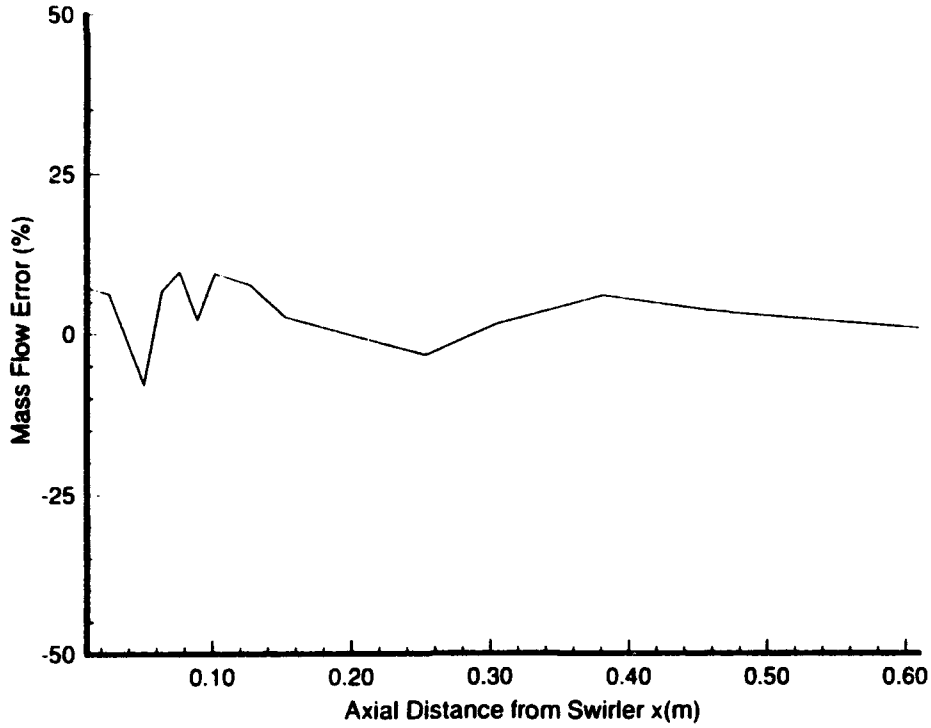

Figure 22: Comparison of Mass Flow Rates Calculated — LDV Data and Flowmeter Measurements

to obtain the best data. The new Rolls–Royce designed test section will permit this.

The difference in mass flow rates obtained from the integration of the axial velocity profiles and the mass flow rates measured using a flowmeter during the experiments, is illustrated as a mass flow error in Fig. 22. The integrated mass flows were calculated to be within $\pm 10\%$ at worst. The larger mass flow errors were observed to be within the range $x = 0.050 - 0.127m$. Observing Fig. 20 this region can be identified with having a large near–wall velocity, thus, when the LDV velocities are integrated with respect to the radius, to calculate the mass flow, any errors in the near–wall velocities magnify errors in the integrated mass flows due to the circular geometry of the combustor. The process of integrating the velocities to obtain the mass flow is only possible when the gas density is known, such as in the case of isothermal flows or in combusting flows where the LDV is coupled with CARS instrumentation. However, this procedure illustrates the value of the isothermal phase of this program by allowing a thorough test of this flow configuration and the associated diagnostics.

Having examined the validity of the data and shown that the flow can be considered axisymmetric, the general features are now described by reference to detailed velocity profiles.

The axial component profiles, Figure 23, show two reverse flow regions, one in the corner extending to $x = 0.046m$, and a larger one in the central region extending all the way down to the last measurement station at $x = 0.609m$, where x refers to the axial distance from the swirler face. Due to optical access the

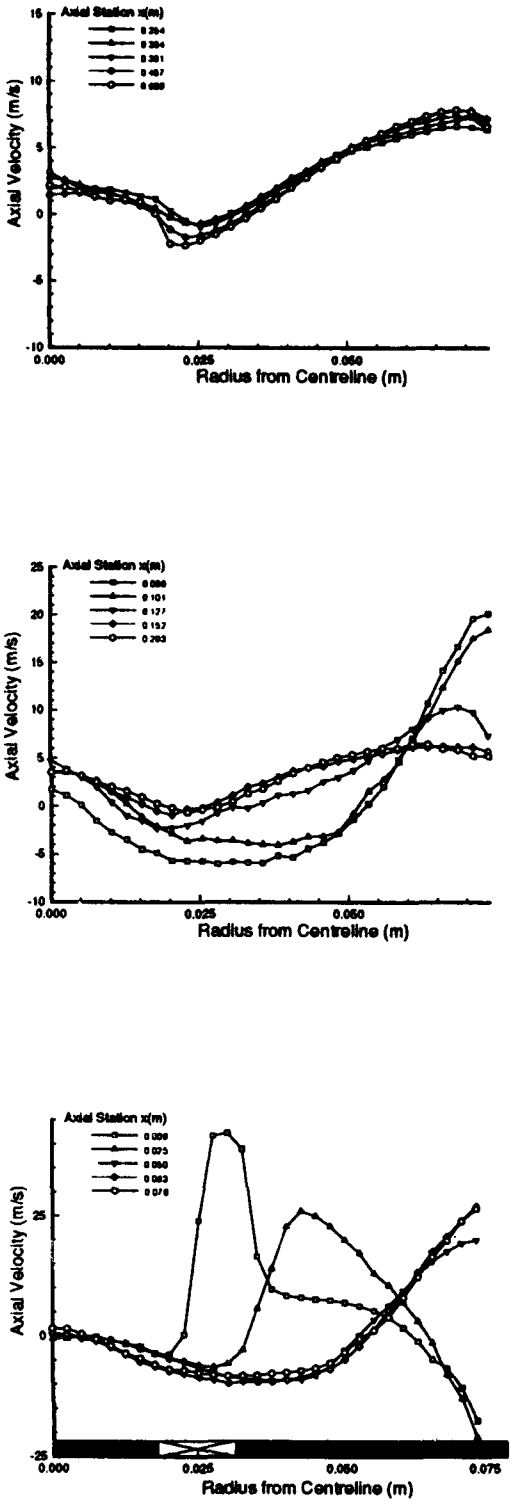

Figure 23 Measured Mean Axial Velocity at Various Axial Stations

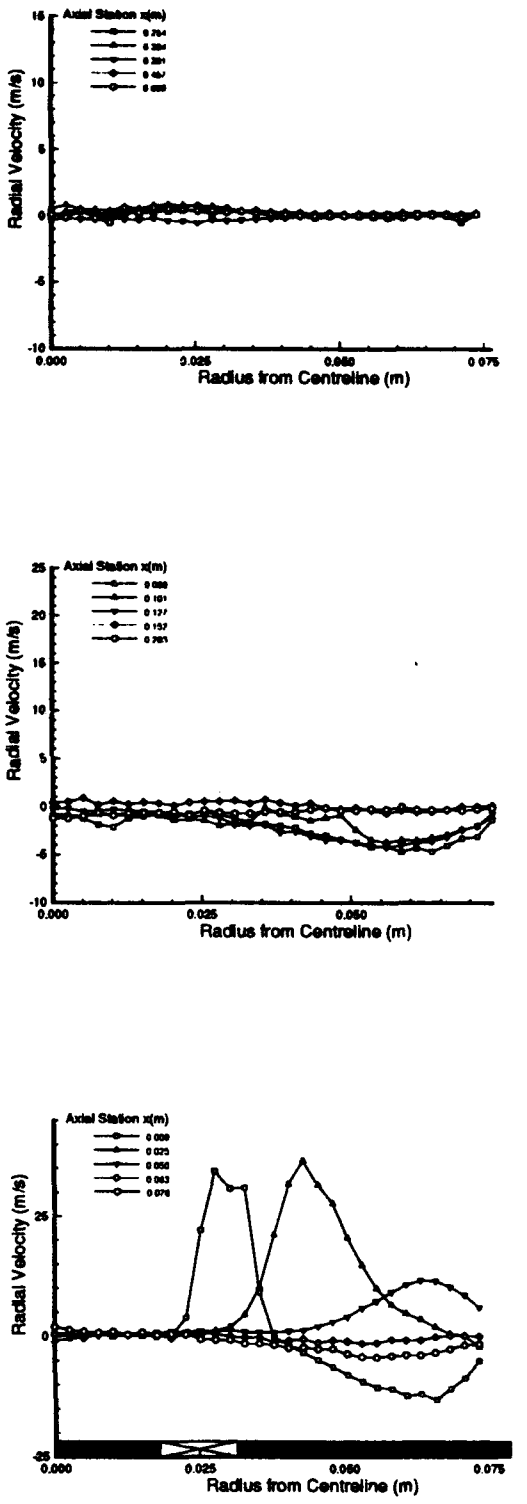

Figure 24 Measured Mean Radial Velocity at Various Axial Stations

closest measurement plane was at $x = 0.009m$. The axial velocity here shows quite clearly a high peak due to the jet issuing out of the swirler. This peak rapidly decays and moves quickly towards the combustor wall. It becomes clear that the majority of the forward flowing mass is very close to the combustor wall. The axial velocities undergo much change from one axial station to another and it isn't until $x = 0.609m$ that little change in the axial velocity profiles is seen. Observing the axial velocity profiles one can see that the axial flow does not fully recover after vortex breakdown, there is still a region of reverse flow at the last measurement plane. This phenomenon has been reported before by So et al. [30] and Wilhelmi [1] and represents a subcritical flow region. With a given mass flow of $0.083kg/s$ and an air density of $1.169kg/m^3$ an average axial air velocity of $3.9m/s$ is calculated, this is much smaller than the maximum swirl velocity of $24m/s$ (later indicated in Figure 25) which is the Squire [31] condition for subcritical flow.

Measured mean radial velocities are shown in Figure 24 and are of the same order of magnitude as the axial velocities, an important factor since it is known that the boundary conditions exert an important influence on the modeling results, [32,33]. The radial velocity drops quite rapidly and is near zero for $x \geq 0.06m$. The first profile ($x = 0.009m$) shows large values of radial velocity as the jet starts to move towards the combustor wall. The radial extent of the corner recirculation zone can be identified between the combustor wall and halfway along the radius, where the radial velocity direction is inward; this zone is rotating counter–clockwise. The corner recirculation zone is quite short as only the "tail" can be seen at the second profile ($x = 0.025m$). At $x = 0.063m$ the radial velocity becomes negative again across nearly the whole diameter, this marks the axial position of the center of the larger recirculation zone with a positive radial velocity (towards the combustor wall) on the upstream side and a negative radial velocity on the downstream side, identifying this zone as clockwise rotating. The center of this vortex is located approximately at $r \simeq 0.0533m$ and $x = 0.061m$, where r is the radial distance from the combustor centerline.

In Figure 24b the majority of the profiles have a negative or inward flow which shows the change of direction of the jet after impinging on the combustor wall. The jet then flows back away from the combustor wall and adjusts itself to be parallel to the combustor axis as shown in Figure 24c.

Observing Figure 25, the swirl velocity is little changed after $x = 0.050m$. What little change there is in swirl velocity is seen near the combustor wall, where the swirl velocity decreases with increasing axial distance along the combustor as the combustor wall exerts more influence on the flow due to friction. Due to symmetry, zero swirl velocities would be expected along the combustor centerline, Figure 25 shows near zero velocities which are probably due to experimental error and slight assymetries in the flow. At $x = 0.009m$ the flow behaves in a swirling jet-like fashion with a weak solid body rotation around the combustor axis. Beyond $x = 0.152m$ (one combustor diameter) the peak in swirl velocity becomes more pronounced and

remains in the same radial position, $r = 0.0244m$, which incidently corresponds to the radial position of the center of the swirler annulus. The near centerline solid body rotation increases in strength as is demonstrated by the increasing swirl velocity gradient. However, the outer region of the flow attains a near constant swirl velocity.

The axial pressure gradients and the friction effects exerted by the combustor wall cause the swirl velocity to decay near the wall as is clearly seen in Figure 25c. Towards the combustor exit the rotating flow comprises two regions, an inner region of solid body rotation (forced vortex) and an outer free vortex region; this combined flow is known as a Rankine vortex, [34]. It is very interesting to note that the swirl velocity gradient does not change significantly in the core region (which implies a very small shear stress in this area) while it gradually loses its strength in the near-wall region. In spite of this, the rotating flow is still strong at the end of the measurement zone indicating a strong, highly swirling jet flow.

Figure 26 illustrates the turbulent axial velocity profiles. The first profile for $x = 0.009m$ shows two peaks in σ_u, these correspond to the two shear layers on the inner and outer edges of the jet issuing from the swirler. The dip between these two peaks marks the jet core. A similar phenomenon can be seen on the measurements of σ_v and σ_w illustrated in Figures 27 and 28. The axial turbulent velocity increases down the combustor until $x = 0.025m$ where it starts to decrease. The peak of σ_u at each axial location is moving radially outwards as the jet develops. The overall value of σ_u decreases with axial distance as the turbulent energy is dissipated.

Comparing Figures 26, 27 and 28 it can easily be seen that the turbulent velocity components are not the same, that is, the turbulence is anisotropic. The high values of the turbulence intensity indicate high gradients of velocity or better mixing. For example, in the near field most of the activity will be around the jet where the velocity is much higher than the surroundings. Further downstream, the jet diffusion and mixing is near completion except for the very low energy regions around the centerline. Again, this is where mixing is taking place and the turbulence values are expected to be higher than the surroundings, as shown in Figures 26, 27 and 28.

It is also noticed that the turbulence levels increase on the centerline further down the combustor, this could be due to a precessing vortex core (PVC). A PVC is a periodic tri-dimensional instability which affects the turbulence levels by spuriously increasing them above the "true" turbulent values. This happens as the center of the vortex precesses around the combustor axis, so at one moment in time the LDV probe volume may be measuring the radial velocity and at another moment in time, the same laser beams may be measuring the swirl velocity, within the same experiment. As a result, measurements of radial velocity near the centerline may contain contributions from the swirl velocity and vica versa. Consequently, on analysis of the LDV data, the values of the turbulence levels are seen to be larger than expected. In a steady-state calculation, it is not possible to pin down the motion of the PVC and hence, its presence will not be reflected in calculations of

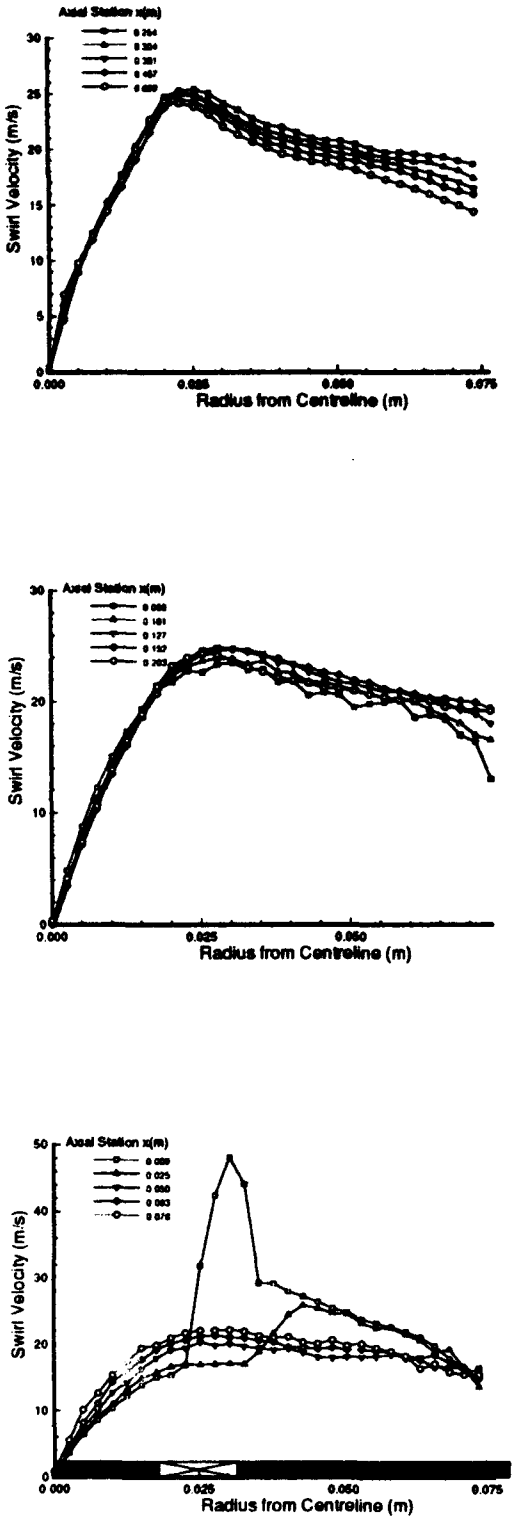

Figure 25 Measured Mean Swirl Velocity at Various Axial Stations

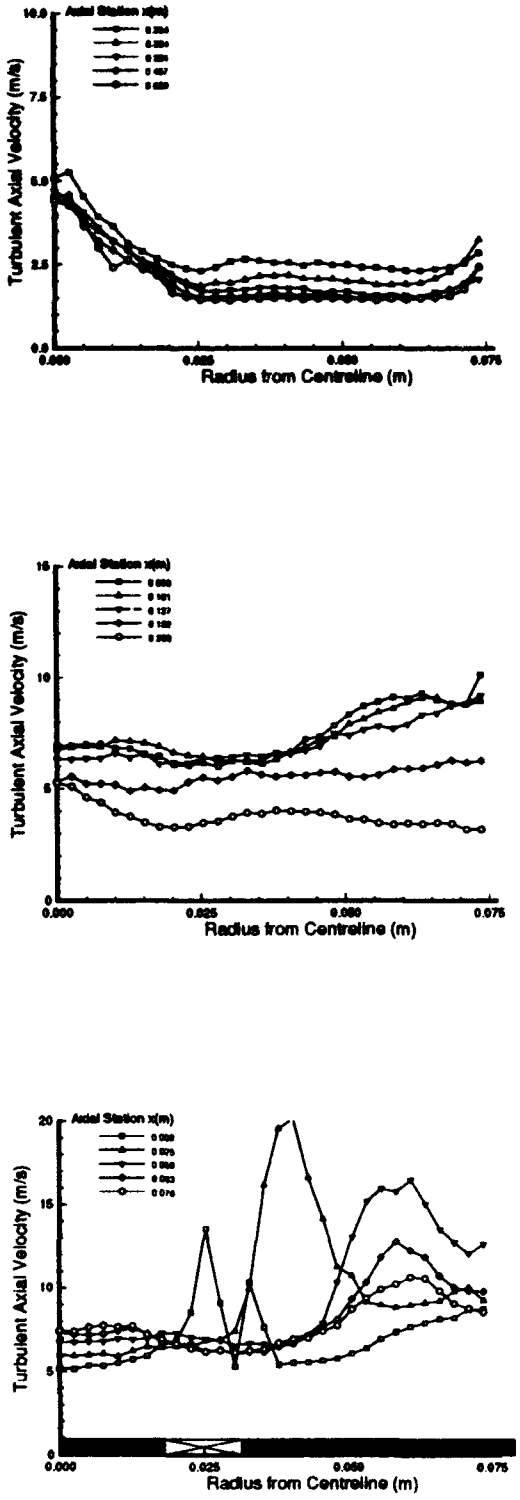

Figure 26 Measured Turbulent Axial Velocity at Various Axial Stations

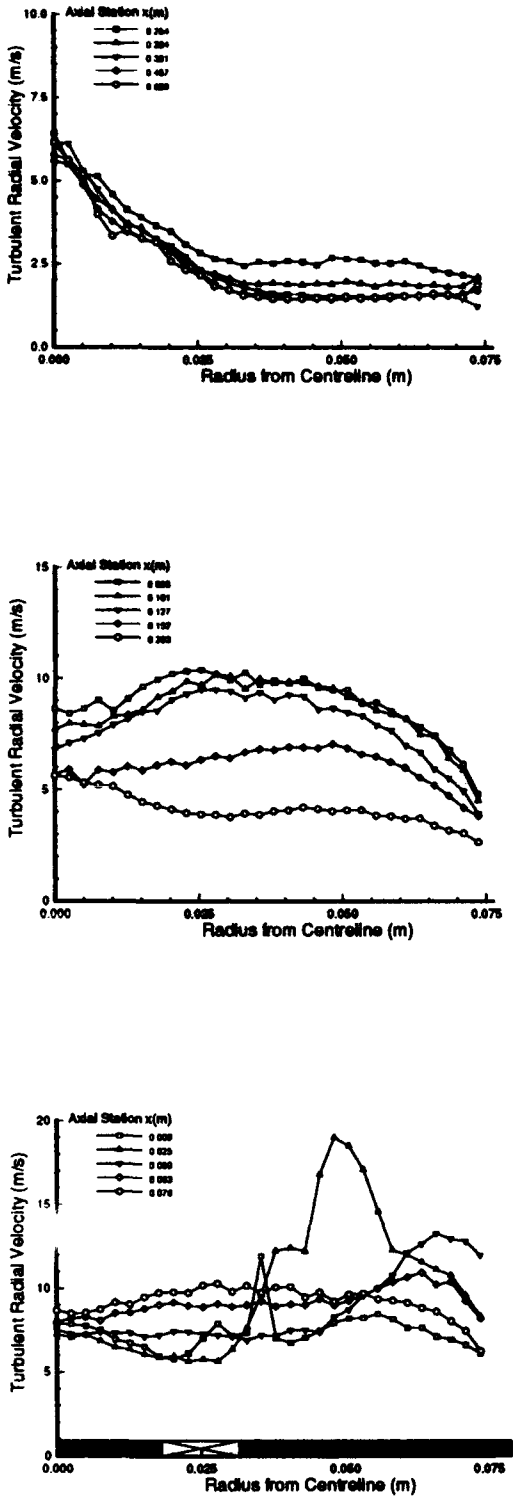

Figure 27 Measured Turbulent Radial Velocity at Various Axial Stations

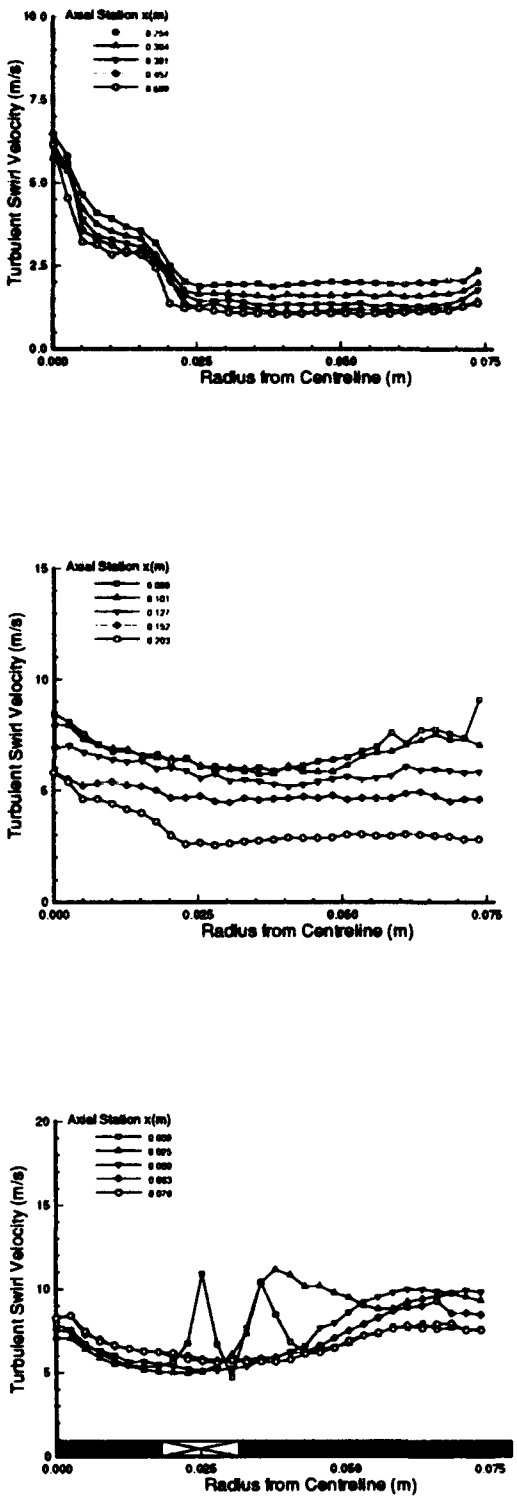

Figure 28 Measured Turbulent Swirl Velocity at Various Axial Stations

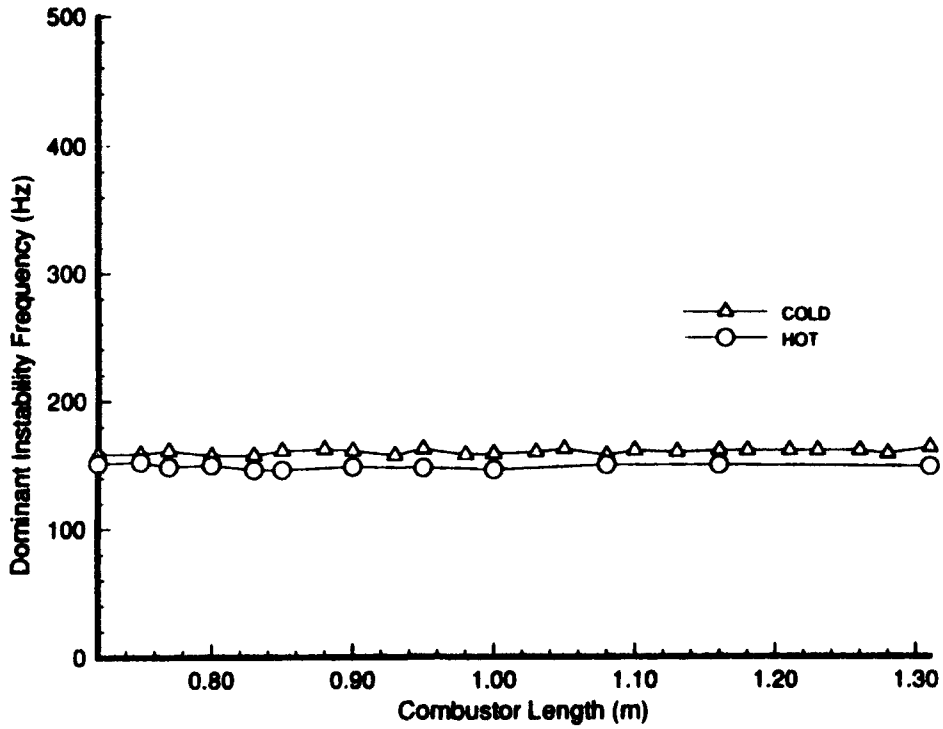

Figure 29: Investigation of Dominant Frequency in Combustor with Changing Combustor Length

normal stress levels.

Overall, it was observed that the axial gradients in velocity and stresses were found to be very steep within the first $150mm$ downstream from the swirler, this presents interpolation difficulties when using the data for CFD validation. Consequently, it is recommended that more axial data stations should be included in future work. An additional 20 locations are suggested, resulting in a resolution of $5mm$ axially and $2.5mm$ radially within $150mm$ of combustor length.

5.2 Flow Instabilities

For visualization purposes, fast action movies were taken of the combusting flowfield through a temporarily installed quartz cylinder acting as the combustor. It was noticed that there was a regular fluctuation of the flame front and structure in the axial direction. This phenomenon pointed to some sort of instability that needed to be understood and removed.

Many measurements were taken of combustor pressure fluctuations and swirl air feed line pressure fluctuations with pressure transducers. These were analyzed with a Fast Fourier Transform technique. From these measurements the instability was suspected to be of an acoustic nature rather than a combustion instability. When the combustor was run at an equivalence ratio of $\Phi = 0.65$ a dominant frequency of $160Hz$ was observed, both in the upstream swirl air feed line and in the combustor, see Figure 29. This dominant frequency remained unchanged with changing combustor length which implied that the source could be an acoustic effect

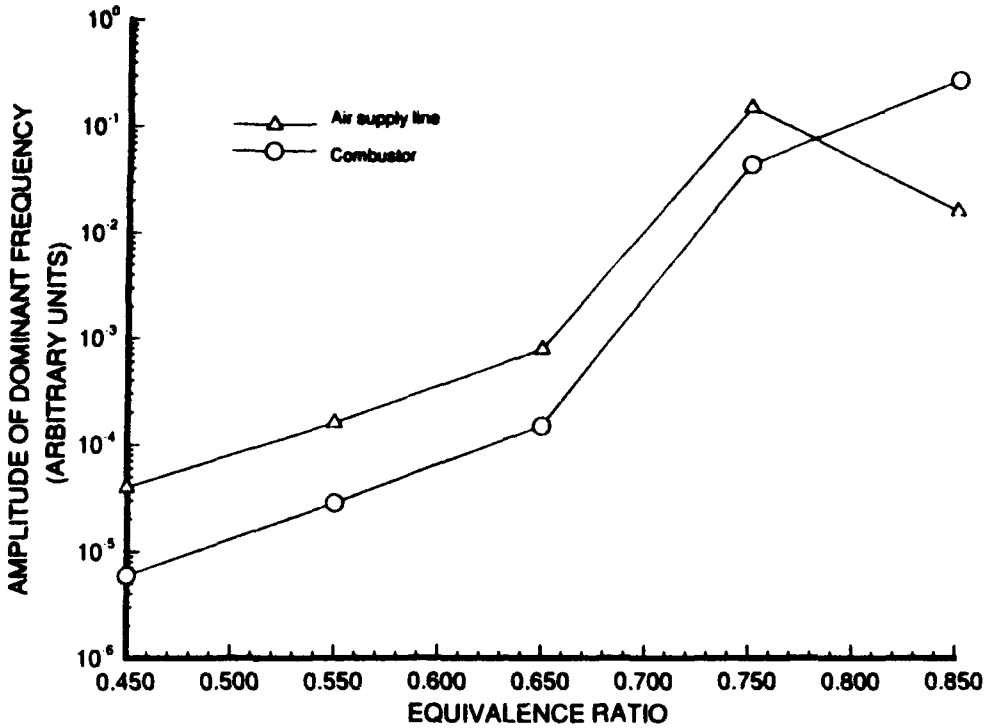

Figure 30: Change in Amplitude of Dominant Combustor Frequency with Changing Equivalence Ratio

related to the fixed geometry of the swirl air feed line. It was also observed that the amplitude of this dominant frequency of $160Hz$ decreased by a factor of more than 1,000 when the equivalence ratio was decreased from 0.85 to 0.45, see Figure 30. The route taken to eliminate the flow instability at $160Hz$ was to run the combustor at a lower equivalence ratio of $\Phi = 0.45$, thereby, reducing the amount of energy available to excite this acoustic instability. This was indeed done, and no further instabilities were detected.

At higher equivalence ratios other smaller amplitude instability frequencies were detected. One such frequency of $\approx 90Hz$ was found to be related to the length of the upstream settling chamber. This particular frequency was removed by inserting a choke plate downstream of the settling chamber to acoustically decouple the settling chamber from the combustor.

5.3 Combustion LDV

The combustion LDV phase of this research program has not yet started, but Gould and Benedict [28] have made some initial measurements during their summer faculty visit to the Wright Laboratory in the Summer of 1992. A significant result was that it was necessary to operate the TSI two-component LDV system in a forward scatter mode in order to get a strong enough signal for analysis. A degradation of the seed material during combustion is suspected as the cause. The only combustor available at the time of these experiments was the WL stainless steel water cooled combustor, already introduced in Section 2.3. Thus, the velocity and Reynolds

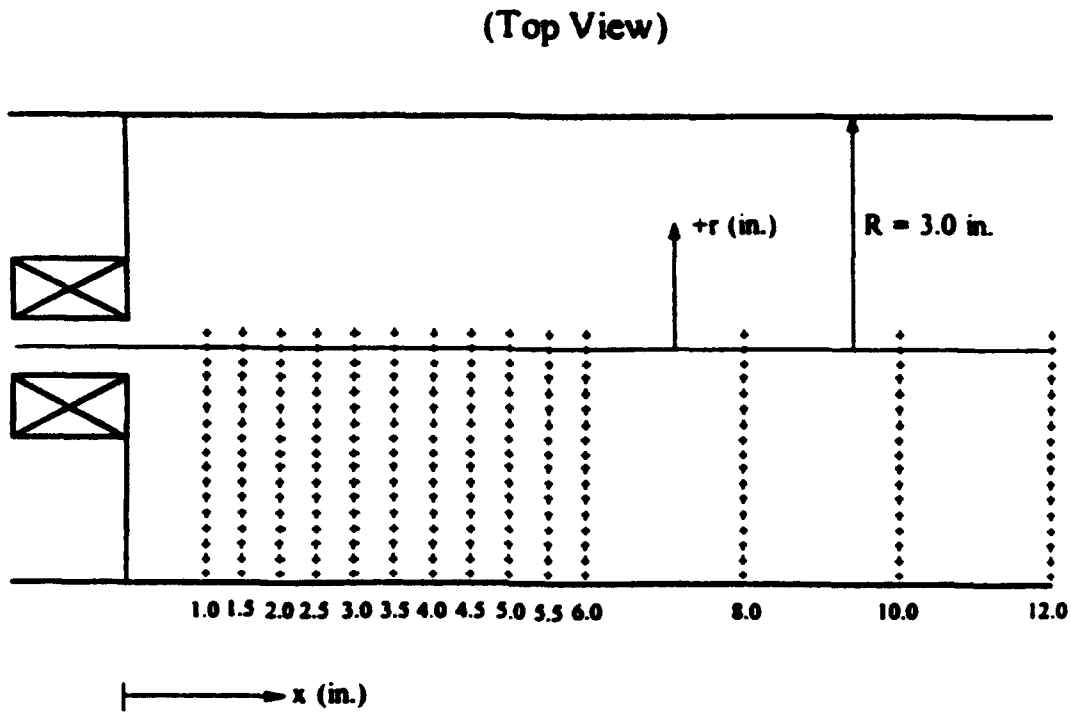

Figure 31: LDV Combustion – Measurement Locations (Gould and Benedict)

stress field data lacked all the radial components which are required for a full CFD validation. Furthermore, the use of the WL water cooled combustor restricted the LDV measurements to be made along a horizontal radius, which, according to what was learned in the isothermal phase, is not the best radius to make measurements due to LDV signal noise caused by laser reflections off the combustor wall.

The LDV system was orientated to make direct measurement of the axial and tangential velocity components on the diameter of the test section. Measurements were made at 16 radial locations and at 14 axial planes as indicated in Figure 31. The $514.5\mu m$ argon laser line was used to measure the axial velocity component while the $488\mu m$ argon laser line was used to measure the tangential velocity component. Full details may be found in Reference [28].

Gould and Benedict, as part of their summer program, also made single-point temperature measurements. This was done by manually traversing a type S Platinum/10% Platinum-Rhodium unshielded thermocouple probe across the radius of the test section at each axial plane. The mean temperature at each point was calculated by averaging 225 temperatures sampled over a 10 second period.

The flowfield was seeded by the same titanium dioxide chemical seeder used for the isothermal LDV measurements, Craig et al. [6]. Data validation rates varied between 10,000 and 200 per second on each counter processor and depended mainly on how clean the quartz windows were and the location in the flowfield. Low data validation rates occurred in the central recirculation zone and near the windows. Coincident data validation rates ranged from 3,000 to 50 measurements per second. The procedure used for eliminating spurious data caused by noise, is explained by

Gould and Benedict [28], the reader is referred to this for full detailed results.

There were three identifiable regions in the combusting flow. There is a corner recirculation zone that remains quite cool and a larger, stronger central recirculation zone that is much hotter. Both of these recirculation zones are maintained by a relatively cool, high velocity jet issuing from the swirler exit. This jet hits the combustor wall then runs parallel to it. The velocity of this jet as expected is much higher than observed in the isothermal case because of expansion due to combustion. A strong central recirculation bubble was found to extend from the swirler to $0.040m$ downstream, whereas, in the isothermal case a reverse flow region was seen to extend $0.609m$ downstream. This is caused by the expansion effect of the combusting flow, where the gaseous products expand so much that they fill up any available regions for reverse flow.

The profiles of the turbulent normal stresses during the first $0.0508m$ are very similar in the hot and isothermal case since, in this near swirler region the turbulence is shear generated. The centerline values of the normal stresses in the hot case are higher than those observed in the isothermal case. This could be attributed to a stronger precessing vortex core (PVC).

The main conclusion to draw from this work is the difficulty experienced in obtaining a good LDV signal in backscatter mode. This is cause for great concern, since the new Rolls-Royce designed test section, although designed for a three-component LDV system, has the requirement that it must operate in back scatter mode. Such a system was chosen since it would require smaller optical ports and thereby, keep to a minimum any flow disturbances caused by these optical ports. There is a growing concern for the survivability of the titanium dioxide seed material, since it decomposes at 1900K. In fact, the seed material is formed by a chemical seeder reacting titanium tetrachloride with water. Investigations by Scientific Research Laboratories [29] have shown this type of seed to be composed of titanium tetrachloride surrounded by a titanium dioxide crust which itself is surrounded by water. As soon as this seed approaches hotter regions (>800K) in the flow it shatters and leaves very little material to scatter the incident laser light. Alternative seeding materials that remain inert and that can better withstand the hostile environment must be found. Techniques for introducing seed materials in a uniform manner must also be investigated.

6 CFD Isothermal Comparisons

The aim of this research program is to provide a data base of good quality data to help in the validation of combustion CFD codes and to further develop the models employed for turbulence and chemistry. This work is carried out with the use of PACE, the Rolls-Royce suite of CFD programs, [1] and [12]. This suite of programs can utilize a $k-\epsilon$ or a Reynolds Stress Transport Model (RSTM). This section presents initial $k-\epsilon$ and RSTM results and compares them with the isothermal data already presented in Section 5.

A two-dimensional polar coordinate system was employed, this is satisfactory, since the experimental results show the flow to be axisymmetric. The modeled domain was from the first measurement plane to the last measurement plane, that is, $x = 0.0096m$– $0.6096m$ and a grid of 31×50 (radial×axial) was employed. A turbulence length scale of $0.035m$ was used; this corresponds to the swirler inlet hub diameter. The inlet boundary conditions were taken from the experimental values and a zero gradient boundary condition was set at the outlet. Particular care had to be taken in transposing the experimental grid values to the numerical grid values due to the velocity staggering techniques used in the code. A hybrid differencing scheme [35] was employed. The model constants used have already been given in Section 4.

For comparison, both the $k-\epsilon$ and the RSTM were employed. Full, detailed results of the numerical predictions are given in Appendix B. Profiles of the axial velocity predictions are shown in Figure 32 along with the measured LDV data. RSTM designates the Reynolds Stress Transport Model predictions and LDV the experimental results. The modeling is started at the axial position $x = 0.0096m$ which corresponds to the first axial position where experimental data are available. Thus, it can be seen that the modeled values of the axial velocity are set equal to the experimental values at this axial location.

It should be noted here that the experimental measurement grid is much coarser than that used for the models (31x15 vs. 31x50) and, therefore, there is not a one–to–one correlation between the experimental grid points and the CFD mesh points. Thus, for the comparisons discussed in this section the CFD results were interpolated onto the experimental measurement grid. This process of interpolation seemed to proceed quite well; however, there are some anomalies in the CFD data which could be attributed to this fitting process.

From Figure 32, at $x = 0.0254m$, the "swirl air jet" is seen to have a higher peak velocity than that modeled and has also moved out further in the radial direction. Generally, up to x=$0.101m$ it seems that the near wall region is not modeled very well, the axial velocities are underpredicted by as much as 60%. The mass flow involved in the central recirculation is grossly underpredicted. In fact, the $k-\epsilon$ model performs better here. After the central recirculation zone ($x = 0.0127m$) the RSTM begins to perform quite well again, correctly predicting the positive

centerline velocity and the thin reverse flow at about $r = 0.025m$ which extends down to the final axial measurement plane. The RSTM unlike the $k - \epsilon$ model, is able to predict the subcritical nature of this strongly swirling flow.

The radial velocities are illustrated in Figure 33. The inlet radial velocity profiles at $x = 0.0096m$ are not exactly the same since the experimental values were interpolated to account for the numerical grid staggering employed in the CFD solution procedure. It is difficult to assess how well the radial velocity has been modeled since, in the most part, it is zero and, therefore, not influential on the subsequent flow development. Also, there is a difficulty in its measurement since, any slight misalignment of the LDV probe volume along the vertical radius of the combustor will result in a measurement that includes a component of swirl, which is quite high throughout the combustor. However, the measured radial velocity has been seen to be mostly zero and this is reflected in the CFD predictions. Again, we see from $x = 0.0254m$ that the swirl jet is modeled as being wider and the peak jet velocity is underpredicted. The modeled radial velocity reduces very quickly towards the wall, where, in fact, at $x = 0.0508m$ it is still quite high.

Observing Figure 34 the RSTM results for the swirl velocity are seen to be very good indeed. The RSTM has captured the swirl velocity profile shape, that is, the inner forced vortex (solid body rotation) and the outer free vortex region. Also, the location of the peak swirl velocity is correctly predicted at about $r = 0.0254m$. Where, in comparison the $k - \epsilon$ model overpredicts the radial diffusion of the angular momentum which results in a solid body rotational flow throughout the diameter of the combustor and a maximum swirl velocity incorrectly predicted near the combustor wall. The RSTM however, does over predict the actual peak value of swirl by as much as 25%, which is still better than that calculated by the $k - \epsilon$ model which gives an overprediction of as much as 50%.

Generally, not much data are available in the literature regarding the Reynolds stresses, in particular the shear stresses. Statistically speaking, the Reynolds stresses are second-moment quantities, whereas, the mean velocities are first moment quantities. Consequently, any errors in the LDV measurement system are further amplified when considering the stress values returned. Thus, measurements of Reynolds stresses should be treated with caution. Bearing this in mind, some comparisons between experimental values and modeled values for Reynolds stresses are presented here for completeness.

Figure 35 shows the axial normal Reynolds Stresses $\overline{u'^2}$. It can be seen that at $x = 0.0096m$ the $\overline{u'^2}$ values for the $k - \epsilon$ model are not the same as the RSTM or experiment. This is because the Reynolds stresses are not defined explicitly in the $k - \epsilon$ code at all, and, therefore, it is impossible to match all six stresses with the freedom of only two variables, that is, k and ϵ. For axial locations it can be seen that the axial stress is consistently measured higher than predicted by either model, in particular, in the near centerline area. However, this apparent increase in turbulence on the centerline may be caused by a precessing vortex core (PVC).

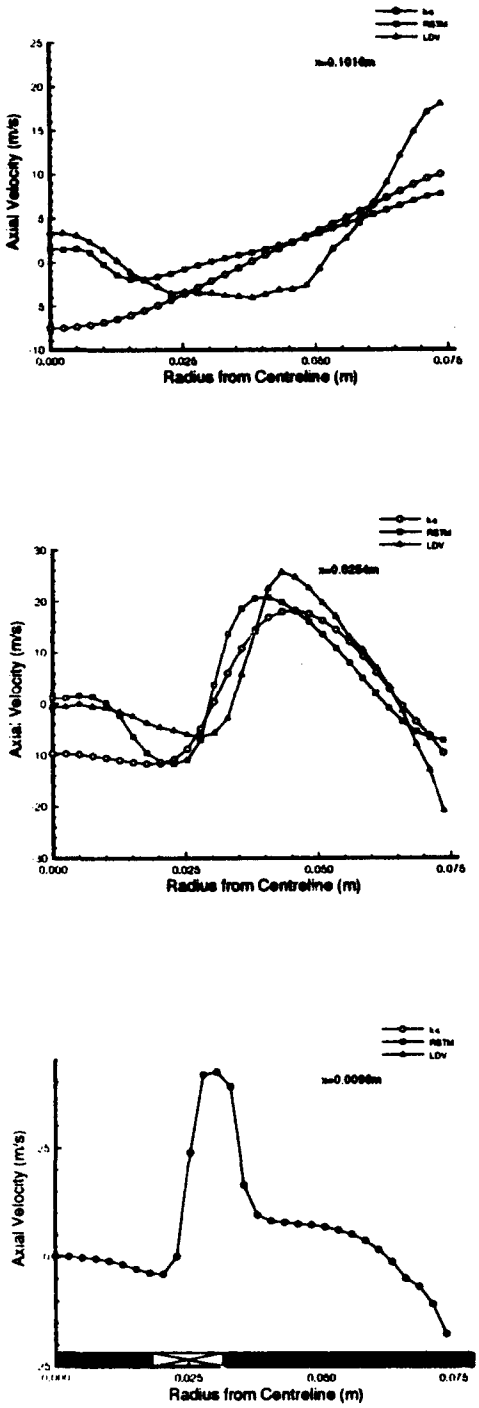

Figure 32 Measured vs. Predicted – Selected Axial Velocity Profiles

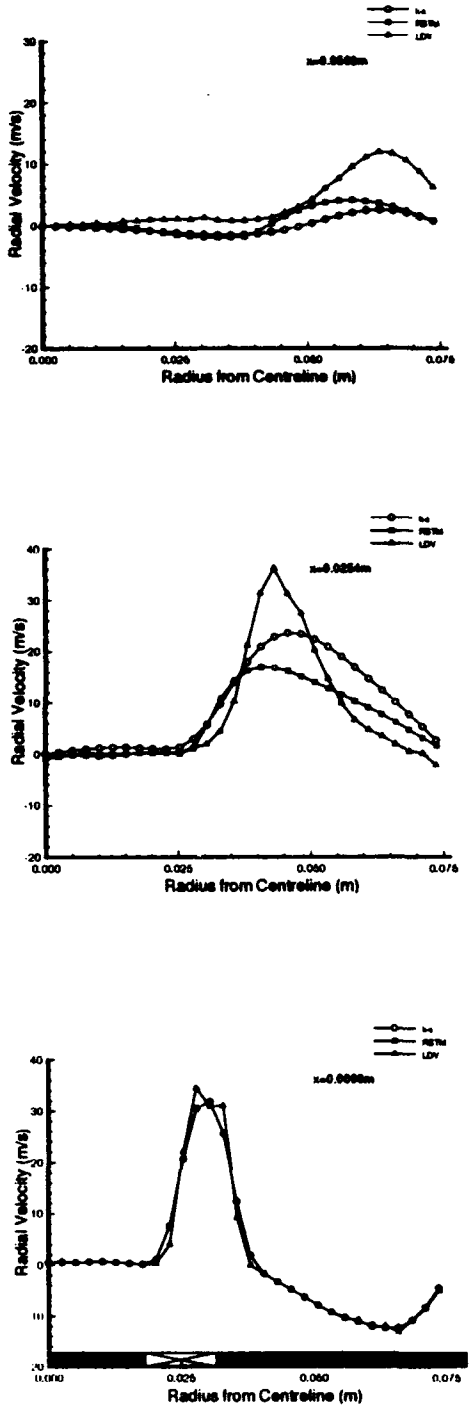

Figure 33 Measured vs. Predicted – Selected Radial Velocity Profiles

as discussed earlier, which of course cannot be predicted with a steady CFD code such as the one used here.

The predicted stresses are of the right order, but the peaks are not high enough. Also, in many cases an increase in $\overline{u'^2}$ was observed near the wall which was not predicted by either model.

Observing Figure 36, again the Reynolds stress $\overline{v'^2}$, is measured higher than predicted, by a factor of 2 to 3. The expected, and observed, decrease in $\overline{v'^2}$ towards the combustor wall is correctly predicted by both models. As the flow progresses downstream, the model predictions $\overline{v'^2}$ become much better, apart from the PVC, which becomes more obvious beyond $x = 0.2032m$. Figure 37 like the results for the other normal Reynolds stresses, shows that the predicted levels of $\overline{w'^2}$ improve as we progress downstream. Again, like the other normal Reynolds stresses, the higher centerline values caused by the PVC are not predicted.

The combined effect of the normal Reynolds stresses is reflected in the profiles of kinetic turbulence energy, Figure 38. After $x = 0.0508m$ both models underpredict k by about 50%, although, they do correctly predict the rising levels of k towards the combustor wall. k remains underpredicted until about $x = 0.2032m$ after which, the RSTM more closely models k. It is at this same point that evidence of the PVC is observed in the high centerline values of k.

It is an over estimation of the shear stresses in the $k - \epsilon$ model that is often cited as the cause of the incorrectly predicted solid body rotation swirl velocity profile in strongly swirling and confined flow configurations. Looking at Figure 39 it can be seen that the RSTM predicts reasonable values of $\overline{u'v'}$ in the downstream region. Whereas, the $k - \epsilon$ model overpredicts the values of $\overline{u'v'}$ by 200%. It is in this downstream region where the $k - \epsilon$ model predicts a solid body rotation type of flow. Again, some unsteadiness can be detected through the values of $\overline{u'v'}$ at the centerline. For a perfectly axisymmetric and steady flow $\overline{u'v'}$ would be expected to be zero at the centerline.

Figure 40 compares the $\overline{u'w'}$ shear stress profiles. All that can be said is that the values of $\overline{u'w'}$ are predicted at the right order.

The $\overline{v'w'}$ stress could not be measured with the optical configuration employed, however, for illustration, the calculated stresses are shown in Figure 41. Since no measurements of $\overline{v'w'}$ were available the calculation assumed $\overline{v'w'}$ to be equal to zero at the model inlet plane, a $\overline{v'w'}$ field is soon generated due to the shear caused by the inlet swirl air. It can be seen that the $k - \epsilon$ model consistently overpredicts the $\overline{v'w'}$ stress field and it is this overpredicition that contributes towards the problem of the $k - \epsilon$ model incorrectly predicting a solid body rotation type of flow. With the $\overline{v'w'}$ stress having such a profound effect on the nature of the flow it would be recommended that efforts should be made in measuring this stress. This will soon be possible if the the new Rolls-Royce designed test section, see Section 2.4 is used in conjunction with a full simultaneous three-component LDV system.

Both the $k - \epsilon$ and RSTM predict velocity fields of the right magnitude but

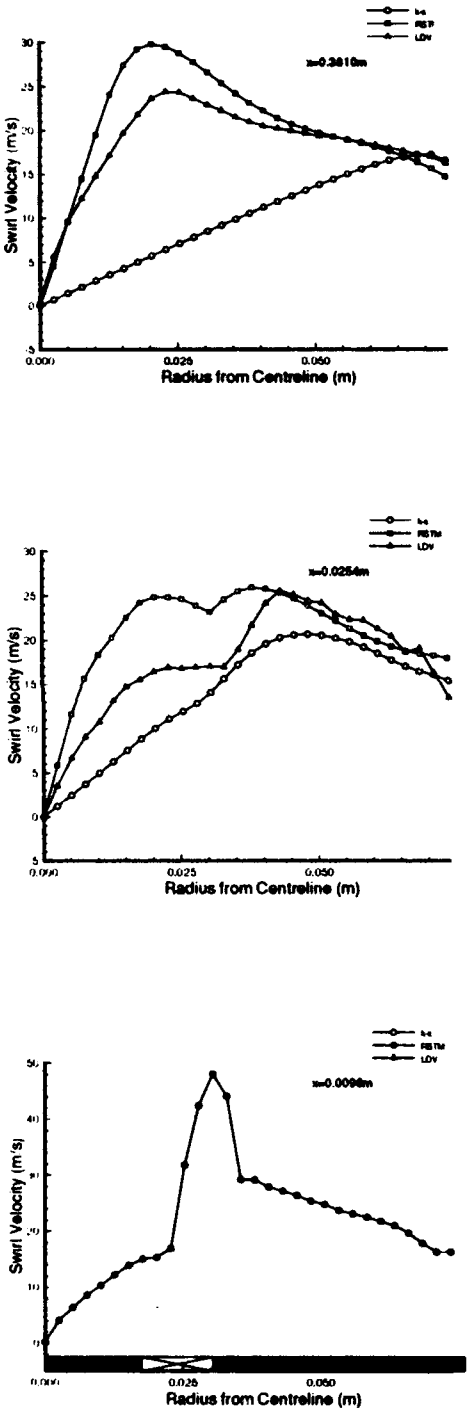

Figure 34 Measured vs. Predicted – Selected Swirl Velocity Profiles

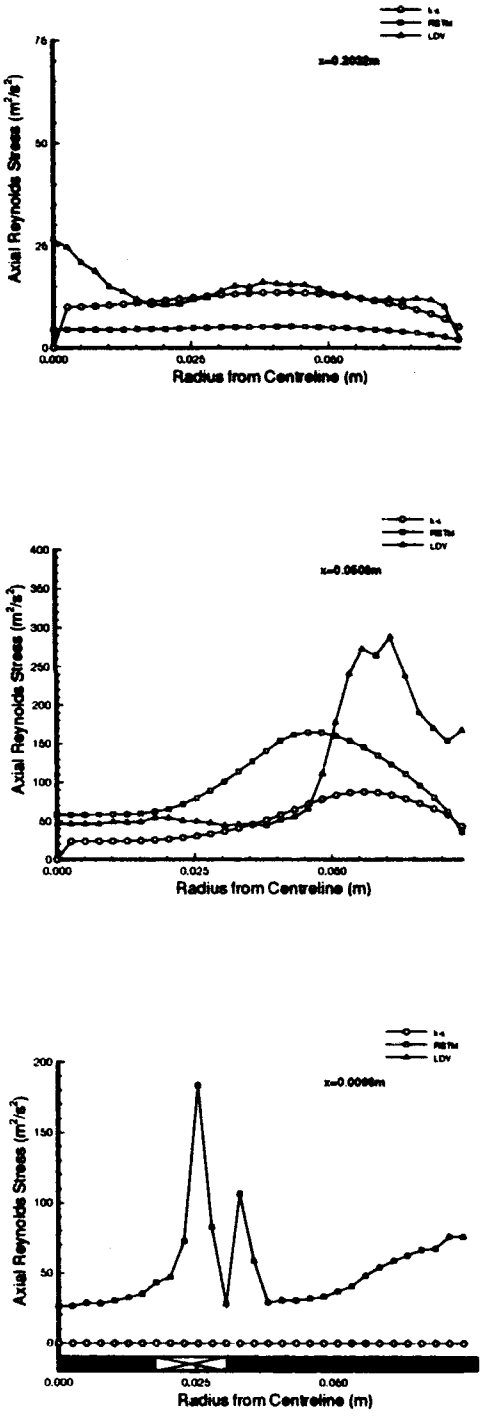

Figure 35 Measured vs. Predicted – Selected Axial Reynolds Stress Profiles

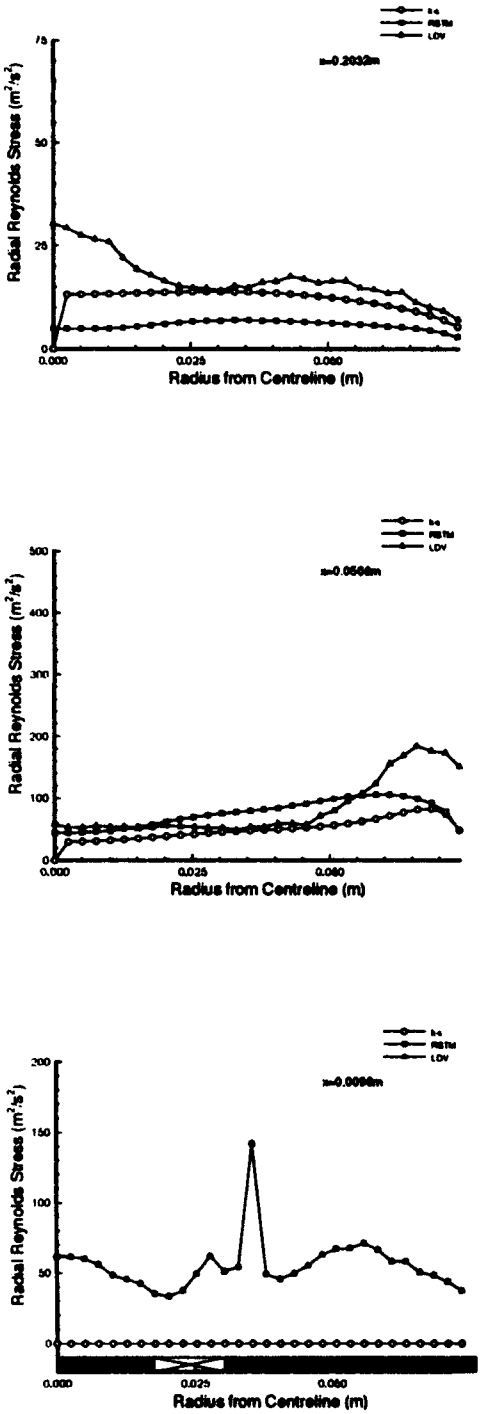

Figure 36 Measured vs. Predicted – Selected Radial Reynolds Stress Profiles

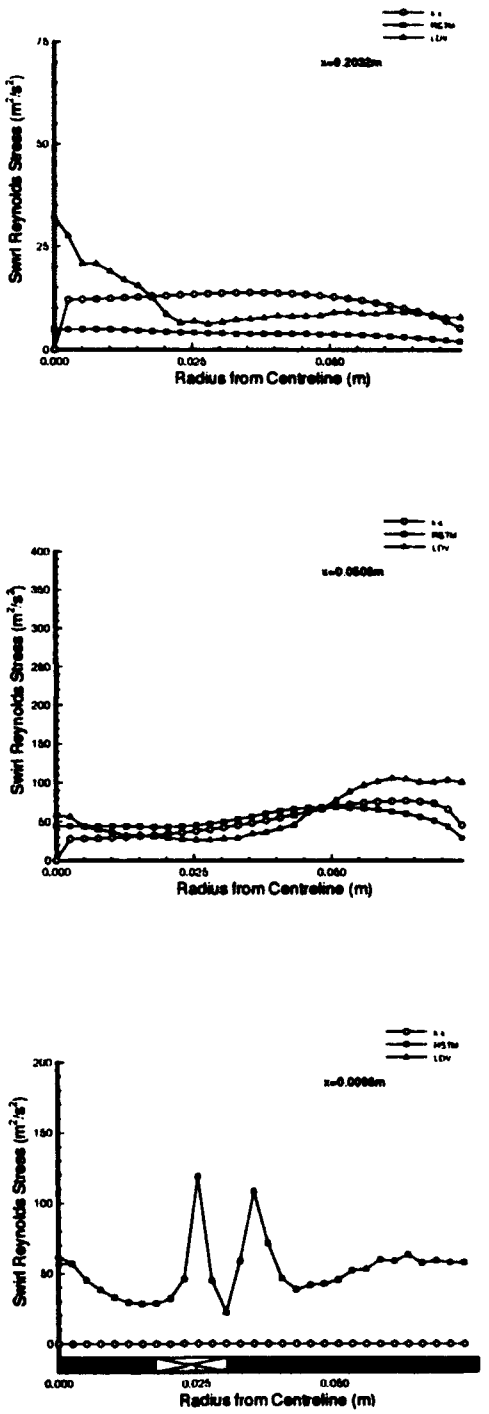

Figure 37 Measured vs. Predicted – Selected Swirl Reynolds Stress Profiles

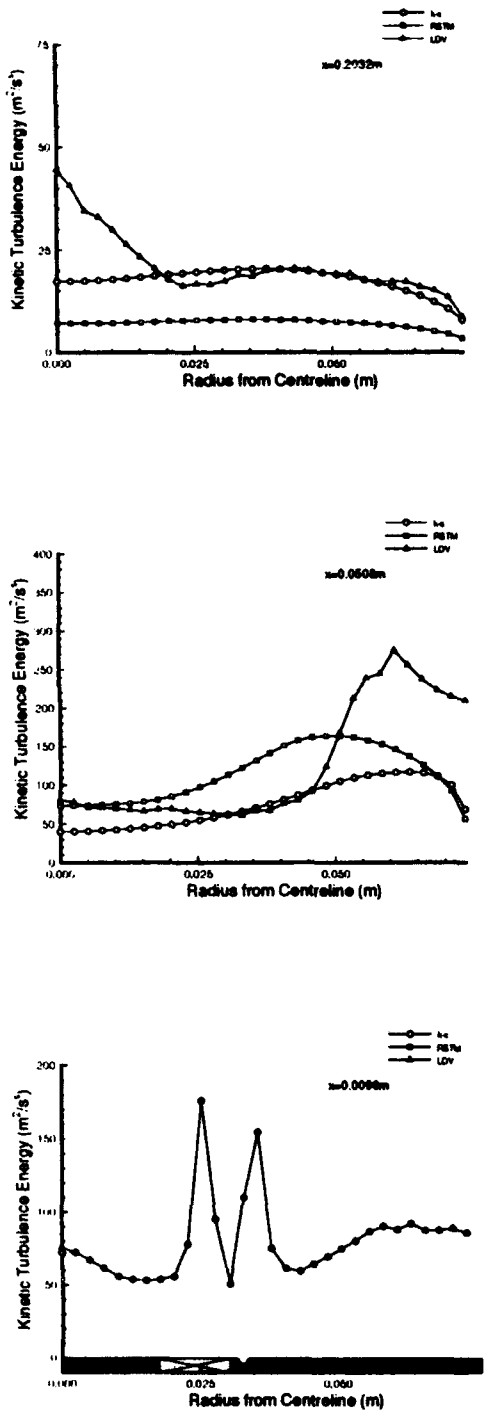

Figure 38 Measured vs. Predicted – Selected Kinetic Turbulence Energy Profiles

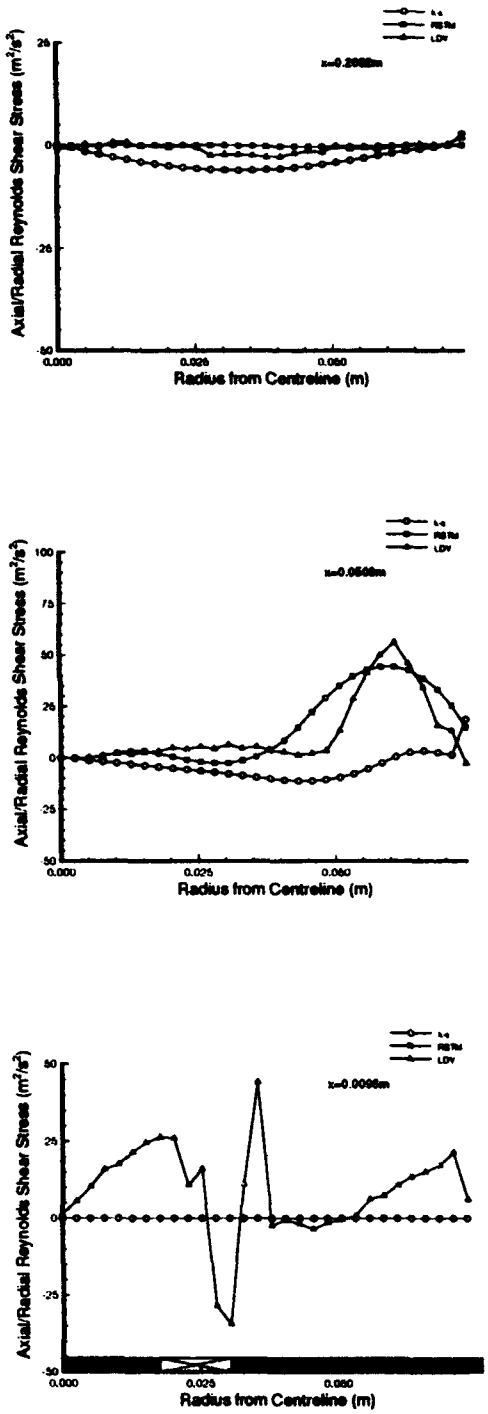

Figure 39 Measured vs. Predicted – Selected Axial/Radial Reynolds Shear Stress Profiles

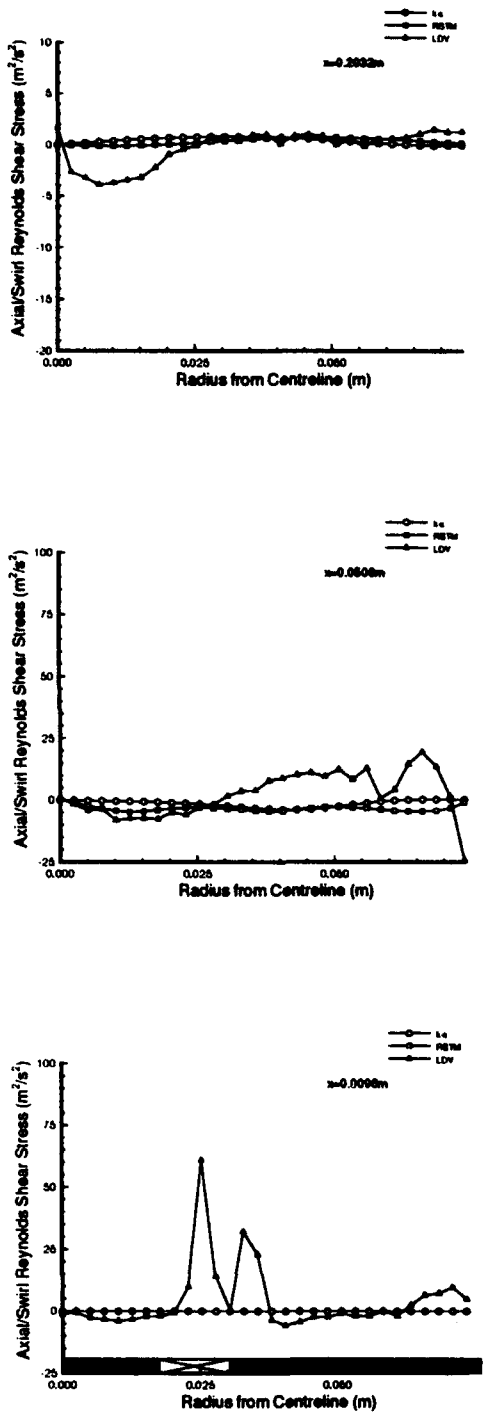

Figure 40 Measured vs. Predicted – Selected Axial/Swirl Reynolds Shear Stress Profiles

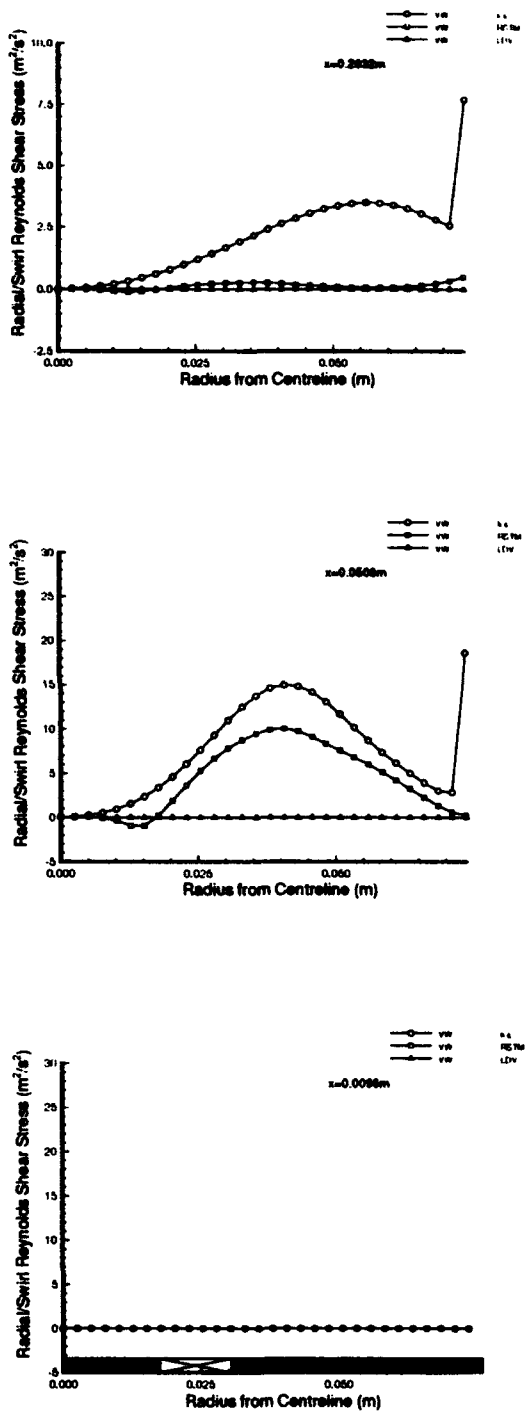

Figure 41 Measured vs. Predicted – Selected Radial/Swirl Reynolds Shear Stress Profiles

only the RSTM captures the subcritical nature of the flow. The mean velocity field predictions for the RSTM are very good, in particular the combined Rankine vortex downstream of the central recirculation zone. However, although it is seen that the stresses are modeled poorly by both models, the RSTM performance is better. It should also be kept in mind that the experimental values are subject to inherent difficulties and should not be taken as fully correct. On this basis it would be recommended to take a closer look at the measured stresses.

Axial gradients in velocity and stresses have been seen to be very steep indeed, particularly within the first $0.150m$ of flow. Since most of the mixing processes occur within this region and it is the region that is most poorly modeled, it is recommended that further measurements should be taken here. The resolution should be increased so that for the first $0.150m$ we have an axial measurement station at every 4 or $5mm$. This will mean an additional 22 axial measurement locations.

7 Program

The aim of this section is to discuss the scheduling achieved to date, to learn from delays already experienced and to put forward a tentative schedule for 1993 1994.

Figures 42, 43, 44, 45 and 46 illustrate the actual scheduling achieved to date. The original work statment [36] anticipated completion of the isothermal and combustion LDV measurements within 7 months of contract start. However, this schedule incorporated the following assumptions:

- Use of the Imperial College quartz tube combustor, and its straightforward installation
- WL facilities would not require extensive modification
- No further hardware would be required
- All necessary optical instrumentation would be readily available

Rolls–Royce and WL agreed to change the facility to be employed. The reasons being, that the originally intended facility in Building 450 was occupied with the work of another program that was running over schedule and that the use of the water–cooled combustor in Building 18 would be preferred over the use of the Imperial College quartz tube combustor, since this WL facility would provide the opportunity to go up to pressure.

This newly adopted facility was modified and a new swirler/injector assembly built because of the difference in size. This took 5.5 months, and consequently, it was October 1990 when the isothermal LDV measurements were started. Despite the extent of the modifications necessary to the facility, this represented very good progress. Also in October 1990, the facility was run hot for the first time to check the combustor characteristics before continuing with the extensive isothermal LDV measurements; no problems were identified at this point, however, some safety modifications to the laboratory were required, which stopped combustion work for the remainder of 1990.

In parallel with the facility modifications and initial trials, PACE, the Rolls-Royce combustion CFD code was installed and compiled on the on-site Silicon Graphics workstation (SGI). Some bugs were experienced and it was not until mid-September 1990 when the first PACE test case was run successfully. With the SGI not being connected to a Rolls–Royce mainframe, further input/output processing routines had to be written; these were not completed until the end of 1990.

Mass flow anomalies were found on the analysis of the isothermal LDV data gathered during October to December 1990, see Section 5.1. It was decided to install the Plexiglas rig (Section 2.2) to enable measurement of all of the velocity components and hopefully gain an insight to this problem. The installation of the Plexiglas rig took 1 month and in February 1991, the isothermal data were retaken.

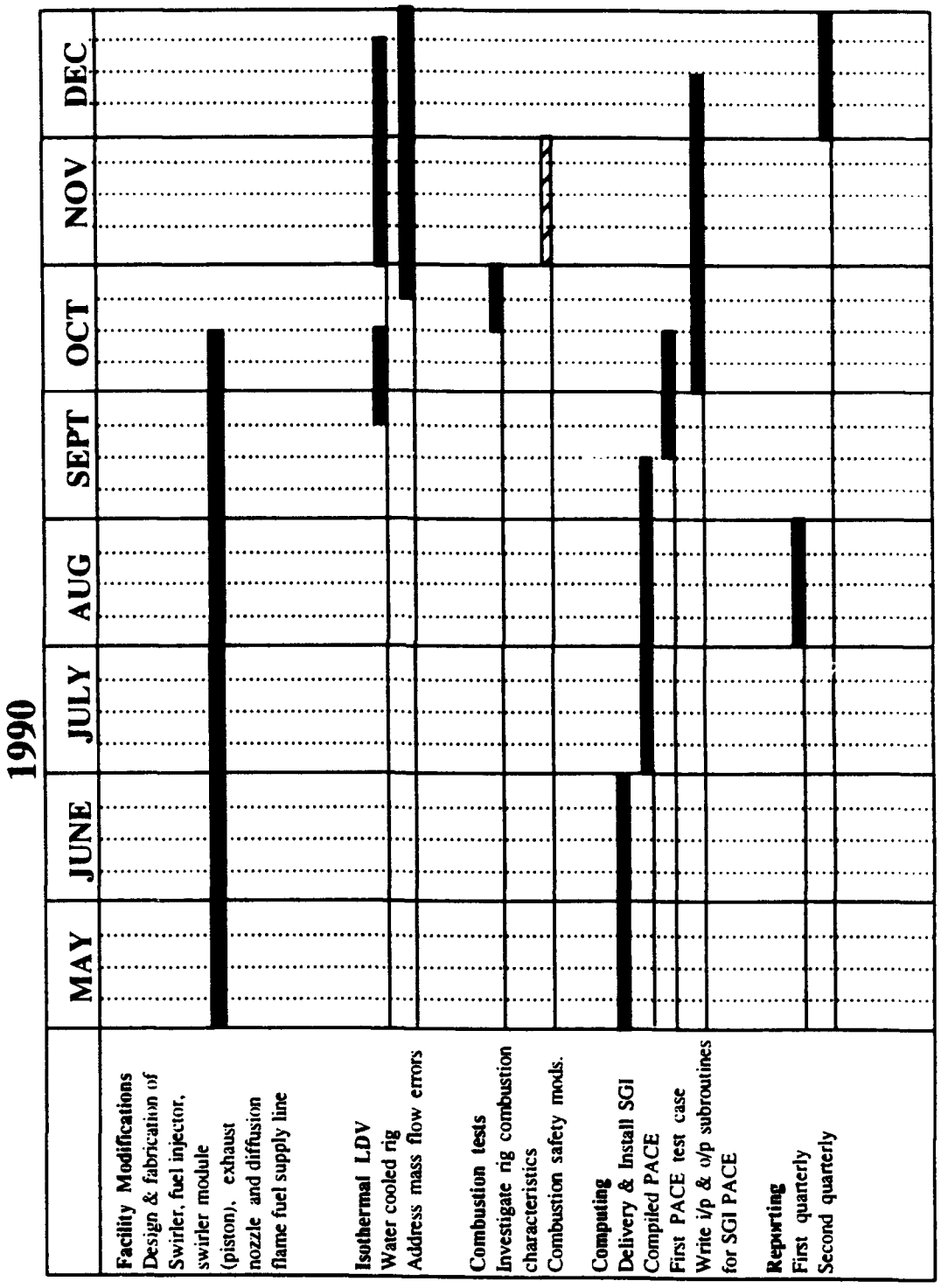

Figure 42: Actual Schedule Achieved — May to December 1990

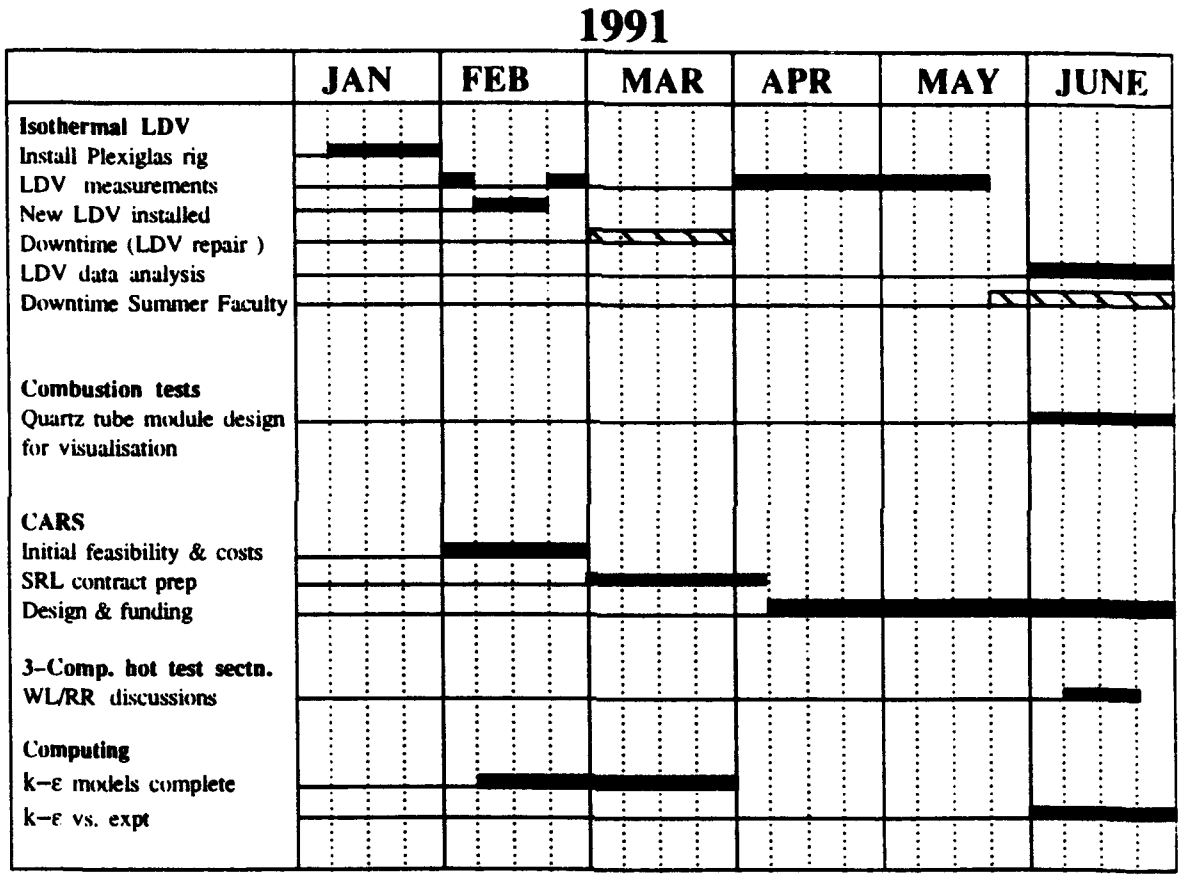

Figure 43: Actual Schedule Achieved — January to June 1991

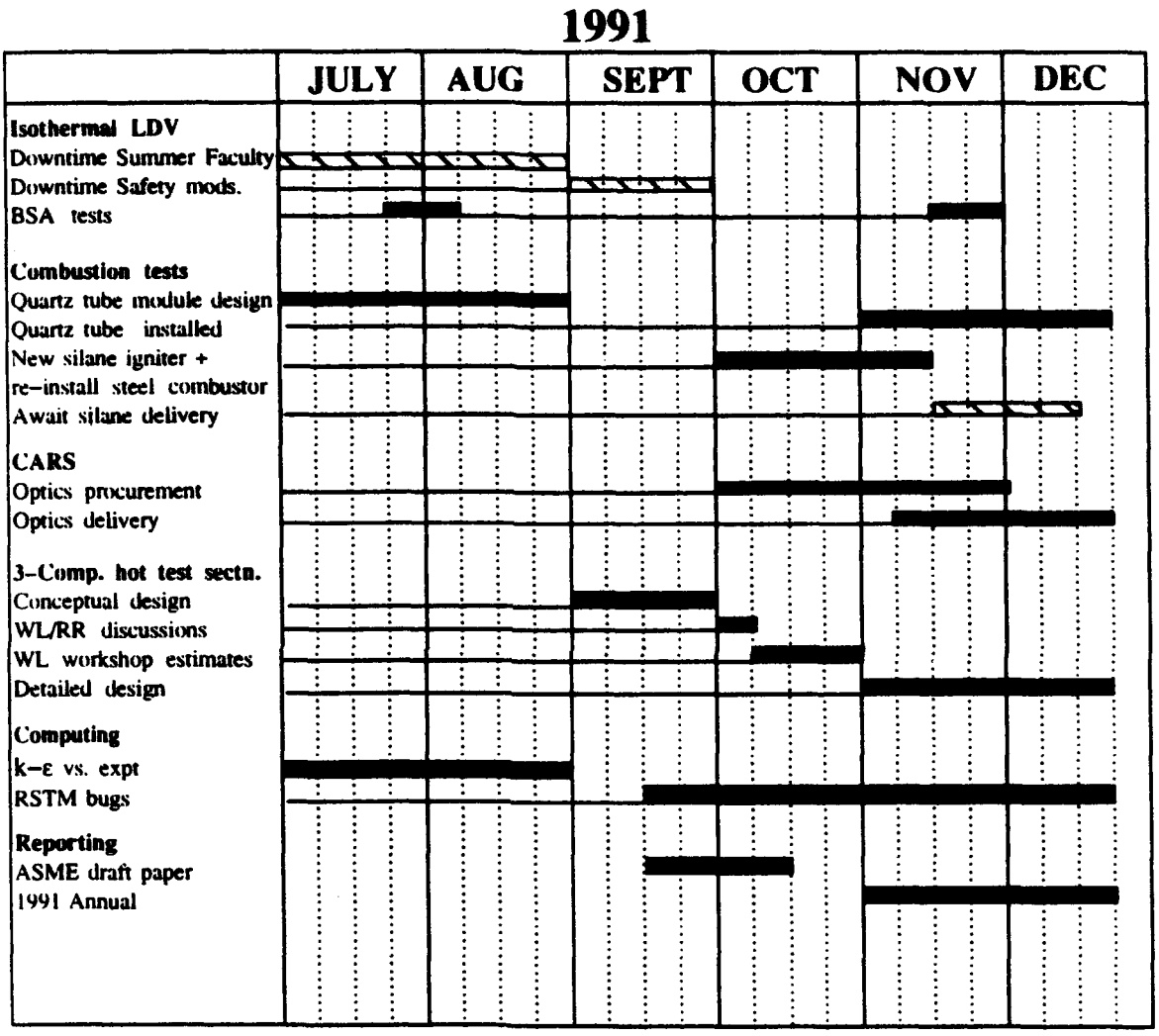

Figure 44: Actual Schedule Achieved — July to December 1991

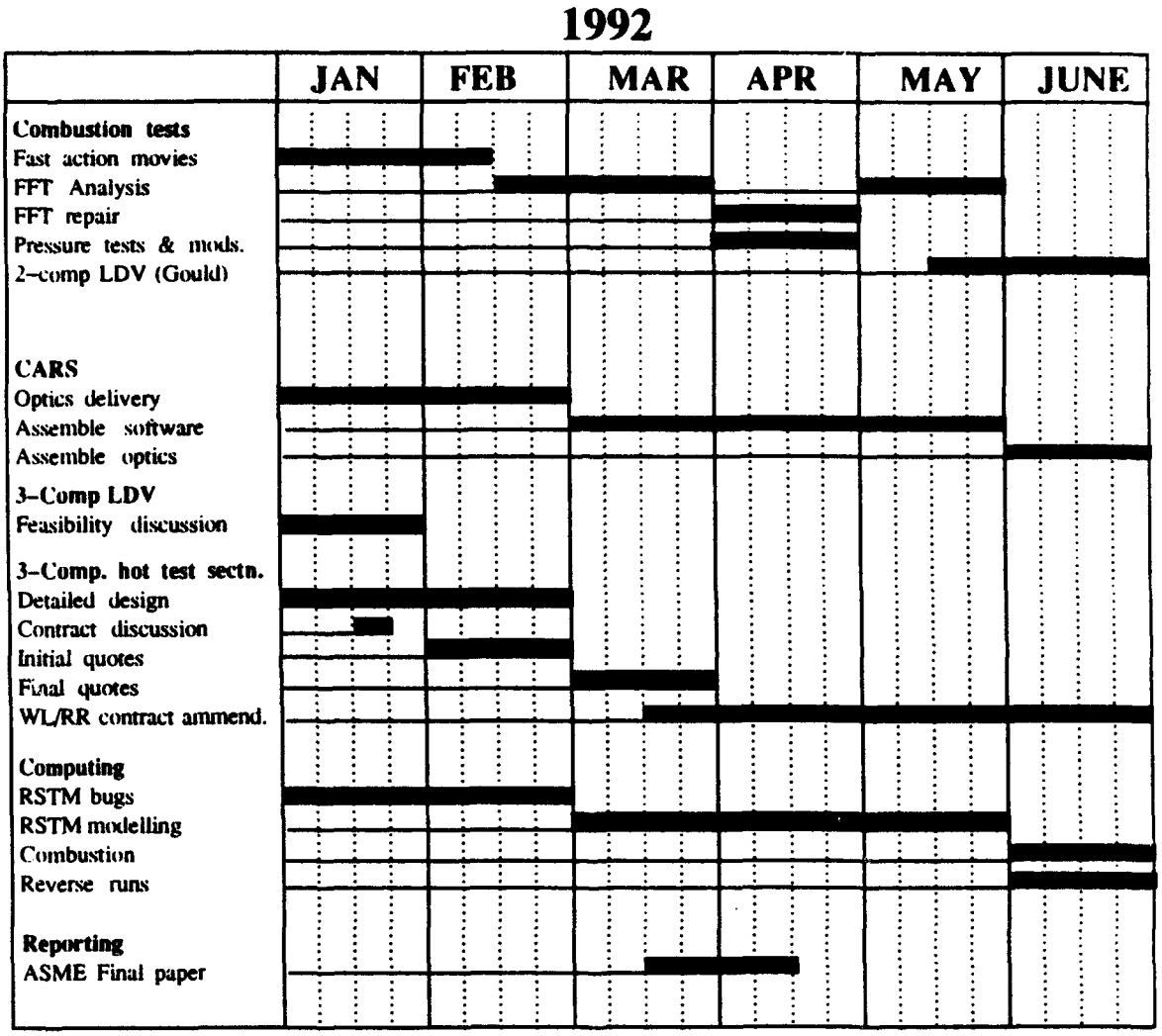

Figure 45: Actual Schedule Achieved — January to June 1992

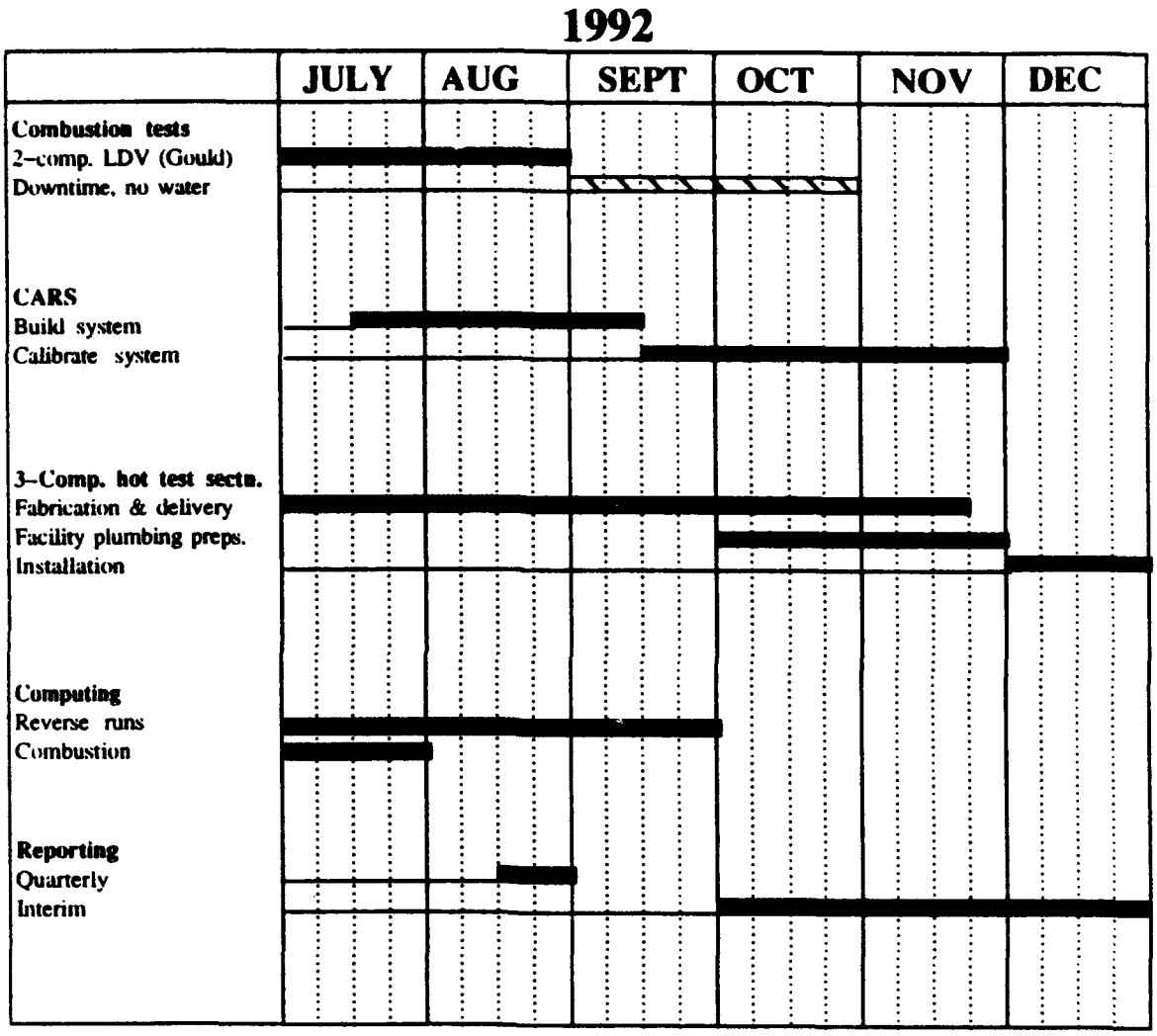

Figure 46: Actual Schedule Achieved — July to December 1992

This was interrupted for 1 month, due to repairs required on the LDV and xyz table but was finally completed in May 1991. Thus from the start of the contract, it took 12 months to obtain a complete set of isothermal data.

All LDV work was stopped at the end of May 1991 to allow access for the summer faculty staff who used the facility for work unrelated to the WL/RR collaborative program. After this, the facility was unavailable for a further month in September 1991 due to required safety modifications. In October 1991, work was started on modifying the ignition system in an effort to provide a smoother ignition and start-up in preparation for a quartz tube to be fitted as a combustor for visulization purposes.

During the final half of 1991 it was decided to design and build a CARS system, as one was not available for this facility. The design of the CARS by SRL was started in April 1991. Funding was difficult to raise and took several months. Initial parts were ordered from October 1991 and deliveries started in November 1991.

Based on the isothermal results, WL and Rolls-Royce agreed that there was a requirement for a combustion test section that would permit LDV access for measurement of all velocity components and all of the Reynolds stresses, see Section 2.4. In September 1991, RR submitted a conceptual design, which was accepted by WL. Detailed design work started in November 1991.

In the early part of 1992, analysis of fast action movies revealed some flow instabilities, Section 5.2. These were further investigated with the use of high response pressure transducers and FFT analysis. At the end of April 1992, these flow instabilities were attributed to the upstream swirl air supply ductwork.

In 1992 affairs were arranged so that the work of the summer faculty research staff contributed to the WL/RR collaborative research program. Consequently, Dr. Gould made some two-component combustion LDV measurements during June-August 1992. After this, the laboratory was unavailable for use for 2 whole months while site-wide maintenance was carried out on the water supply.

Much progress was made on the CARS in 1992. All of the hardware was purchased by March 1992, and assembly was completed in mid-September 1992. Calibration of the CARS continued through to the Christmas break. At present, the CARS instrumentation is completed and is now ready to be installed on the combustion facility.

The detailed design of the three-component hot test section was completed in February 1992, and final quotes for subcontractor fabrication were received in March 1992. There was then a delay of over 3 months before the WL/RR contract was ammended to permit RR to subcontract and oversee the fabrication of the test section. It then took 4.5 months for fabrication and delivery of the section to WL. Installation of the section was then achieved by the end of December 1992.

Reynolds Stress Transport Modeling was attempted in January 1992, and bugs were not addressed until the end of February 1992. RSTM modeling continued up to the end of May 1992.

So, after 32 months a complete set of isothermal LDV data has been obtained, flow intabilities have been addressed and some seeding problems have been identified with the LDV combustion. No useful combustion LDV data for CFD code validation have yet been obtained. However, much development of the facility has been required in order to address the objectives of the original work statement [36]. For instance, there was no CARS available nor a test section that would allow full optical access for a three–component LDV system in a combusting flow. These items could have been obtained more quickly if funding was more readily available and several months could have been saved if contract amendments did not take so long. Now that these items have been obtained, the WL facility offers a great potential for combustion measurements.

Facility downtimes, excluding holidays and vacations, amounted to 7.5 months over a 32–month period. Most of this cannot be reduced, as maintainance and safety modifications are mandatory. However, the summer faculty programs have been put to effective use by doing research directly related to the WL/RR program.

The schedule for the next 24 months is to be formally agreed between WL and RR in early February 1993. However, Figures 47 and 48 illustrate a suggested approach. Now that the CARS instrumentation is available and the new test section is in place, it is recommended that temperature measurements be taken. This would provide a good start to the combustion phase of the program. In parallel with this, combustion LDV seeding problems should be addressed ready for implementation in May 1993 with the arrival of summer faculty staff. During the three–component LDV combustion measurements in summer, the CARS hardware/software should be further developed for species concentration measurements which can be attempted in Fall/Winter 1993.

The schedule for 1994 will much depend on the events of 1993, but efforts should be made to couple the LDV to the CARS system and measurements attempted in the early part of 1994. These could then be followed by measurements at pressure.

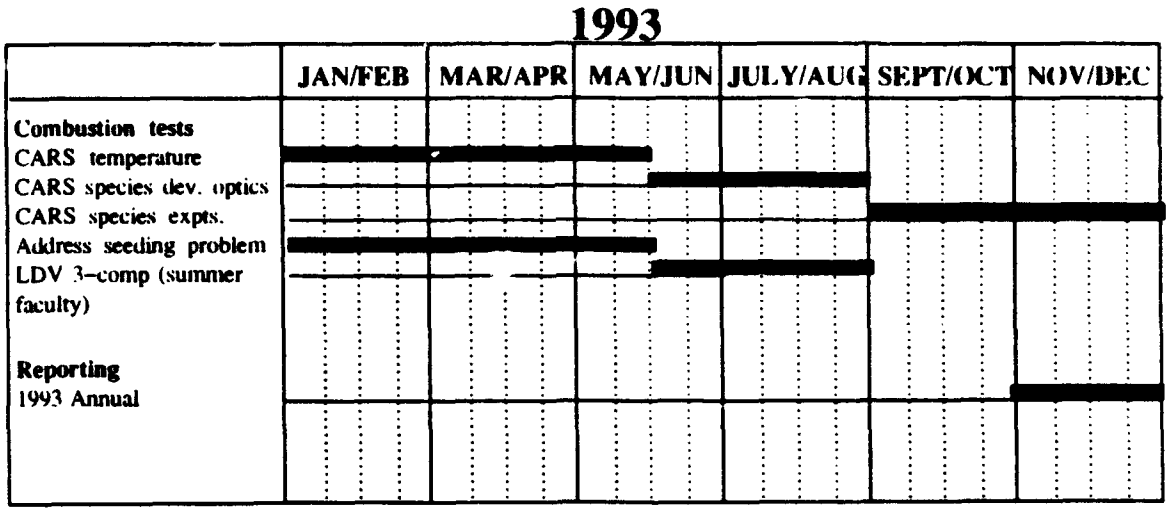

Figure 47: Anticipated Schedule — 1993

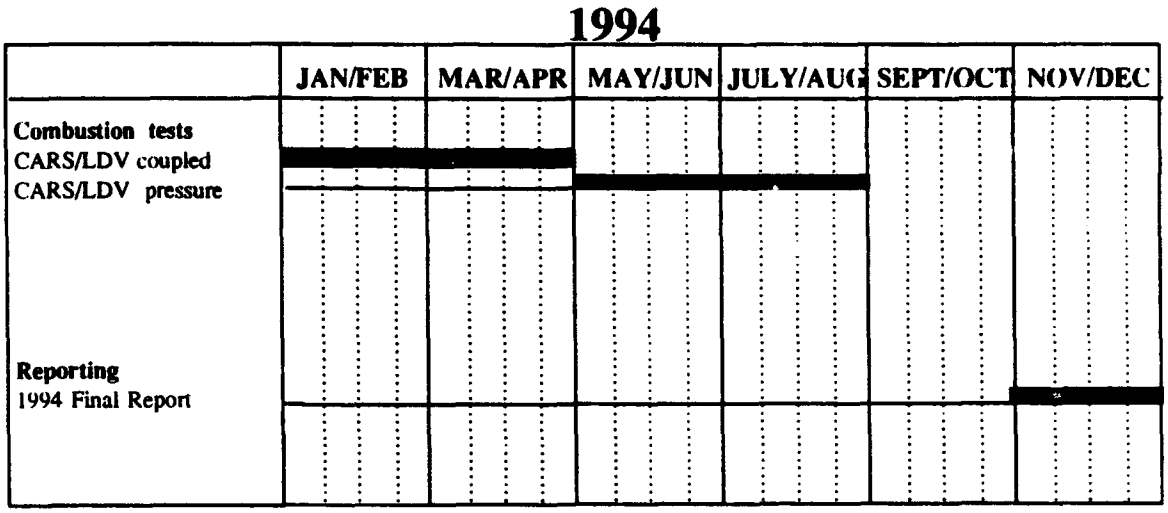

Figure 48: Anticipated Schedule — 1994

8 Conclusions

Much effort has been expended in gathering the isothermal CFD data. Mass flow anomalies were identified when comparisons were made between the flowmeter measurements and integrated axial velocity profiles. These were attributed to LDV signal noise caused by reflections of the LDV probe volume off the internal combustor wall. These noise problems were minimized when LDV measurements were made along the vertical diameter of the circular cross-section combustor, thus ensuring that the reflections were transmitted off the LDV optical axis. This knowledge has been put into effect in the design of the new hot test section and demonstrates the useful approach of first taking isothermal measurements as a means of testing out instrumentation.

The axial gradients in velocity and stresses were found to be very steep within the first $150mm$ downstream from the swirler. Consequently, it is recommended that more axial data stations should be included in future work. An additional 20 locations are suggested, resulting in a resolution of $5mm$ axially and $2.5mm$ radially within $150mm$ of combustor length.

Initial CFD modeling has provided good results. The RSTM has demonstrated its superiority over the $k-\epsilon$ model for strongly swirling, confined flows such as the one investigated in this work. Mean velocity field predictions were good but the models for the Reynolds stresses will require further development. The importance of the $\overline{v'w'}$ shear stress was clearly illustrated to affect the character of the swirling flow. It was the only shear stress that could not be measured with the Plexiglas combustor and the two-component LDV system.

During initial combustion trials, some flow instabilities were identified. These were found to be caused by the upstream swirl air supply ductwork and were augmented at higher equivalence ratios. It was agreed that the effort required in changing the ductwork was prohibitive and, therefore, the running conditions were changed from an equivalence ratio of 0.6 to 0.45, at which, no instabilities were observed.

The optical access provided by the water-cooled combustor in the WL facility was quite restricted in relation to obtaining a full data set that could usefully be employed in combustion CFD code validation. Thus, in light of what was learned in the isothermal phase of the program, a new test section was designed, built and installed. This section permits the access of a 3-component LDV system for the simultaneous measurement of all velocity components and Reynolds stresses at pressures of up to $3atm.$ as well as the simultaneous application of CARS for temperature and species measurements.

Excluding vacation and holidays, over 7.5 months of the 32-month program have experienced rig downtime. This includes time used on the rig by summer faculty staff who were carrying out research unrelated to the WL/RR program. These delays have now been reduced by agreeing to a summer schedule that benefits both

the faculty staff and the WL/RR program.

At the outset of this program there was no means of nonintrusively measuring the temperatures on the WL facility, and in response to this, WL built up a CARS system. This is now complete and with recent installation of the new Rolls-Royce designed hot test section, the combustion diagnostics facility at WL has been brought up to a world class capability for studying gas turbine combusting flow fields. The next phase of this research program will be to embark on combustion diagnostics and modeling.

References

[1] Wilhelmi, J., "Axisymmetric Swirl Stabilized Combustion," PhD Thesis, Imperial College London ENGLAND, June 1984.

[2] Ahmed, S.A. and Nejad, A.S., "Premixed Turbulent Combustion of Axisymmetric Sudden Expansion Flows," *International Journal of Heat and Fluid Flow*, Vol. 12, No. 1, March 1992.

[3] Nejad, A.S., Vanka, S.P., Favaloro, S.C., Sammimy, M., and Langenfeld, C., "Application of Laser Velocimetry for Characterization of Confined Swirling Flow," Journal of Engineering for Gas Turbines and Power, Vol. 111, pp. 36-45, 1984.

[4] Buckley P. L., Craig, R. R., Davis, D. L. and Schwartzkopf, K. G., "The Design and Combustion Performance of Practical Swirlers for Integral Rockets/Ramjets," *AIAA Journal*, Vol. 21, No. 5, May 1983.

[5] Beér, J.M. and Chigier, N.A., *Combustion Aerodynamics*, Applied Science, pp100-146, 1972.

[6] Craig, R.R., Nejad, A.S., Hahn, E.Y., and Schwartzkopf, K.G., "A General Approach for Obtaining Unbiased LDV Data in Highly Turbulent Non-reacting and Reacting Flows," AIAA Paper No. 84-0366, 1984.

[7] Nejad, A.S., Vanka, S.P., Favaloro, S.C., Sammimy, M., and Langenfeld, C., "Application of Laser Velocimetry for Characterization of Confined Swirling Flow," Journal of Engineering for Gas Turbines and Power, Vol. 111, pp. 36-45, 1984.

[8] Ahmed, S.A., Nejad, A.S., and Craig, R.R., "A Near Field Study of a Turbulent Free Jet, Including the Effects of Velocity Bias," Eleventh symposium on Turbulence, University of Missouri-Rolla, 1988.

[9] Snyder, P. K., Orloff, K. L., and Reinath, M. S., "Reduction of Flow Measurement Uncertainties in Laser Velocimeters With Nonorthogonal Channels," AIAA Journal, Vol. 22, No. 8, pp. 1115-1123, 1984.

[10] Favre A., "Problems of Hydrodynamics and Continuous Mechanics," *Society for Industrial and Applied Mathematics*, p231, 1969.

[11] Hogg, S. I., "Second-Moment-Closure Calculations of Strongly-Swirling Confined Flows with and without Density Variations," PhD Thesis, University of Manchester, ENGLAND, December 1988.

[12] Manners, A. P., "The Calculation of the Flows in Gas Turbine Combustor Systems," PhD Thesis, Imperial College London, ENGLAND, June 1988.

[13] Beinito, A. P., "The Application of Second Order Turbulence Closures to Isothermal and Combusting Swirling Flows," PhD Thesis, Imperial College London, ENGLAND, October 1989.

[14] Boussinesq, J., "Essai sur la theorie des eaux courantes," Memoire presente par divers savants a l'Academie des Sciences, Vol. 23, No. 1, pp 1-680, Paris, 1877.

[15] Boussinesq, J., "Theorie de l'ecoulement tourbillonnant et tumulteux des liquides dans les lits rectilignes a grande section," I-II Gauthier-Villars, Paris, 1897.

[16] Launder, B. E. and Spalding, D. B., "The Numerical Computation of Turbulent Flows," *Comp. Meth. in Applied Mech. and Eng.*, Vol. 3, No. 2, pp 269-289, 1974.

[17] Jones, W.P., "Models for Turbulent Flows with Variable Density and Combustion," *Prediction Methods for Turbulent Flows*, Ed. W. Kollman, Hemisphere 1980.

[18] Gibson, M.M. and Launder B.E., "Ground Effects on Pressure Fluctuations in the Atmospheric Boundary Layer," *Journal of Fluid Mechanics* Vol. 86, pp. 491-511, 1978.

[19] Launder, B.E, Reece, G.J. and Rodi, W., "Progress in the Development of a Reynolds Stress Closure," *Journal of Fluid Mechanics*, Vol68, pp. 537-566, 1975.

[20] Chou, P.Y., "On velocity Correlations and the Solutions of the Equations of Turbulent Fluctuations," *Quarterly Applied Mathematics*, Vol. 3, p. 38, 1945.

[21] Hanjalic, K. and Launder, B.E, "A Reynolds Stress Model of Turbulence and its Applications to Thin Shear Flows," *Journal of Fluid Mechanics*, Vol. 52, p. 609, 1972.

[22] Daly, B.J. and Harlow, F.H., "Transport Equations in Turbulence," *Physics of Fluids* Vol. 13, p. 2634, 1970.

[23] Shir, C.C., "A preliminary Numerical Study of Atmospheric Turbulent Flows in the Idealized Planetary Boundary Layer," *Journal of Atmospheric Science*, Vol. 30, pp 1327-1329, 1973.

[24] Rotta, J.C, "Statistische Theorie Nichthomogener Turbulenz," *Zeitschrift für Physik*, Vol. 129, No. 5, pp 547-572, 1951.

[25] Naot, D., Shavit, A. and Wolfshtein, M., "Interaction between Components of the Turbulent Velocity Correlation Tensor due to Pressure Fluctuations," *Israel Journal of Technology*, Vol. 8, p. 259, 1970.

[26] Hinze, J. O., "Turbulence," McGraw Hill, 1959.

[27] Monin, A.S., "On the Symmetry properties of Turbulence in the Surface Layer of Air," *IZM Atmospheric and Oceanic Physics I*, Vol. 45, pp. 45–54, 1965.

[28] Gould, R. D. and Benedict, L. H., "Velocity and Temperature Measurements in a High Swirl Dump Combustor," *Final Report, Summer Research Program, Wright Laboratory*, Sponsored by AFOSR, August 1992.

[29] Personal Communication with Dr. Larry Goss of Scientific Research Laboratories (SRL), Dayton Ohio, November 1992.

[30] So, R.M., Ahmed, S.A. and Mongia, H.C., "An Experimental Investigation of Gas Jets in Confined Swirling Air Flow," *NASA CR 3832*, 1984.

[31] Squire, H.B., "Analysis of the Vortex Breakdown Phenomenon," *Miszellanen der Angerwandten Mechanik, Akademie, Berlin*, pp306-312, 1962.

[32] Abujelala, M.T. and Lilley, D.G., "Confined Swirling Flow Predictions," *AIAA-83-0316*, January 1983.

[33] Sturgess, G.J., Syed, S.A. and McManus, K.R., "Importance of Inlet Boundary Conditions for Numerical Simulation of Combustor Flows," *AIAA-83-1263*, June 1983.

[34] Gupta, A.K., Lilley, D.G. and Syed, N., "Swirl Flows," Abacus Press, 1984.

[35] Spalding, D.B., "A Novel Finite Difference Formulation for Differential Equations Involving both First and Second Derivatives," *International Journal of Numerical Methods in Engineeering*, Vol. 4, pp551-559, 1972.

[36] Veninger, A., "Statement of Work — Collaborative Research on Combustion Diagnostics and Modeling between Rolls–Royce Inc., and the Air Force Wright Research Development Center." *AV90–81, Rolls–Royce Inc. Atlanta.*

APPENDIX A

Conventially Averaged Equations for Constant Density Flows

Continuity;

$$\frac{\partial}{\partial x}\rho\overline{U} + \frac{1}{r}\frac{\partial}{\partial r}\rho r\overline{V} = 0 \tag{66}$$

momentum;

$$\frac{\partial}{\partial x}\rho r\overline{U}\,\overline{U} + \frac{\partial}{\partial r}\rho r\overline{V}\,\overline{U} = \frac{\partial}{\partial x}\left(r\mu\frac{\partial\overline{U}}{\partial x}\right) + \frac{\partial}{\partial r}\left(r\mu\frac{\partial\overline{U}}{\partial r}\right) - r\frac{\partial p}{\partial x} - \frac{\partial}{\partial x}\rho r\overline{u'^2} - \frac{\partial}{\partial r}\rho r\overline{u'v'} \tag{67}$$

$$\frac{\partial}{\partial x}\rho r\overline{U}\,\overline{V} + \frac{\partial}{\partial r}\rho r\overline{V}\,\overline{V} = \frac{\partial}{\partial x}\left(r\mu\frac{\partial\overline{V}}{\partial x}\right) + \frac{\partial}{\partial r}\left(r\mu\frac{\partial\overline{V}}{\partial r}\right) - r\frac{\partial p}{\partial r} - \frac{\partial}{\partial r}\rho r\overline{v'^2} - \frac{\partial}{\partial x}\rho r\overline{u'v'} + \rho\overline{W}^2 + \rho\overline{w'^2} - \frac{\mu\overline{V}}{r} \tag{68}$$

$$\frac{\partial}{\partial x}\rho r\overline{U}\,\overline{rW} + \frac{\partial}{\partial r}\rho r\overline{V}\,\overline{rW} = \frac{\partial}{\partial x}\left(r\mu\frac{\partial\overline{rW}}{\partial x}\right) + \frac{\partial}{\partial r}\left(r\mu\frac{\partial\overline{rW}}{\partial r}\right) - r^2\frac{\partial}{\partial x}\rho\overline{u'w'} - r^2\frac{\partial}{\partial r}\rho\overline{v'w'} - 2r\rho\overline{v'w'} - 2\mu\frac{\partial}{\partial r}\overline{rW} \tag{69}$$

scalar field;

$$\frac{\partial}{\partial x}\rho r\overline{U}\,\overline{C} + \frac{\partial}{\partial r}\rho r\overline{V}\,\overline{C} = \frac{\partial}{\partial x}\left(r\frac{\mu}{\sigma_c}\frac{\partial\overline{C}}{\partial x}\right) + \frac{\partial}{\partial r}\left(r\frac{\mu}{\sigma_c}\frac{\partial\overline{C}}{\partial r}\right) - \frac{\partial}{\partial x}\rho r\overline{u'c'} - \frac{\partial}{\partial r}\rho r\overline{v'c'} + r\overline{S_c} \tag{70}$$

APPENDIX B

Isothermal CFD Predictions - Complete Results

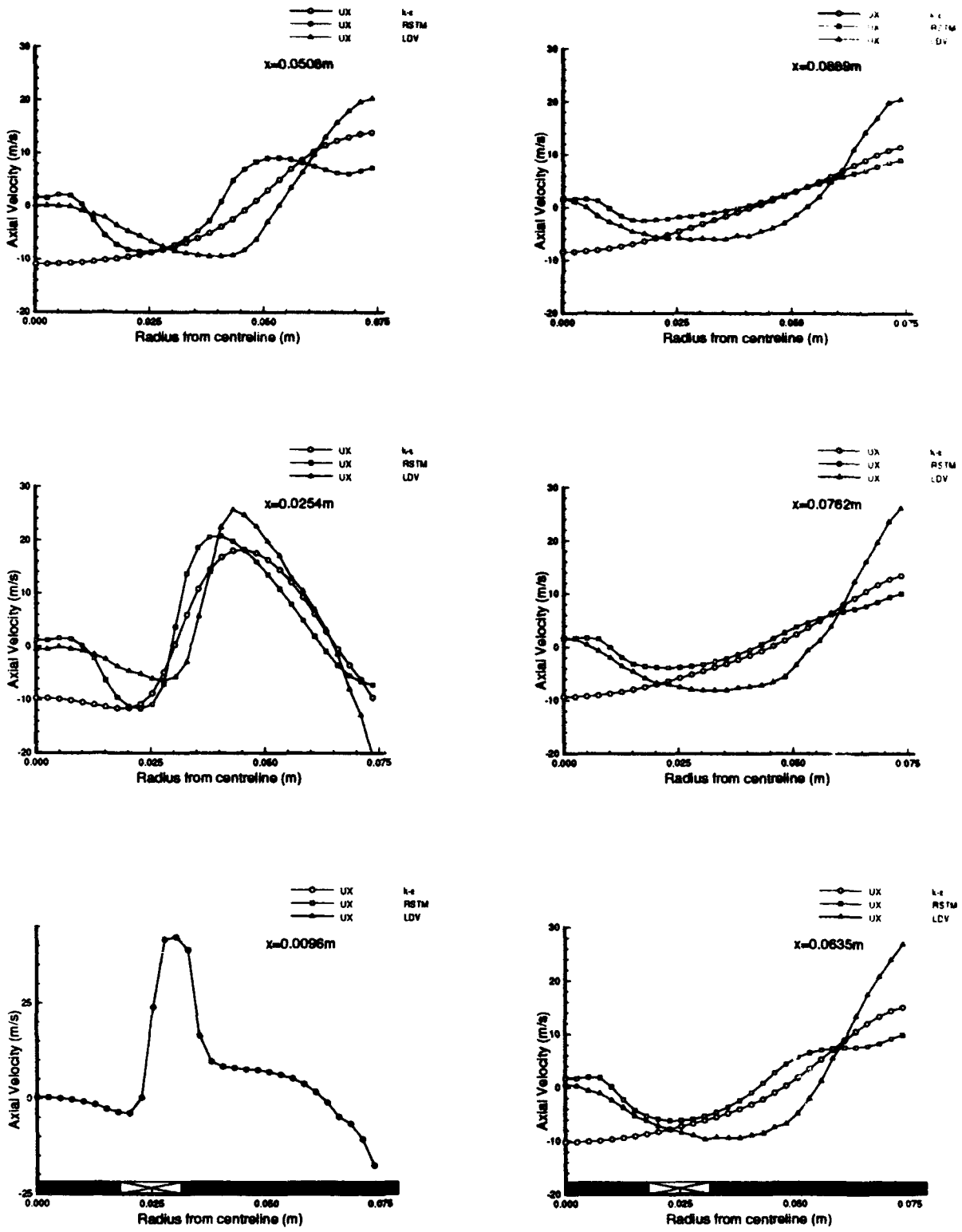

Figure 49a Measured vs. Predicted – Axial Velocity Profiles

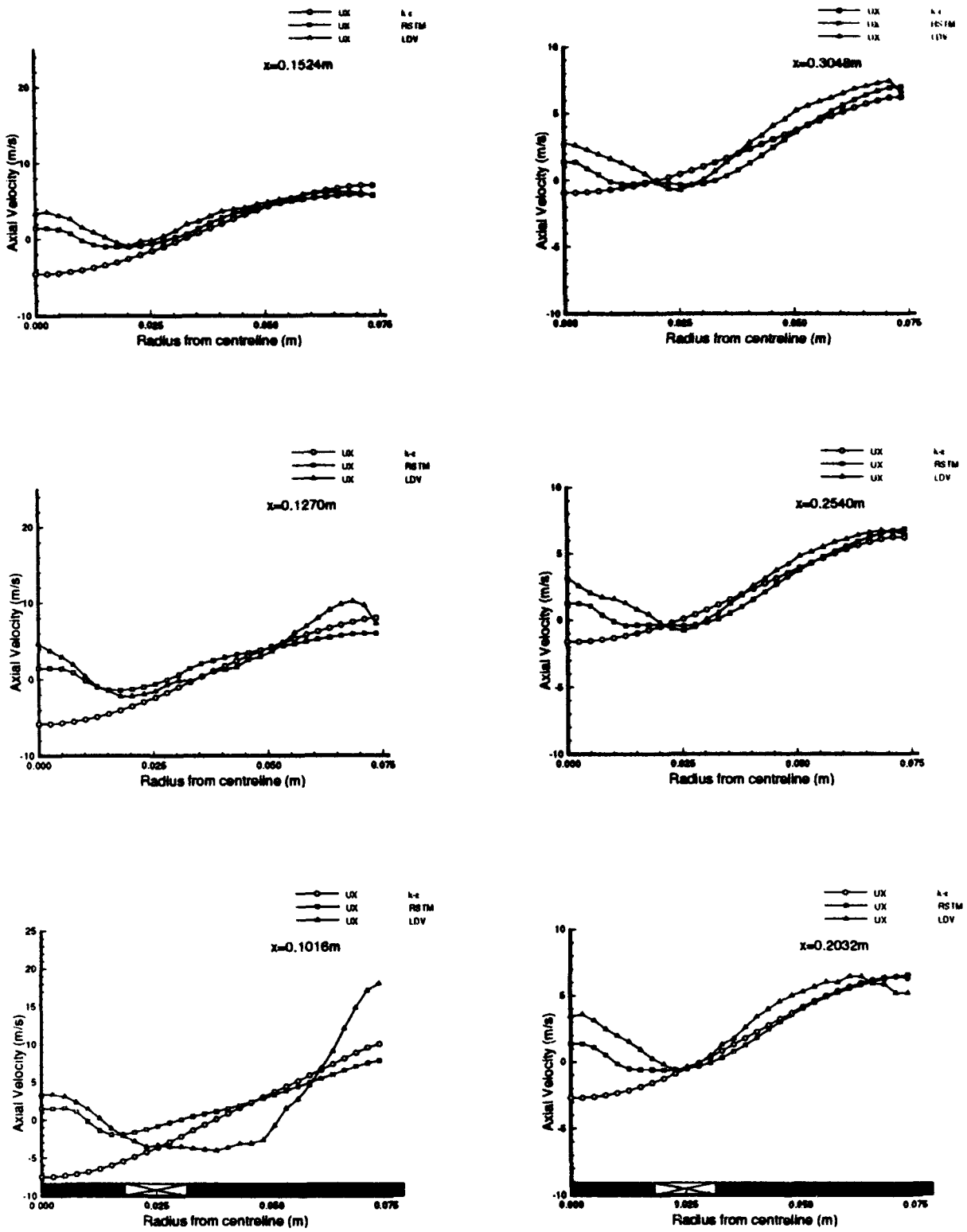

Figure 49b Measured vs. Predicted – Axial Velocity Profiles

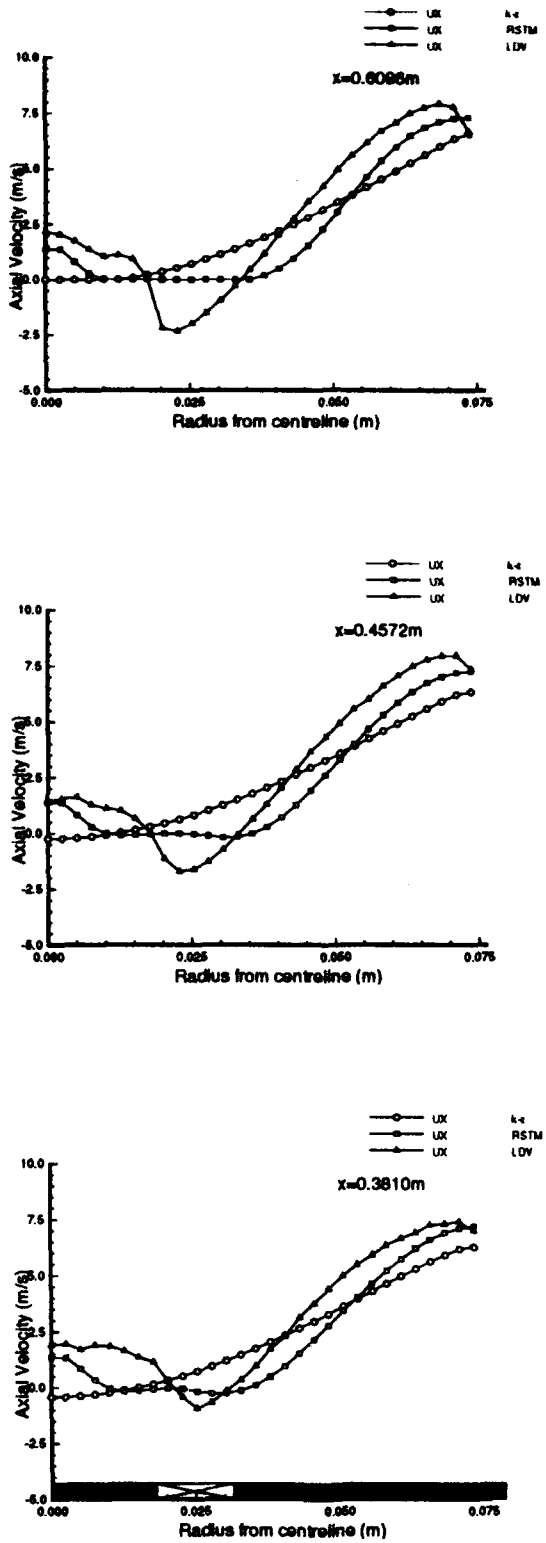

Figure 49c Measured vs. Predicted – Axial Velocity Profiles

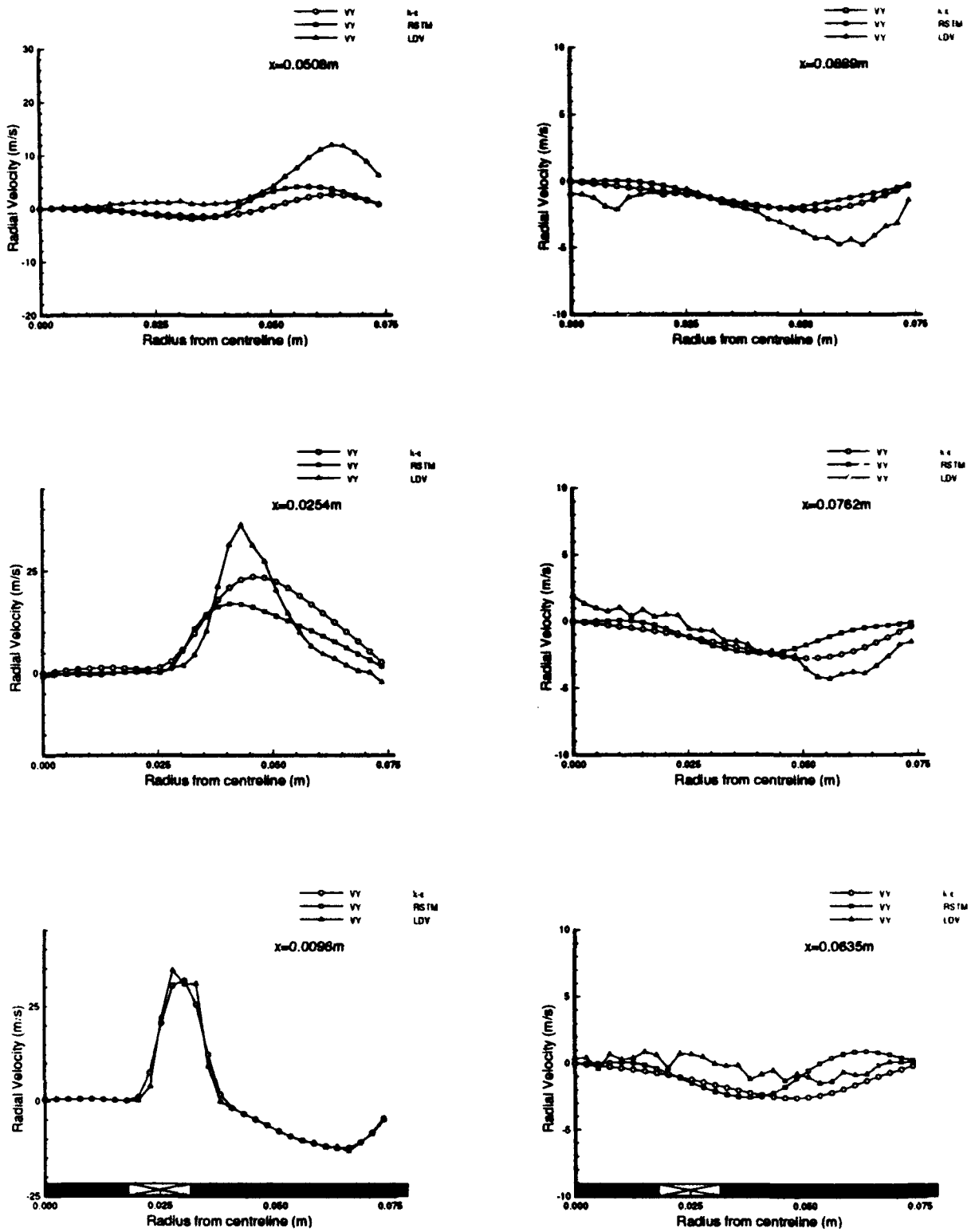

Figure 50a Measured vs. Predicted – Radial Velocity Profiles

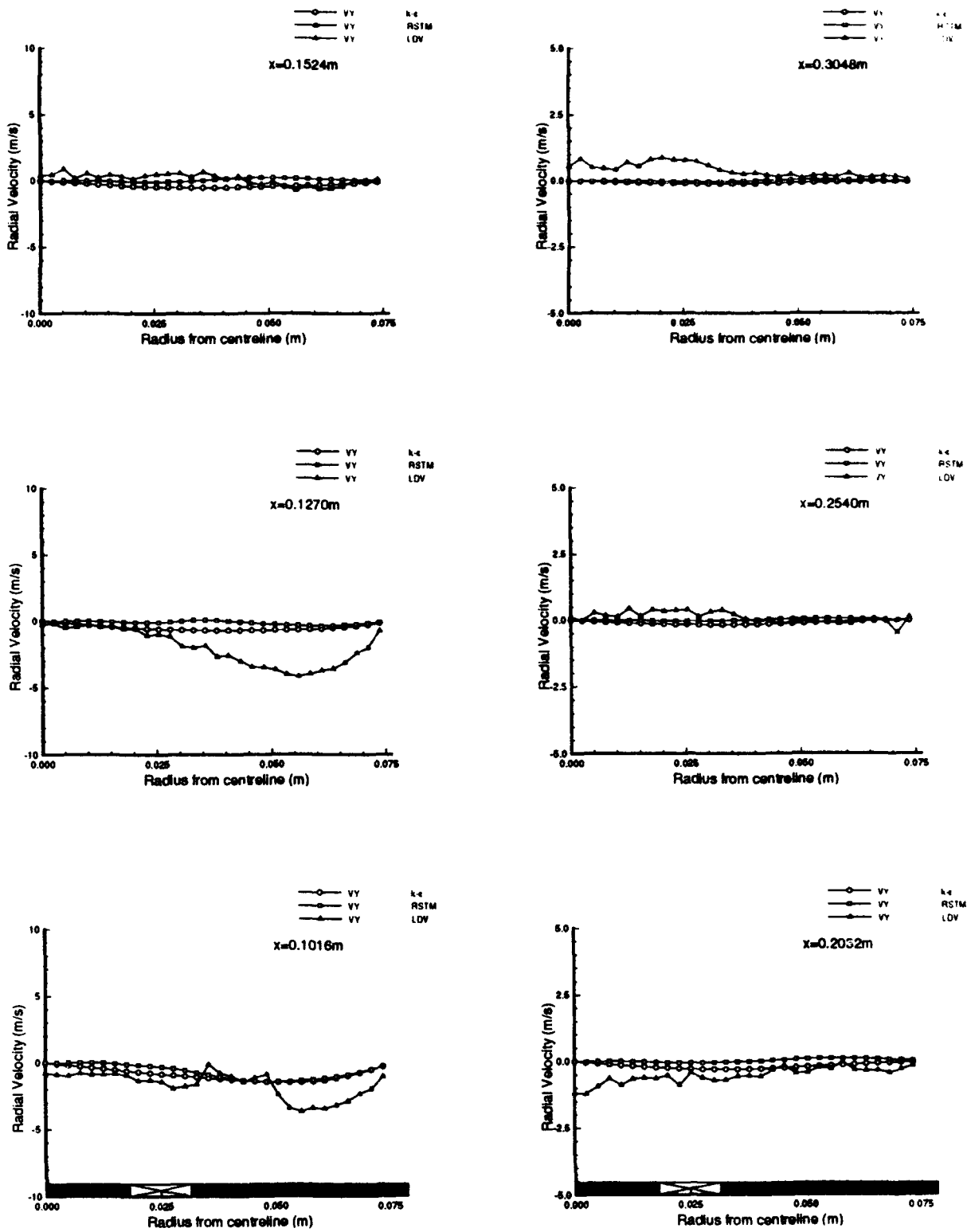

Figure 50b Measured vs. Predicted – Radial Velocity Profiles

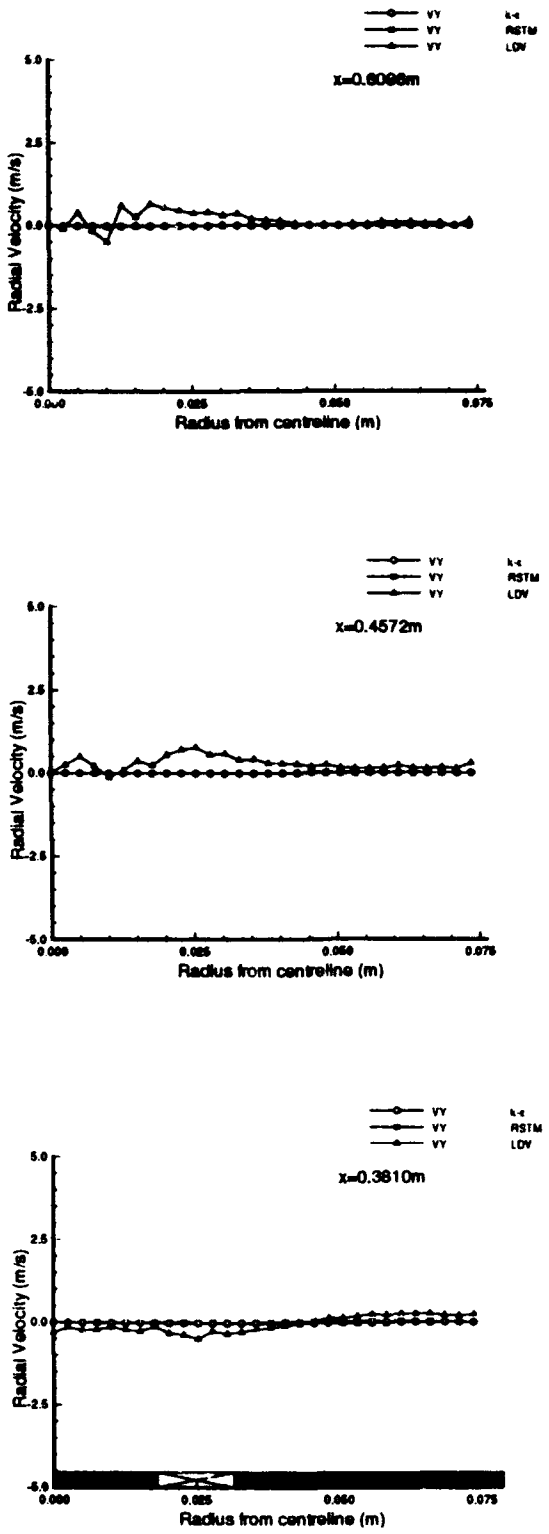

Figure 50c Measured vs. Predicted – Radial Velocity Profiles

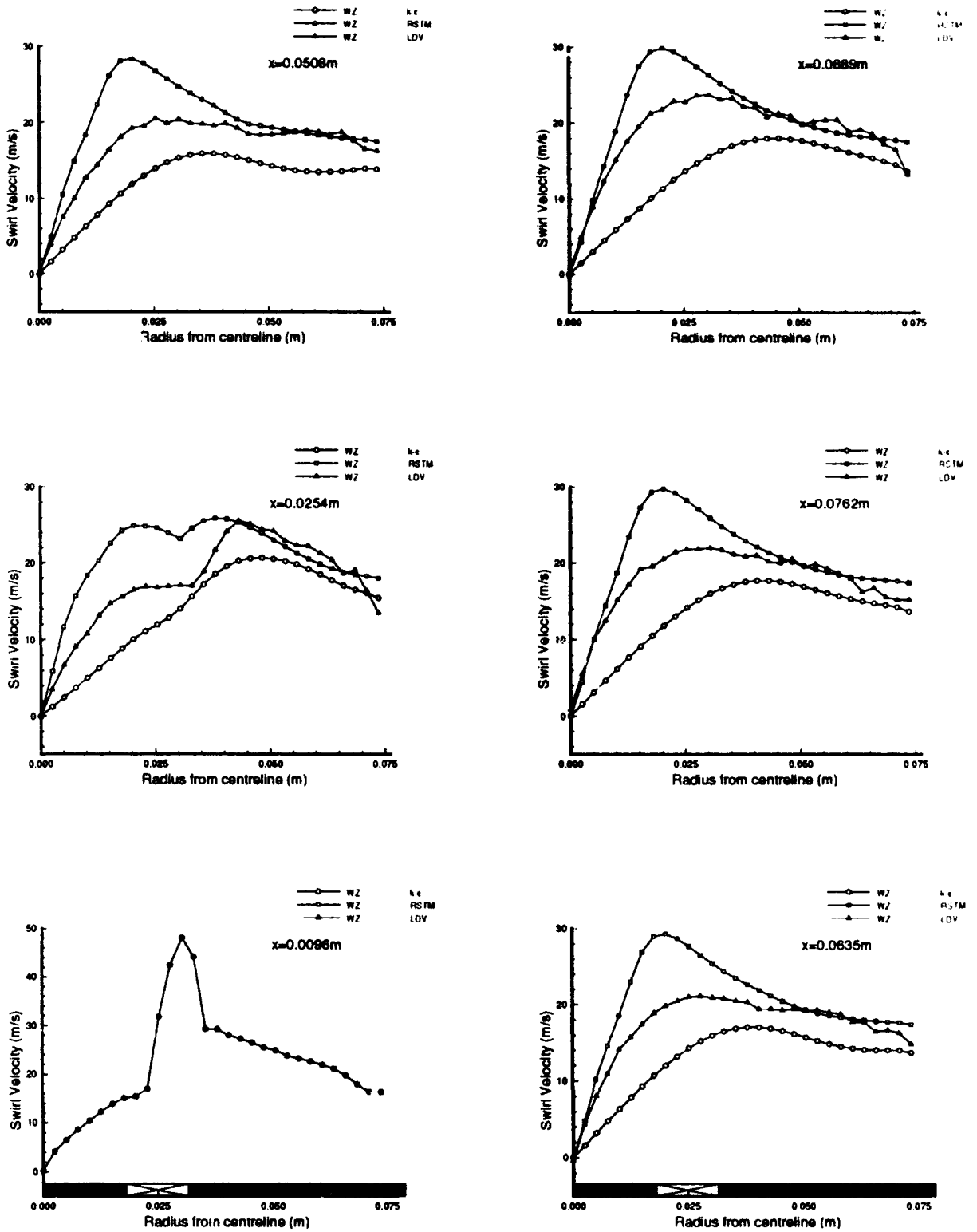

Figure 51a Measured vs. Predicted – Swirl Velocity Profiles

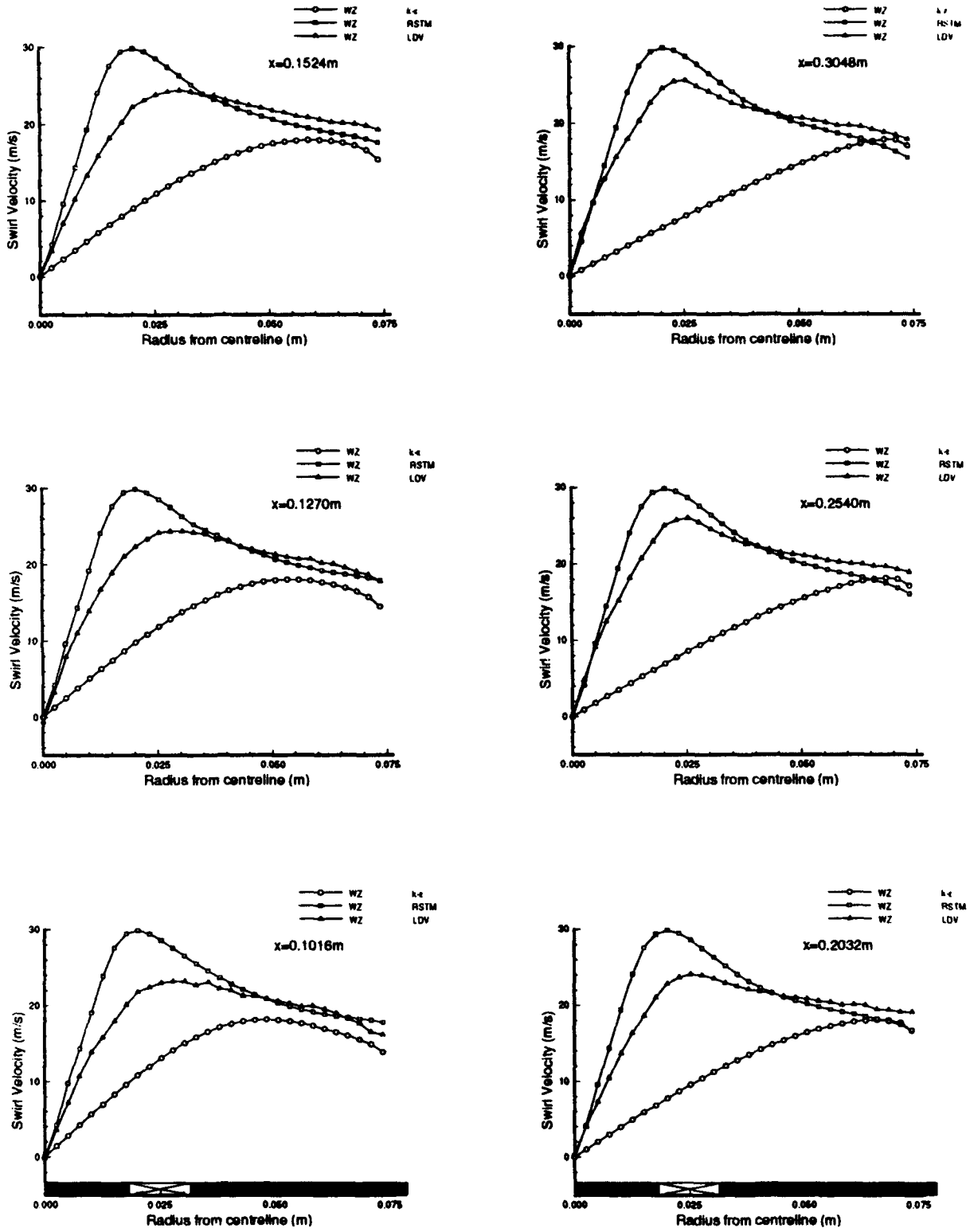

Figure 51b Measured vs. Predicted – Swirl Velocity Profiles

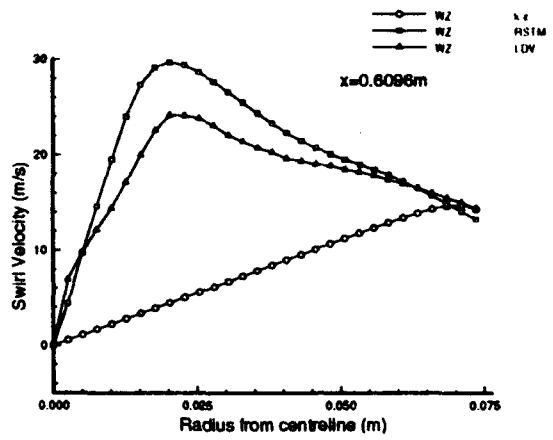

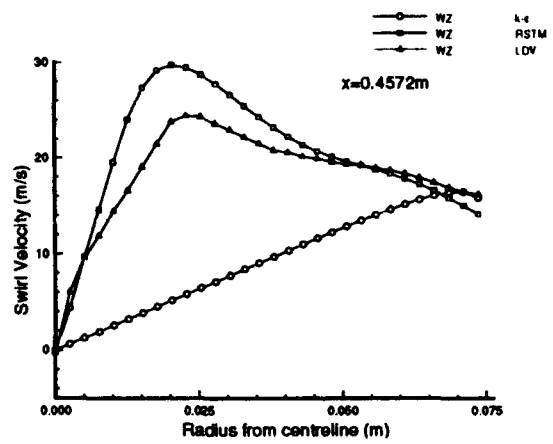

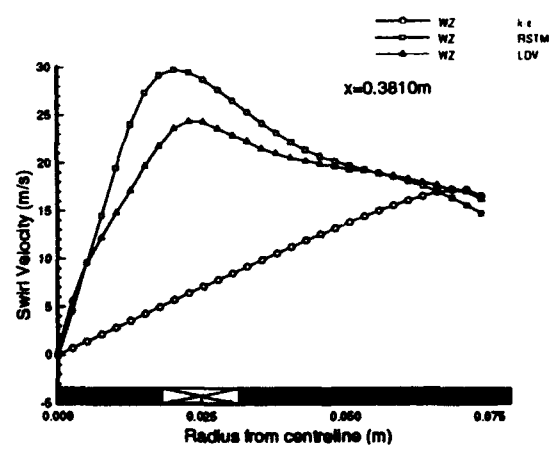

Figure 51c Measured vs. Predicted – Swirl Velocity Profiles

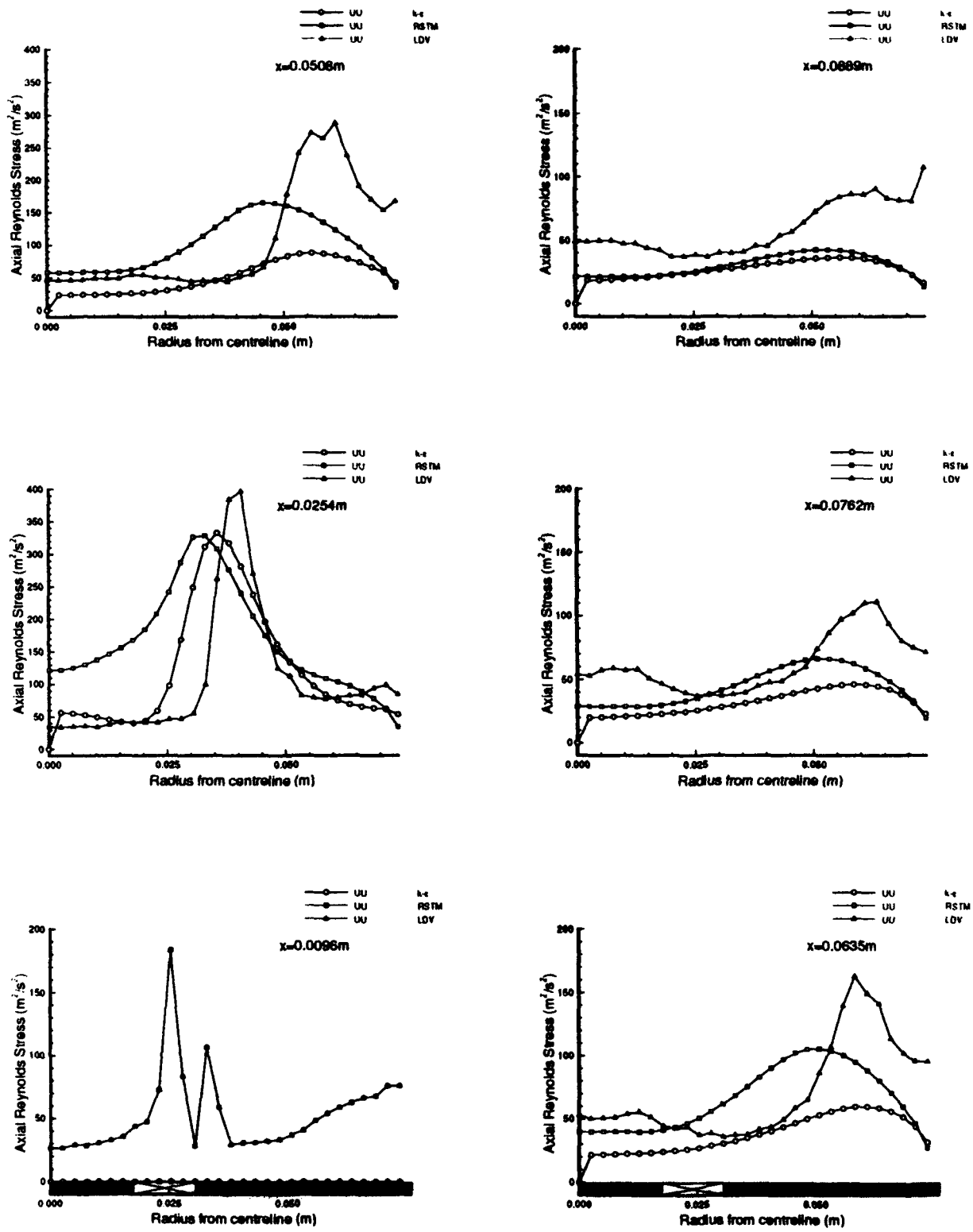

Figure 52a Measured vs. Predicted – Axial Reynolds Stress Profiles

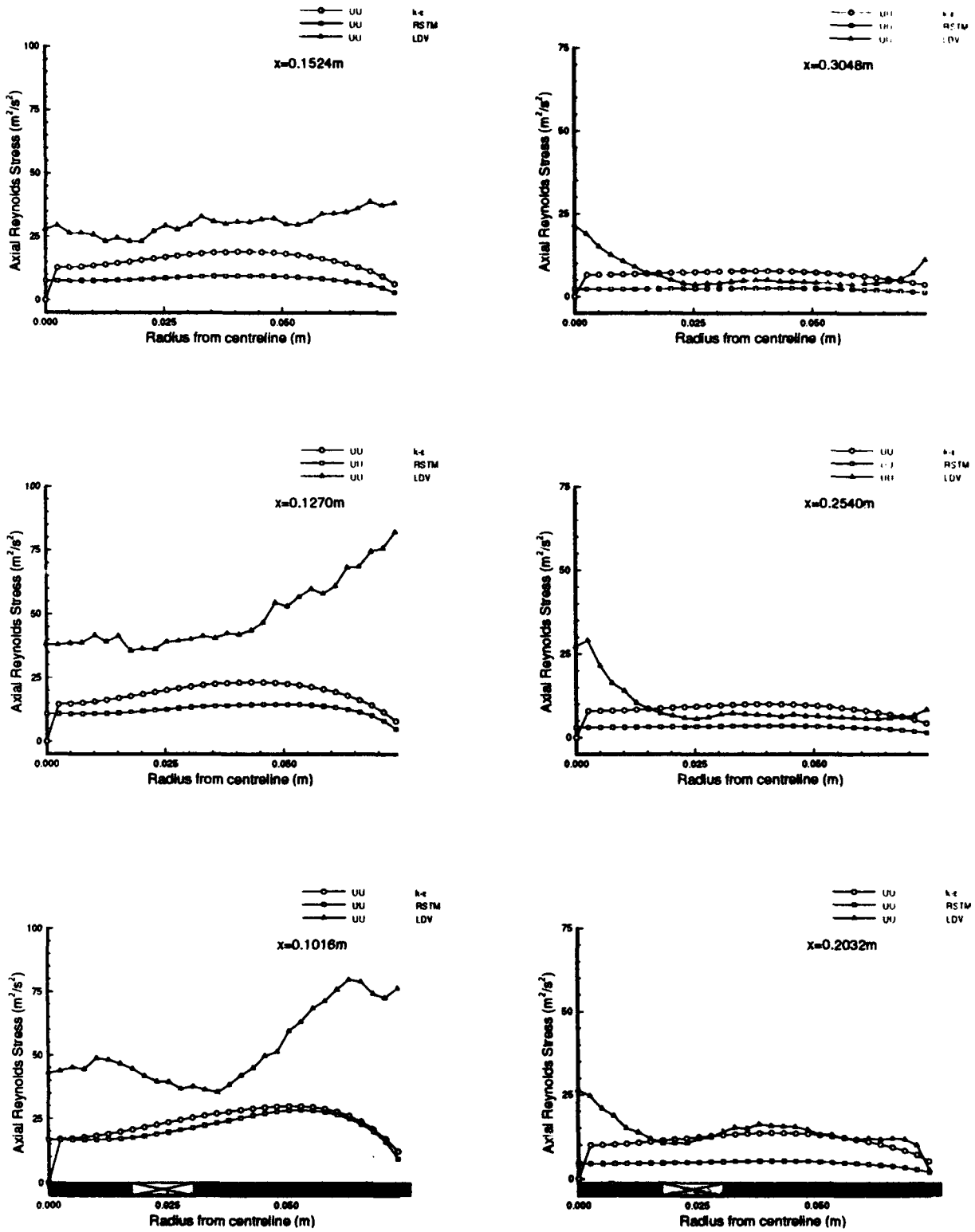

Figure 52b Measured vs. Predicted – Axial Reynolds Stress Profiles

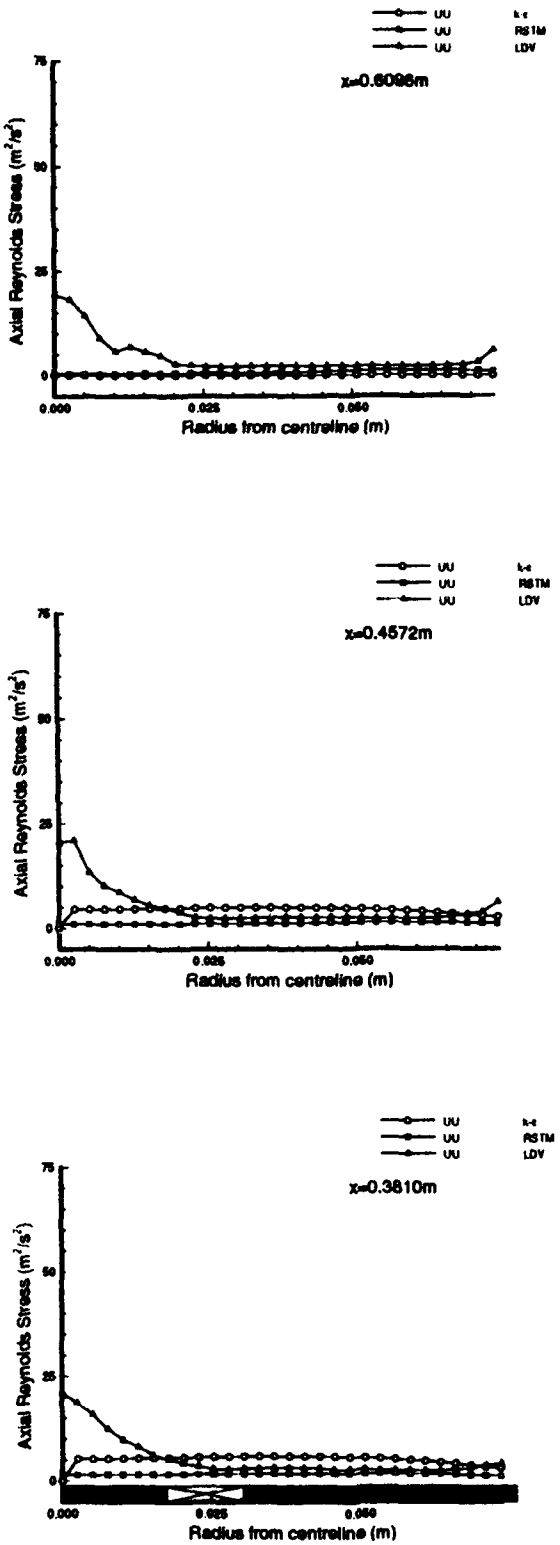

Figure 52c Measured vs. Predicted – Axial Reynolds Stress Profiles

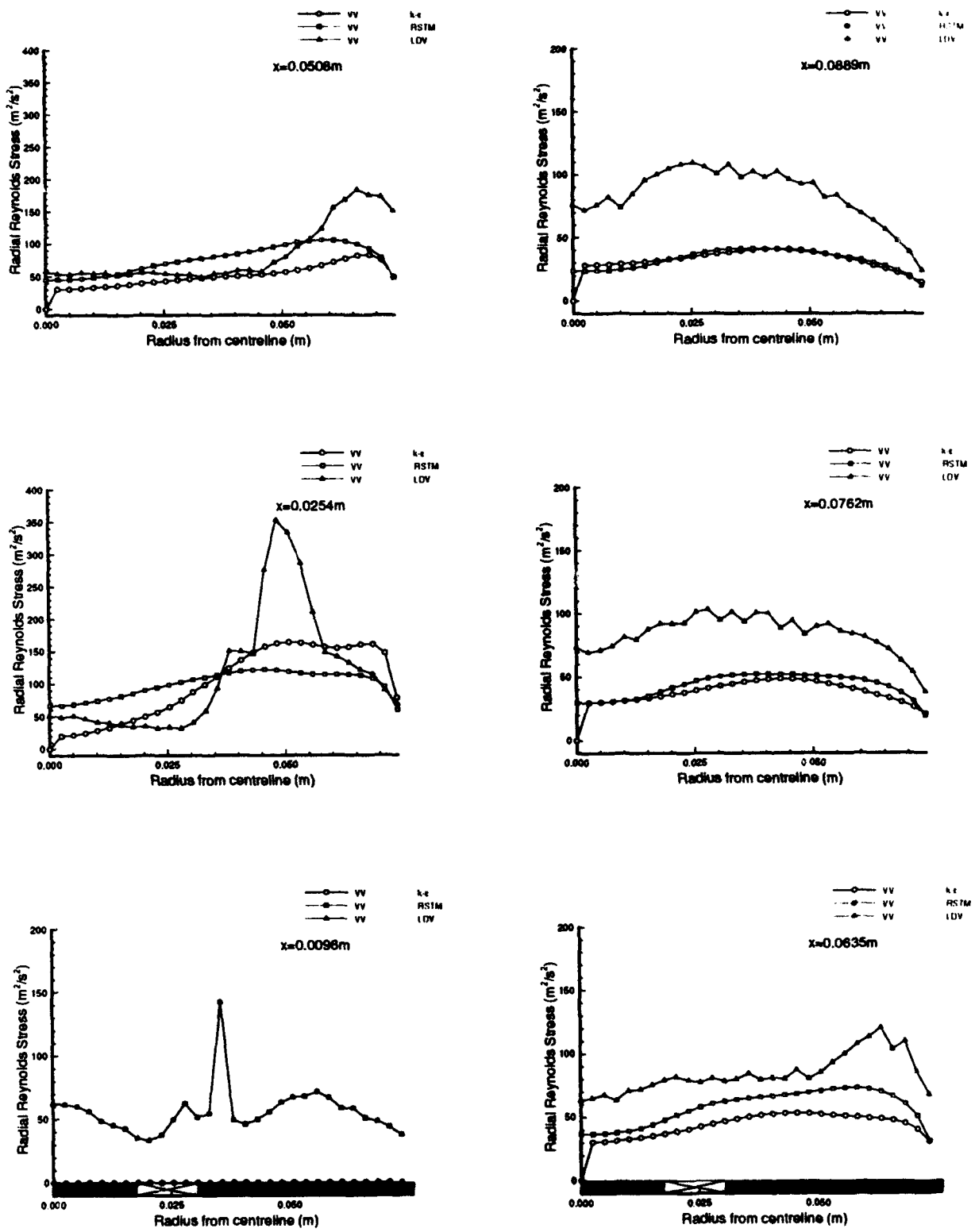

Figure 53a Measured vs. Predicted – Radial Reynolds Stress Profiles

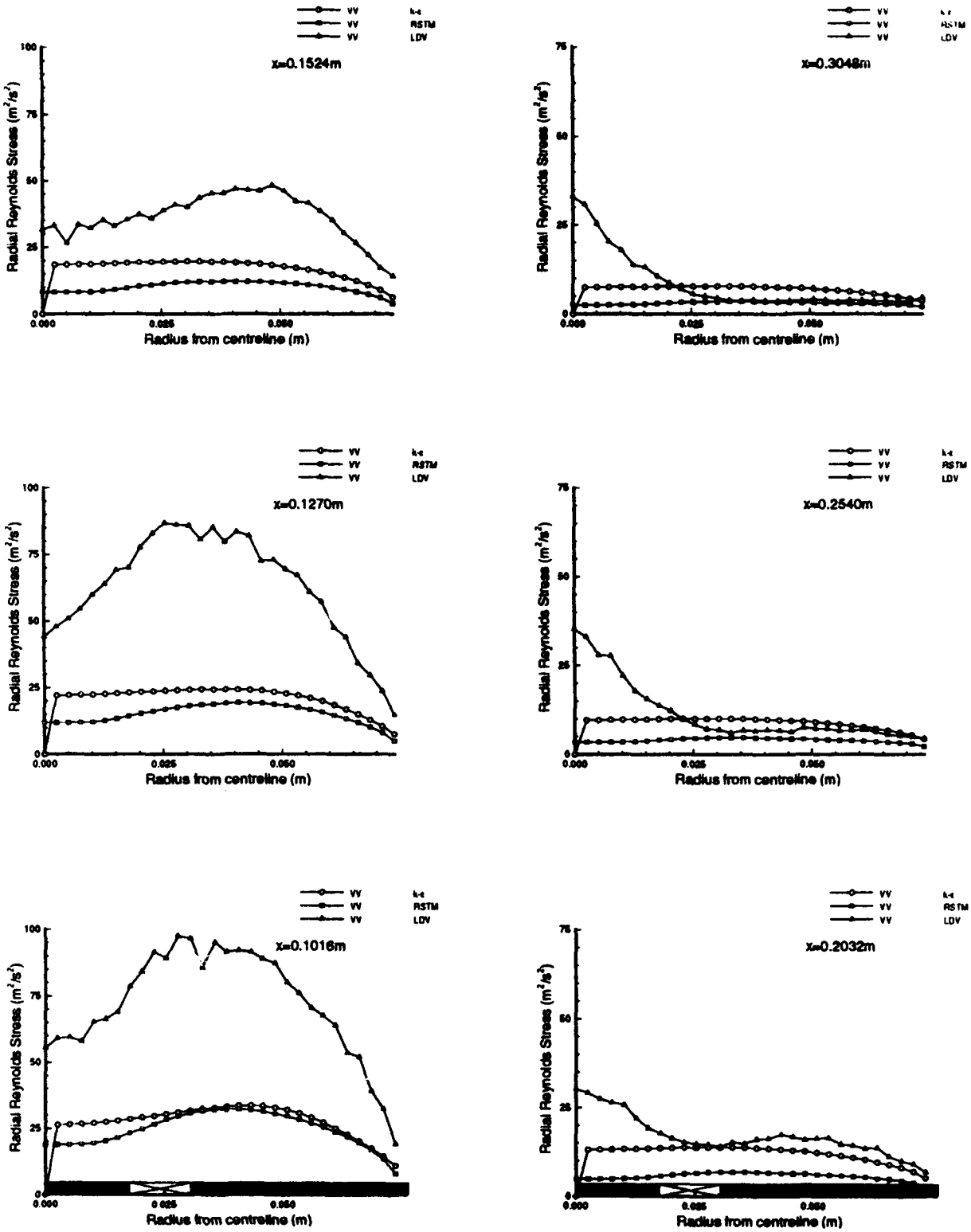

Figure 53b Measured vs. Predicted – Radial Reynolds Stress Profiles

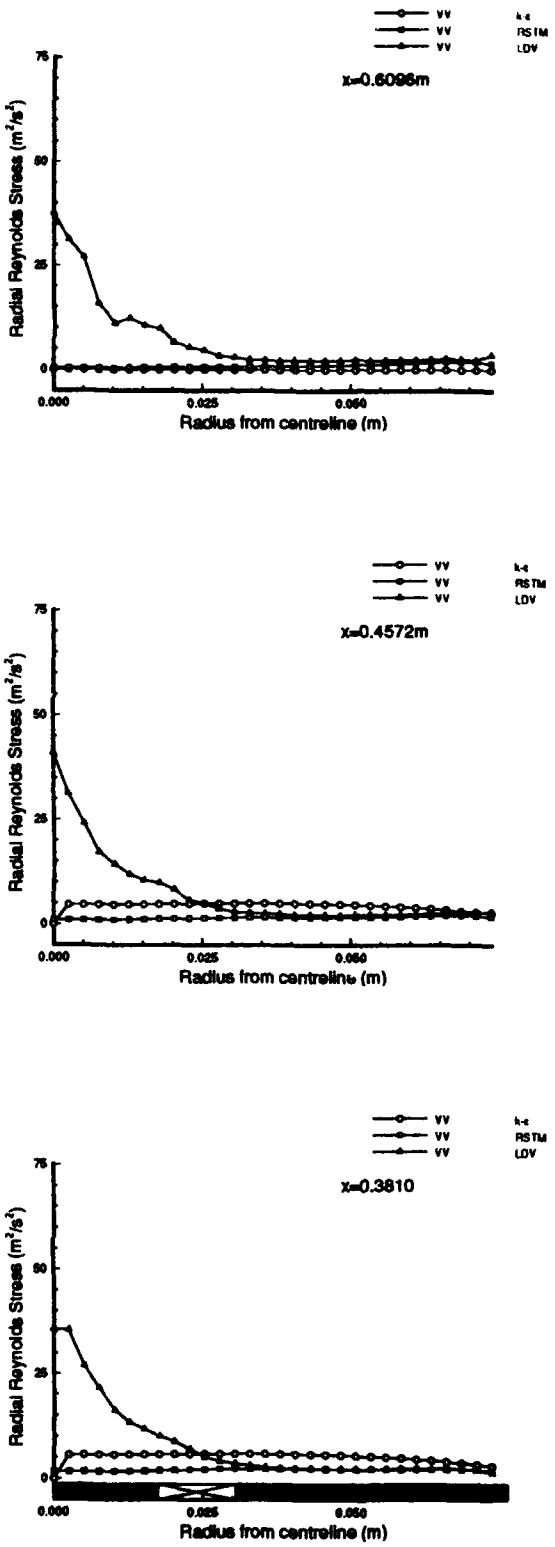

Figure 53c Measured vs. Predicted – Radial Reynolds Stress Profiles

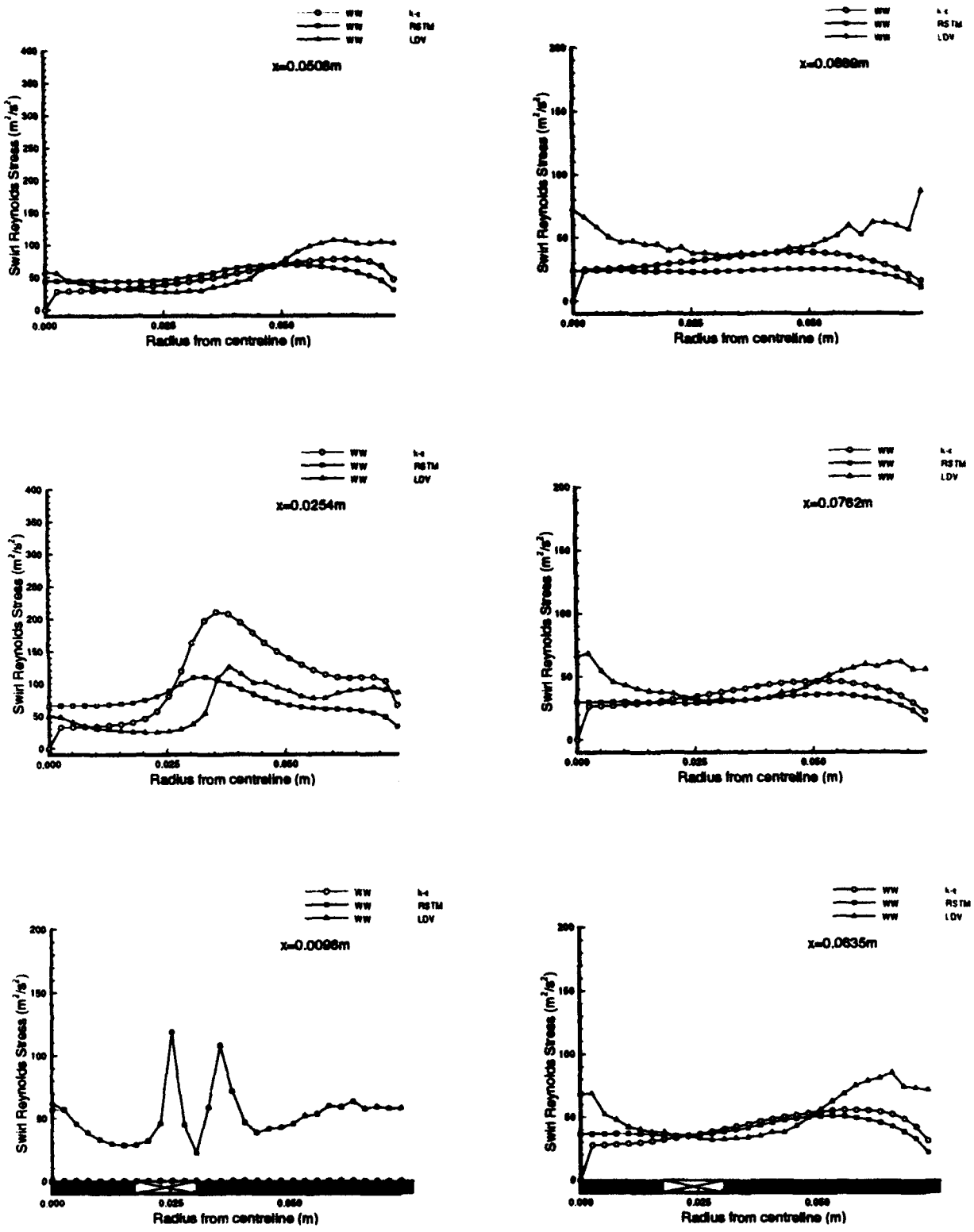

Figure 54a Measured vs. Predicted – Swirl Reynolds Stress Profiles

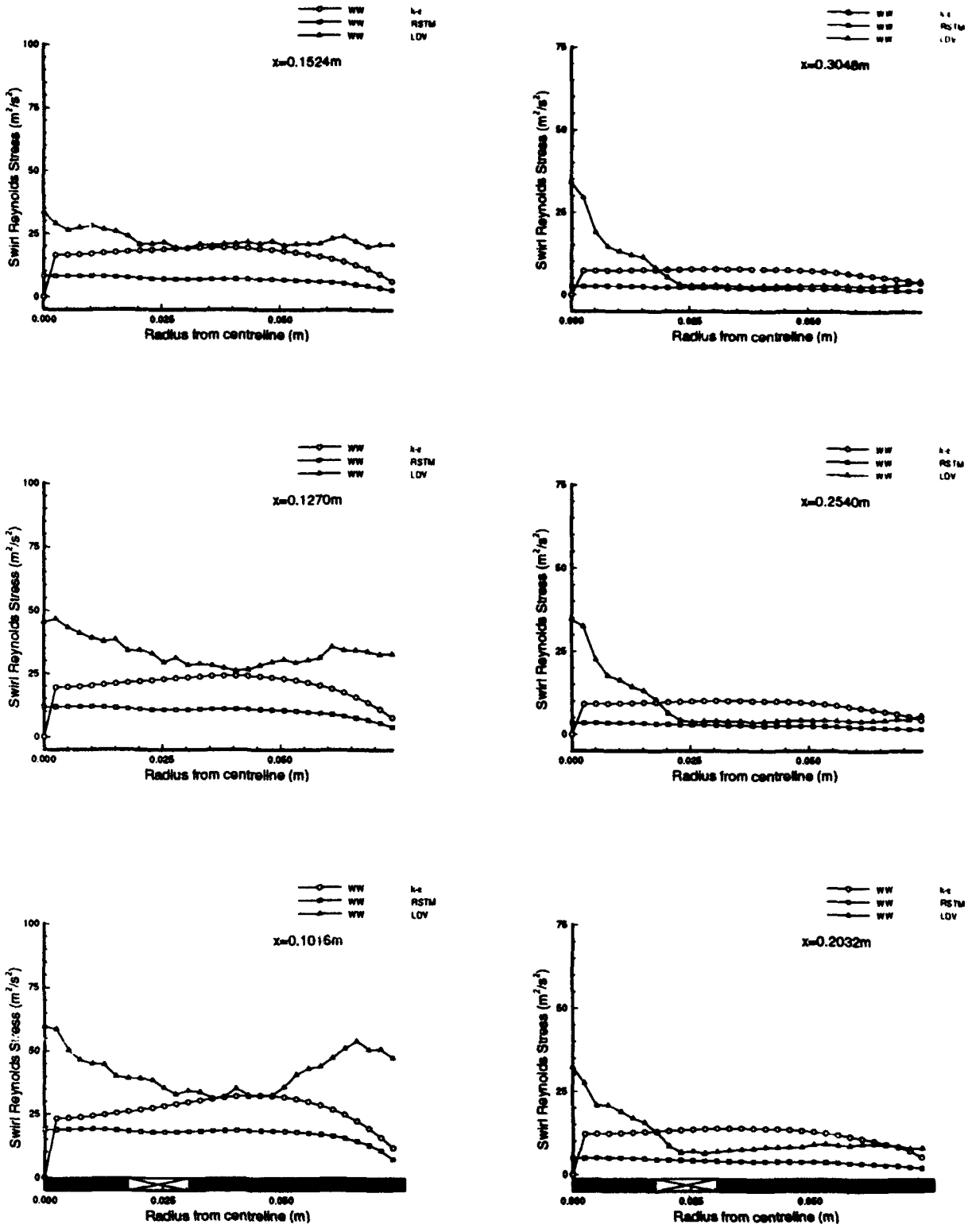

Figure 54b Measured vs. Predicted – Swirl Reynolds Stress Profiles

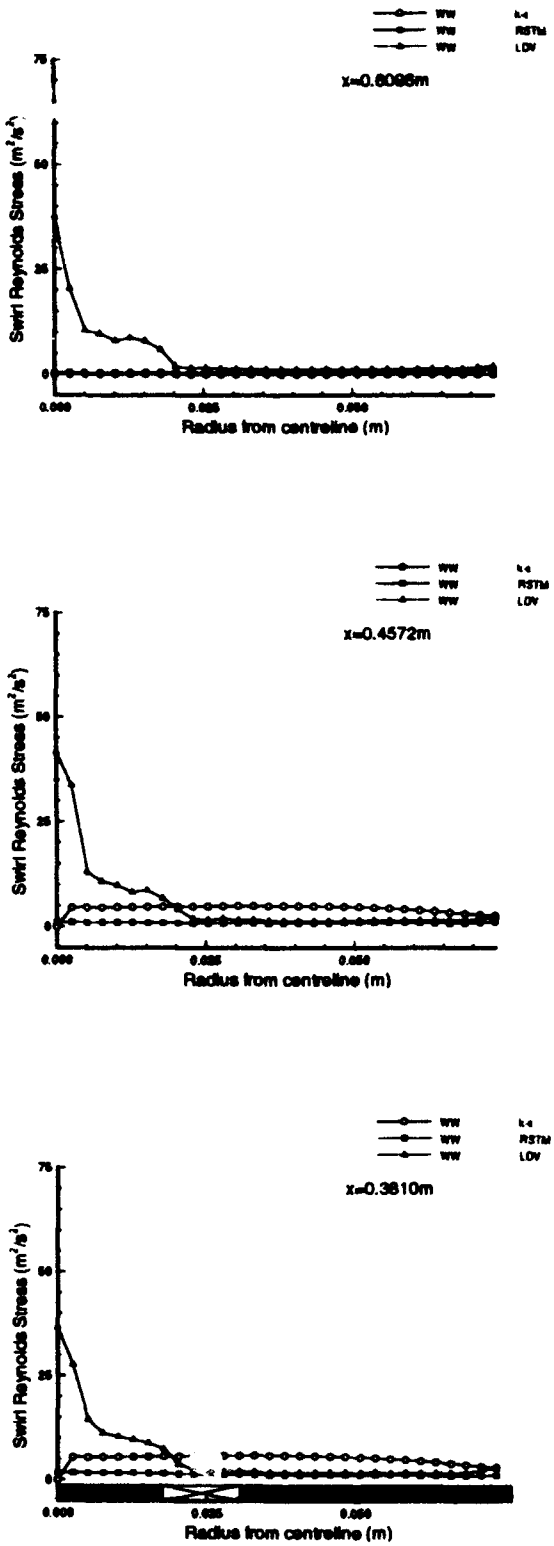

Figure 54c Measured vs. Predicted – Swirl Reynolds Stress Profiles

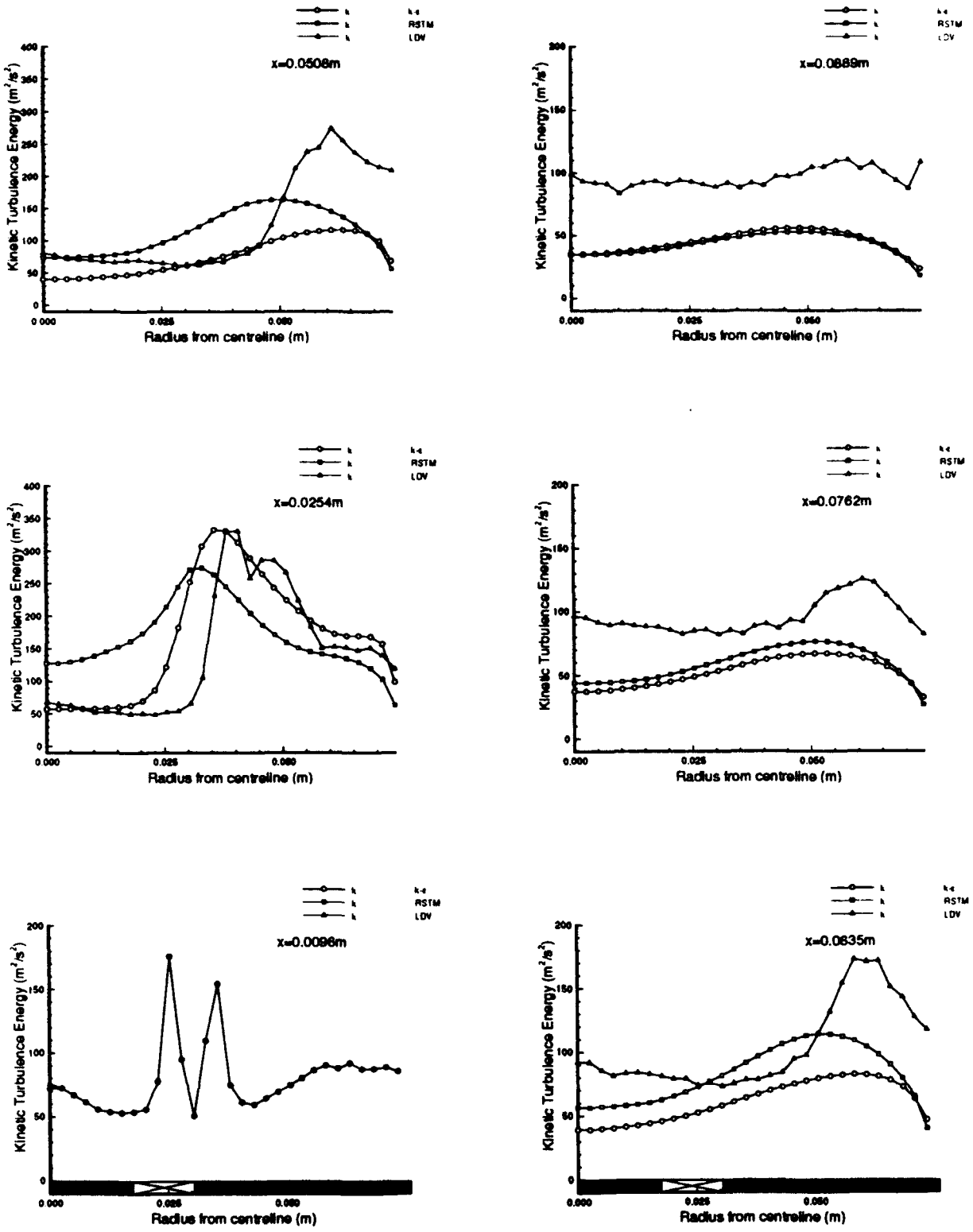

Figure 55a Measured vs. Predicted – Kinetic Turbulence Energy Profiles

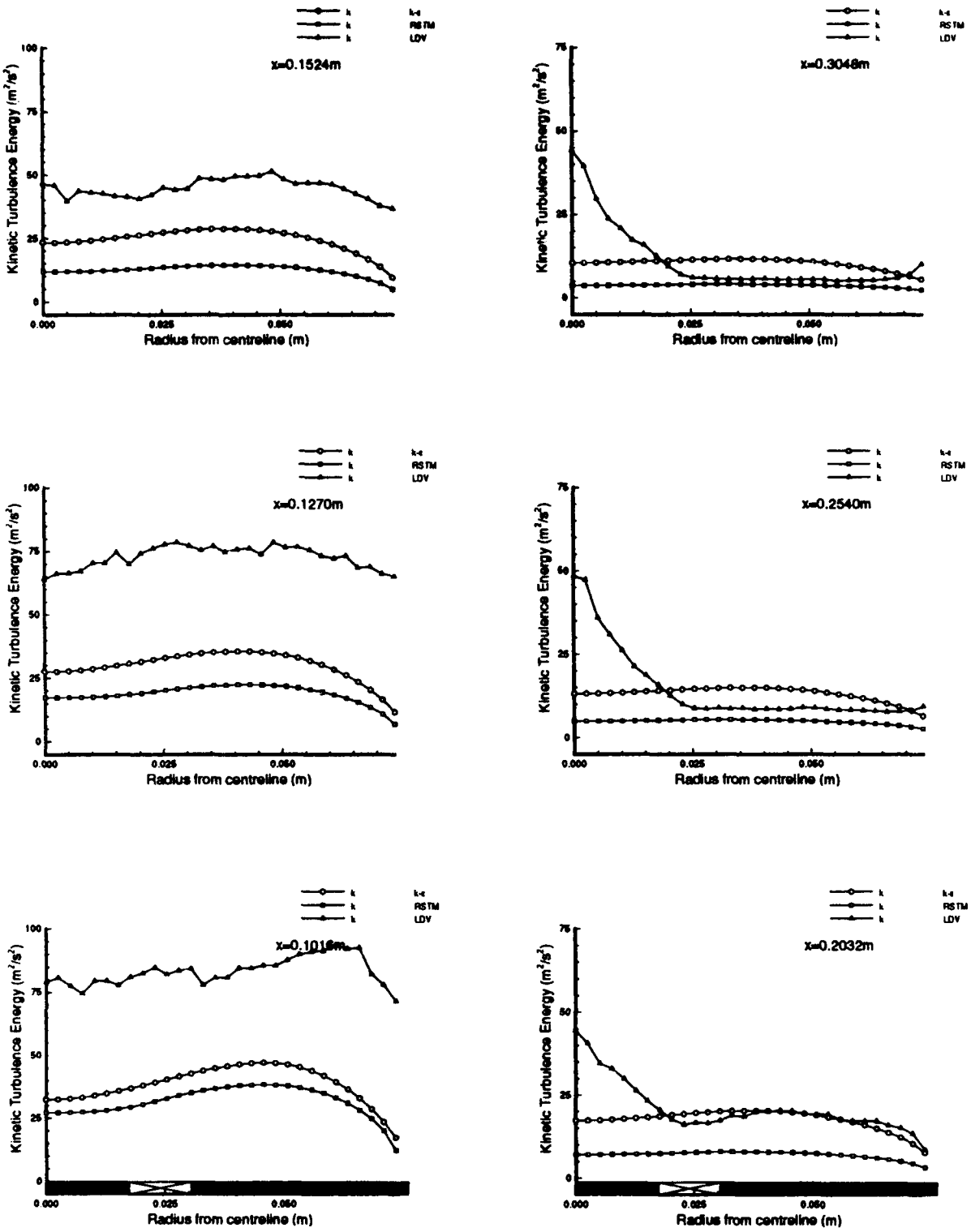

Figure 55b Measured vs. Predicted – Kinetic Turbulence Energy Profiles

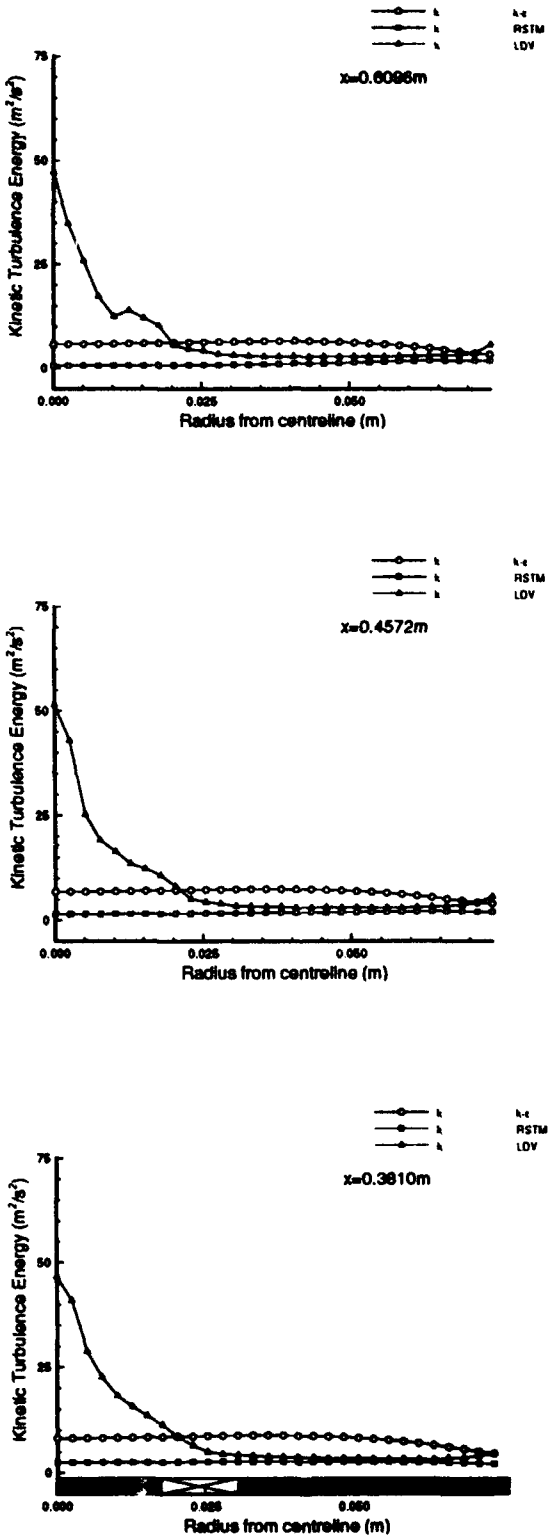

Figure 55c Measured vs. Predicted – Kinetic Turbulence Energy Profiles

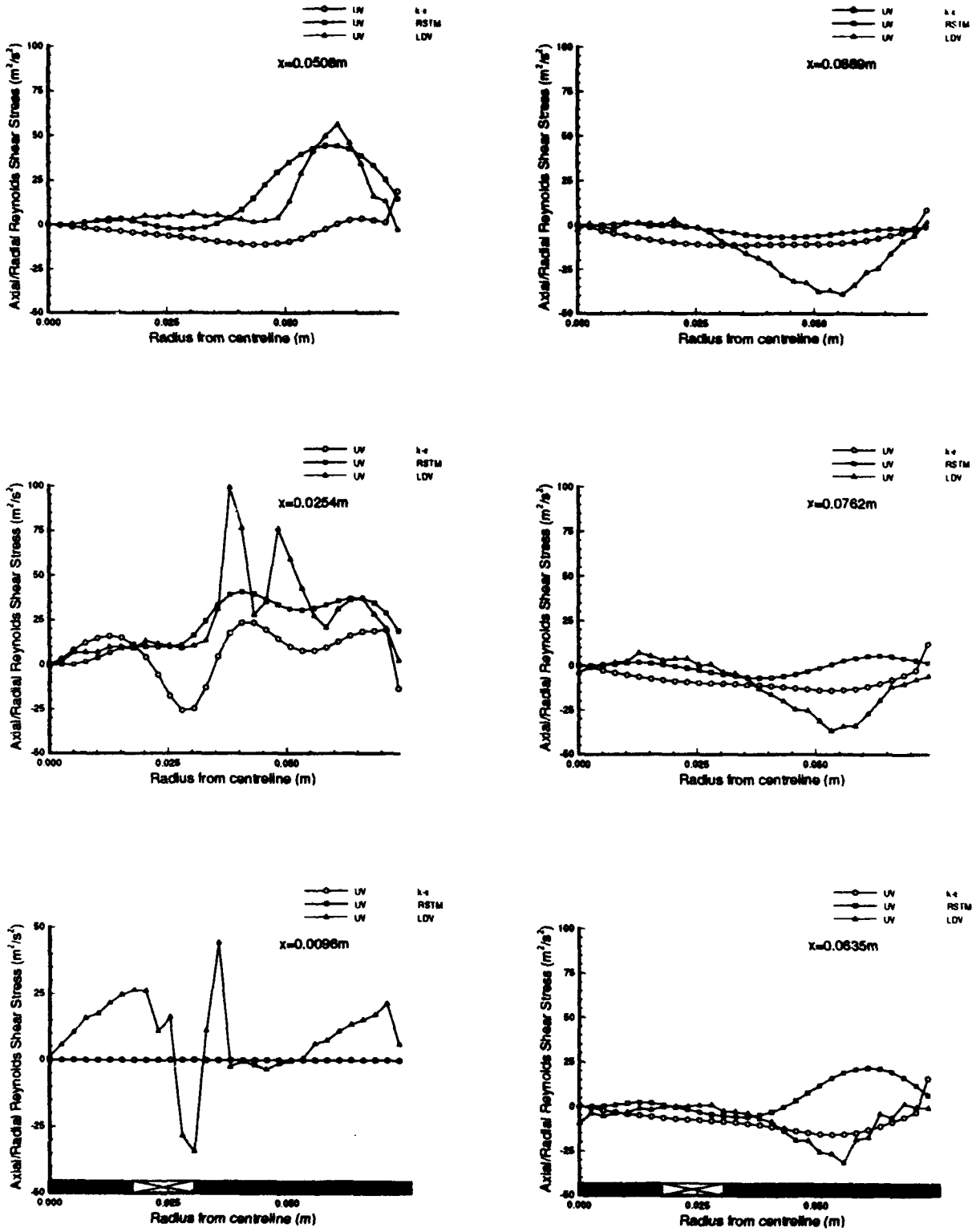

Figure 56a Measured vs. Predicted – Axial/Radial Reynolds Shear Stress Profiles

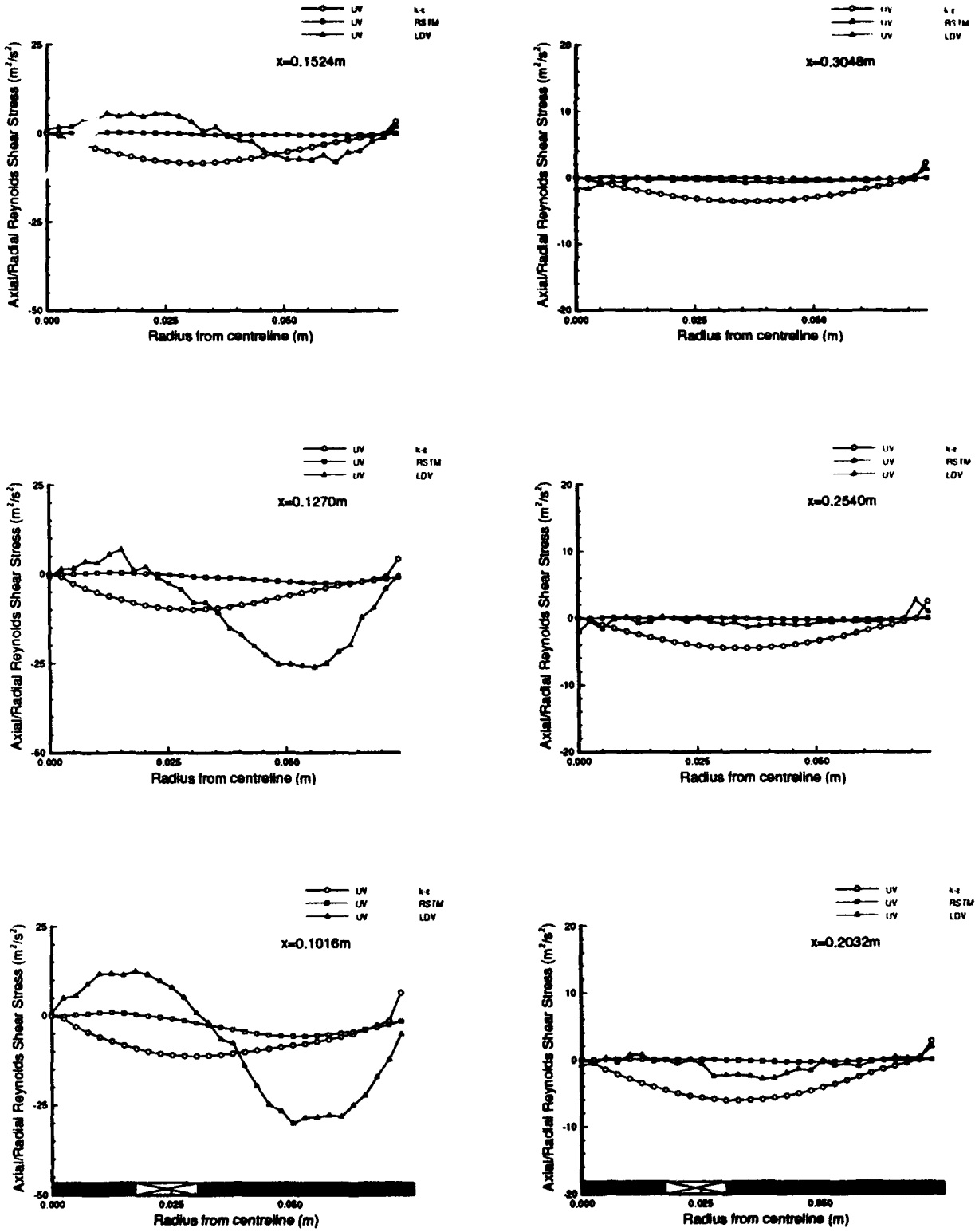

Figure 56b Measured vs. Predicted – Axial/Radial Reynolds Shear Stress Profiles

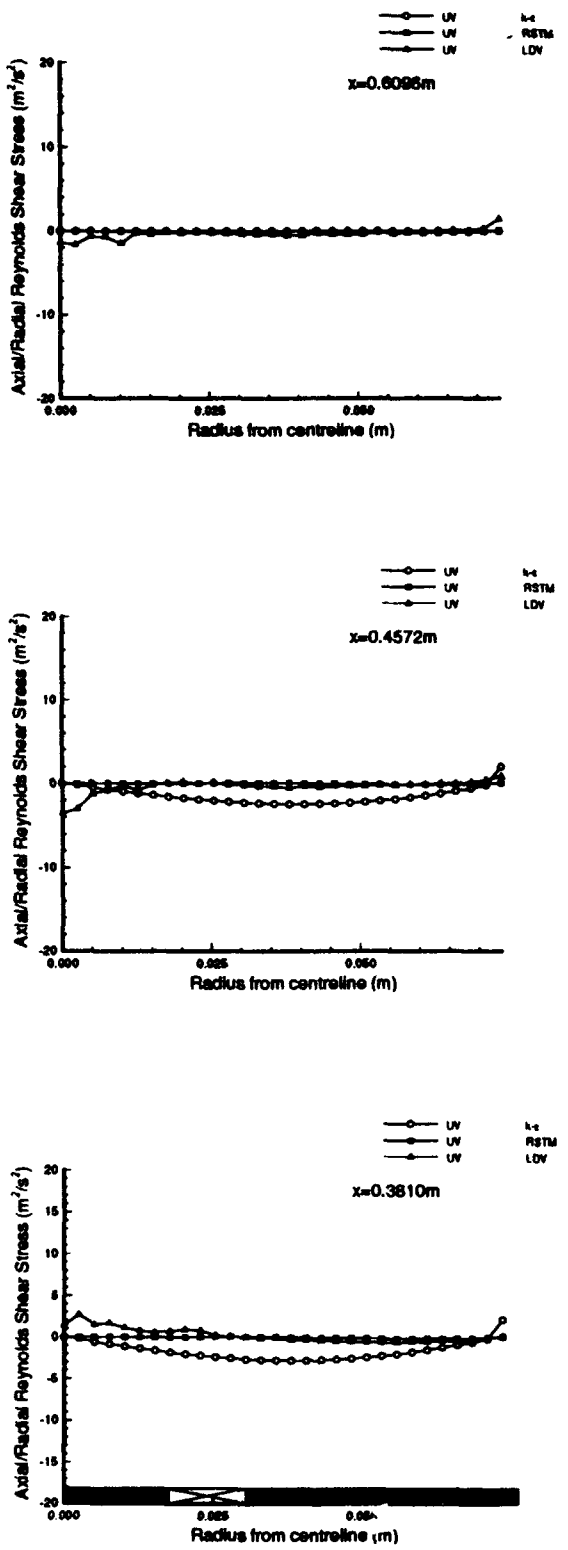

Figure 56c Measured vs. Predicted – Axial/Radial Reynolds Shear Stress Profiles

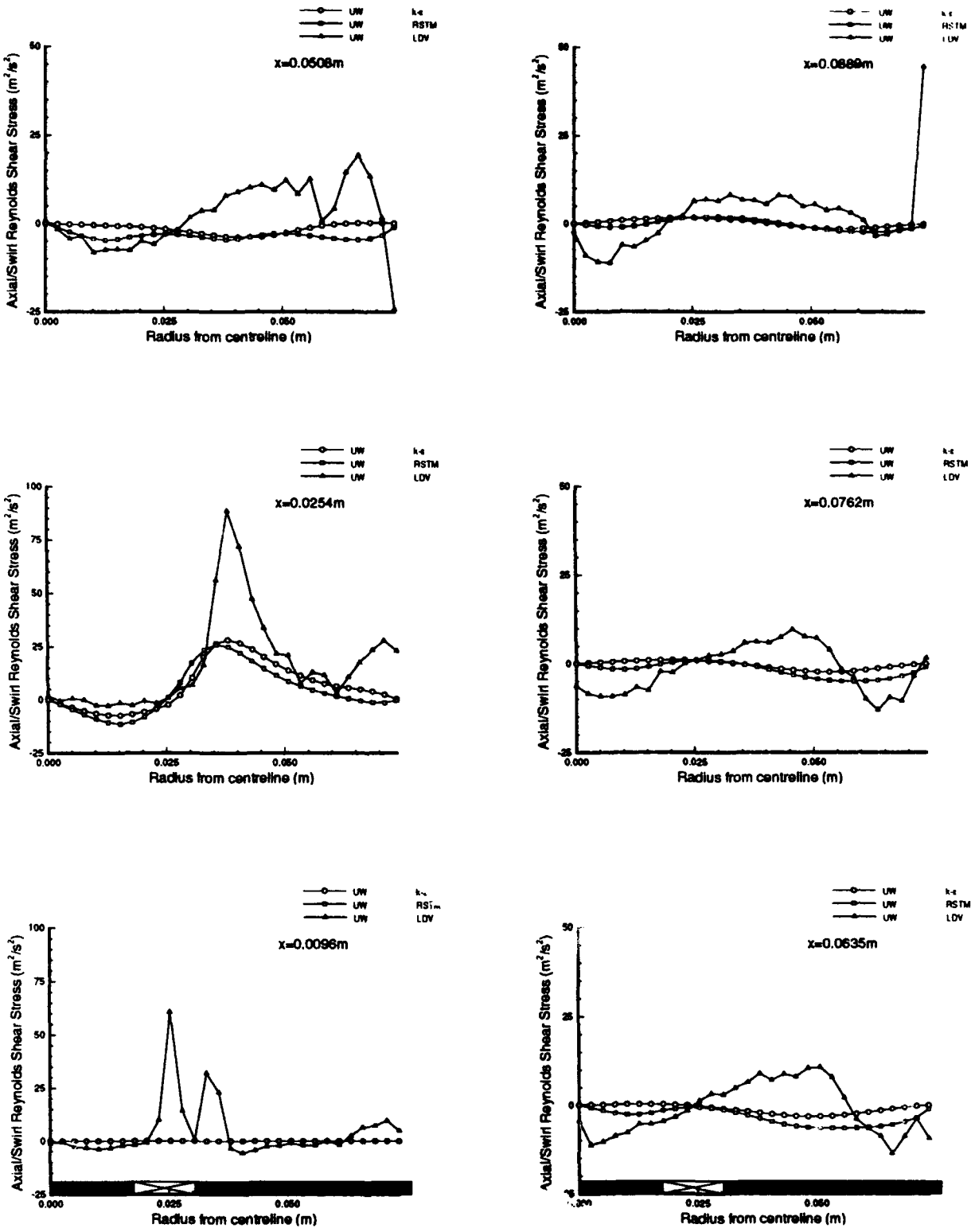

Figure 57a Measured vs. Predicted – Axial/Swirl Reynolds Shear Stress Profiles

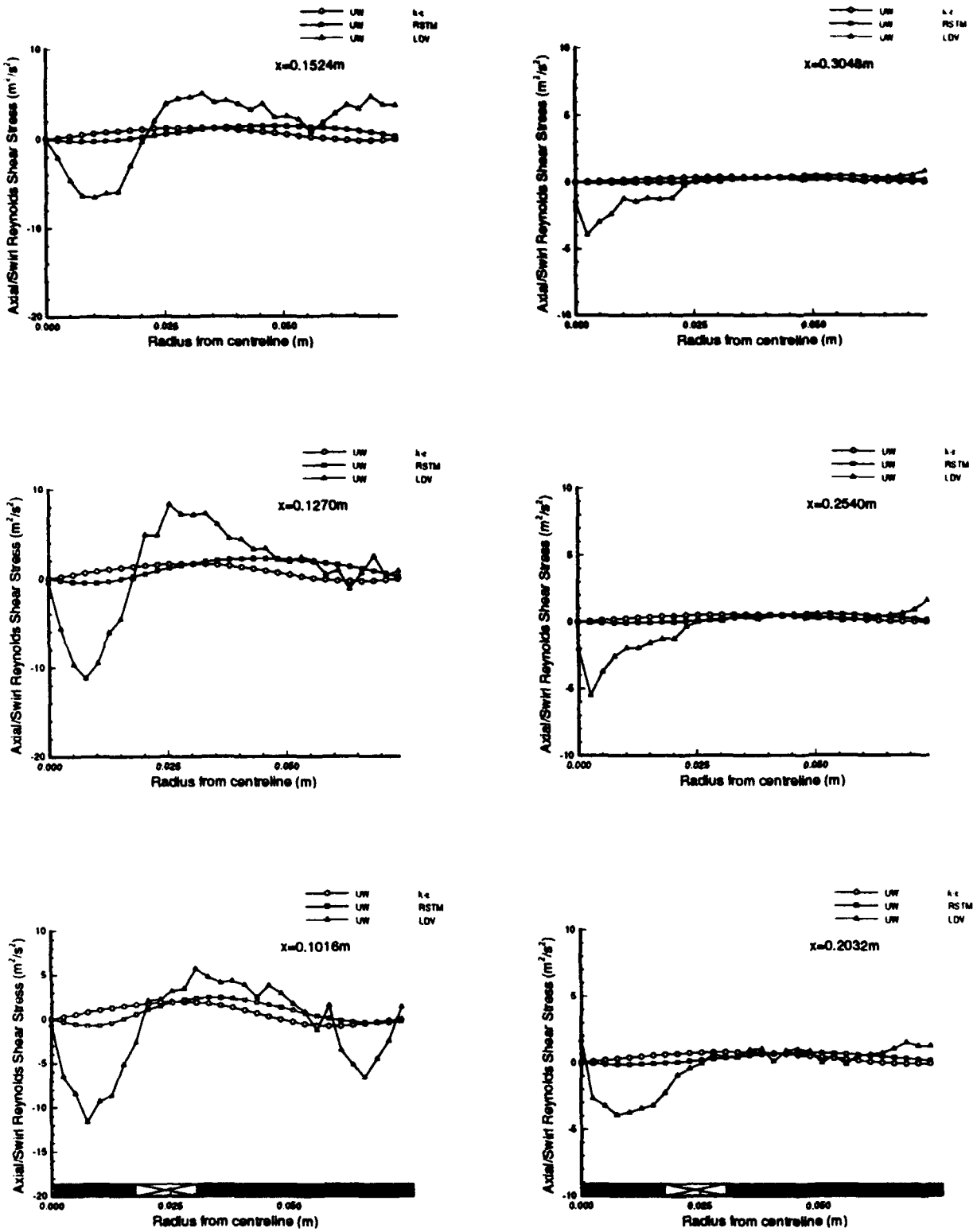

Figure 57b Measured vs. Predicted – Axial/Swirl Reynolds Shear Stress Profiles

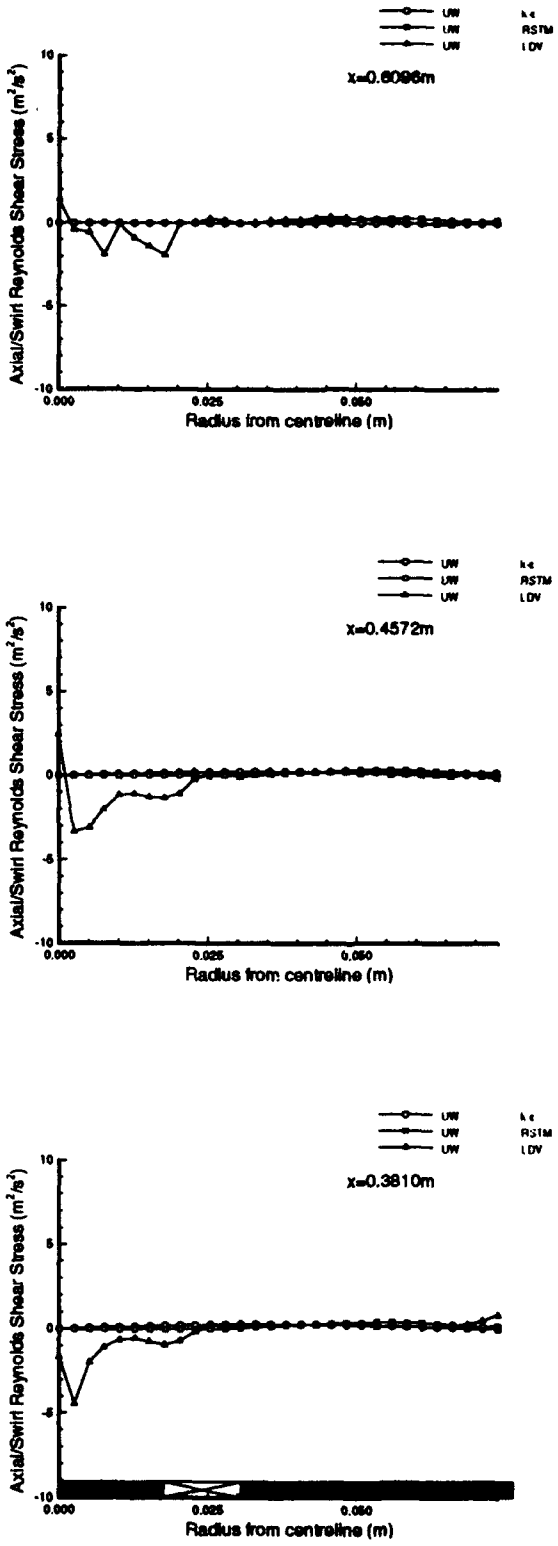

Figure 57c Measured vs. Predicted – Axial/Swirl Reynolds Shear Stress Profiles

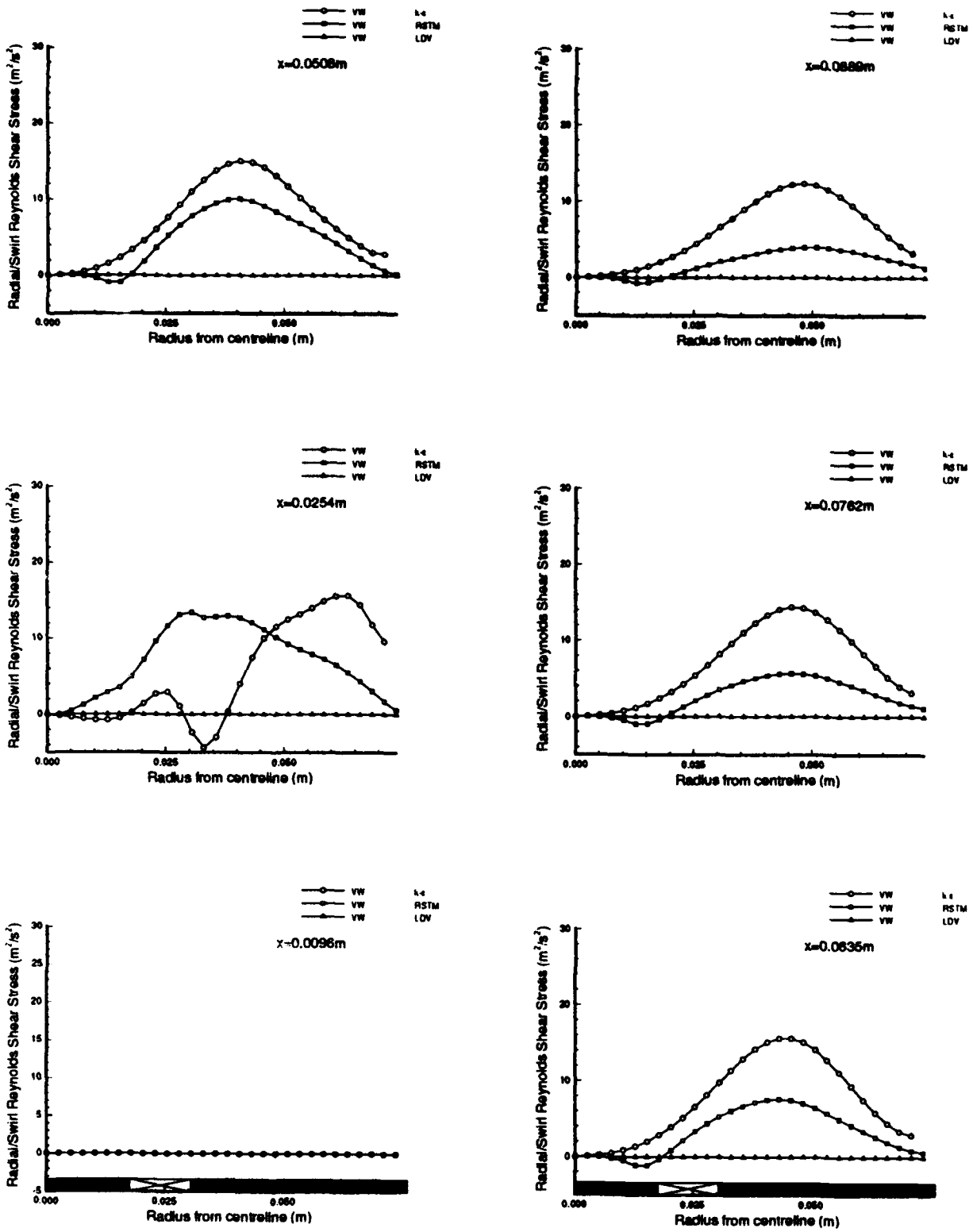

Figure 58a Predicted – Radial/Swirl Reynolds Shear Stress Profiles

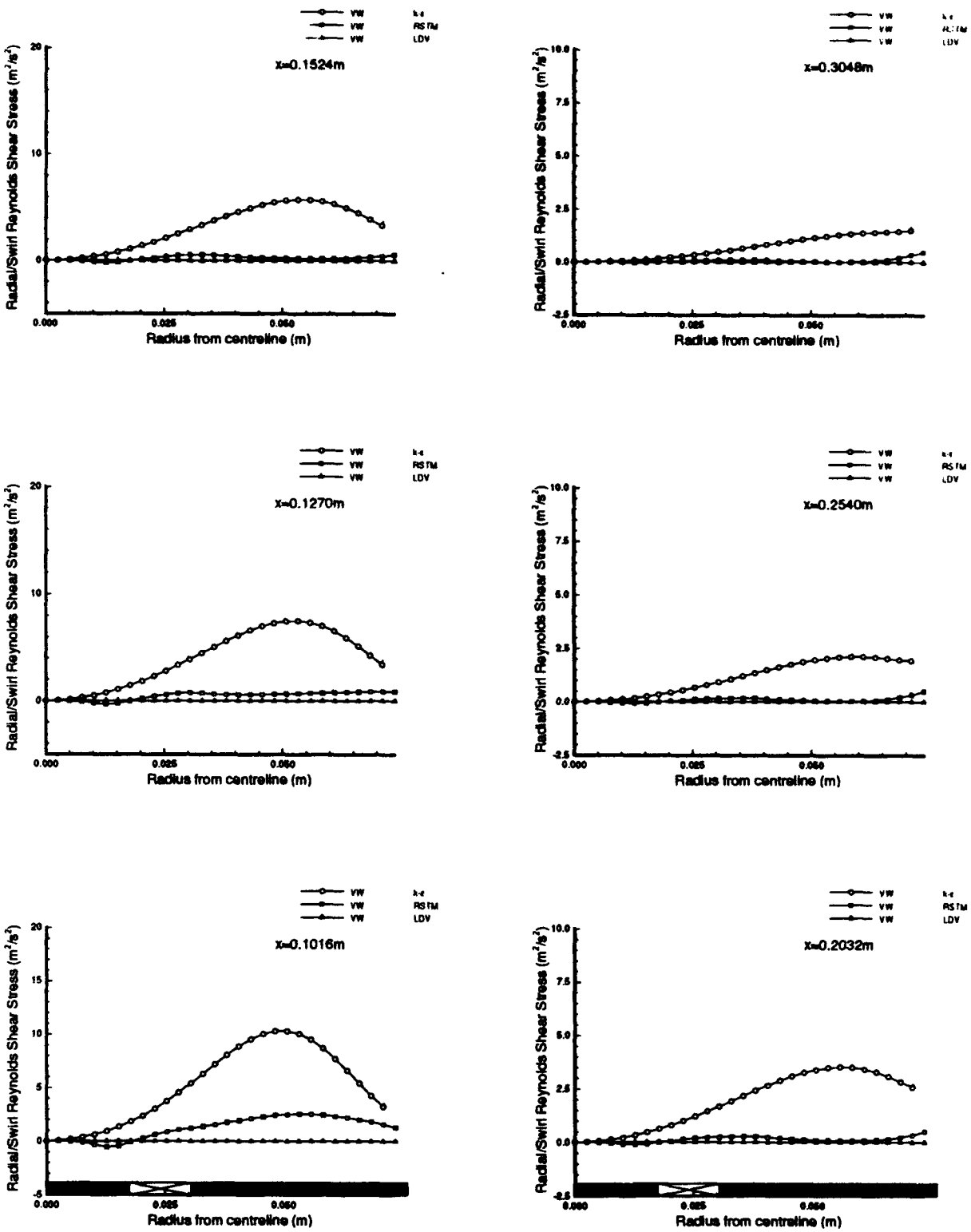

Figure 58b Predicted – Radial/Swirl Reynolds Shear Stress Profiles

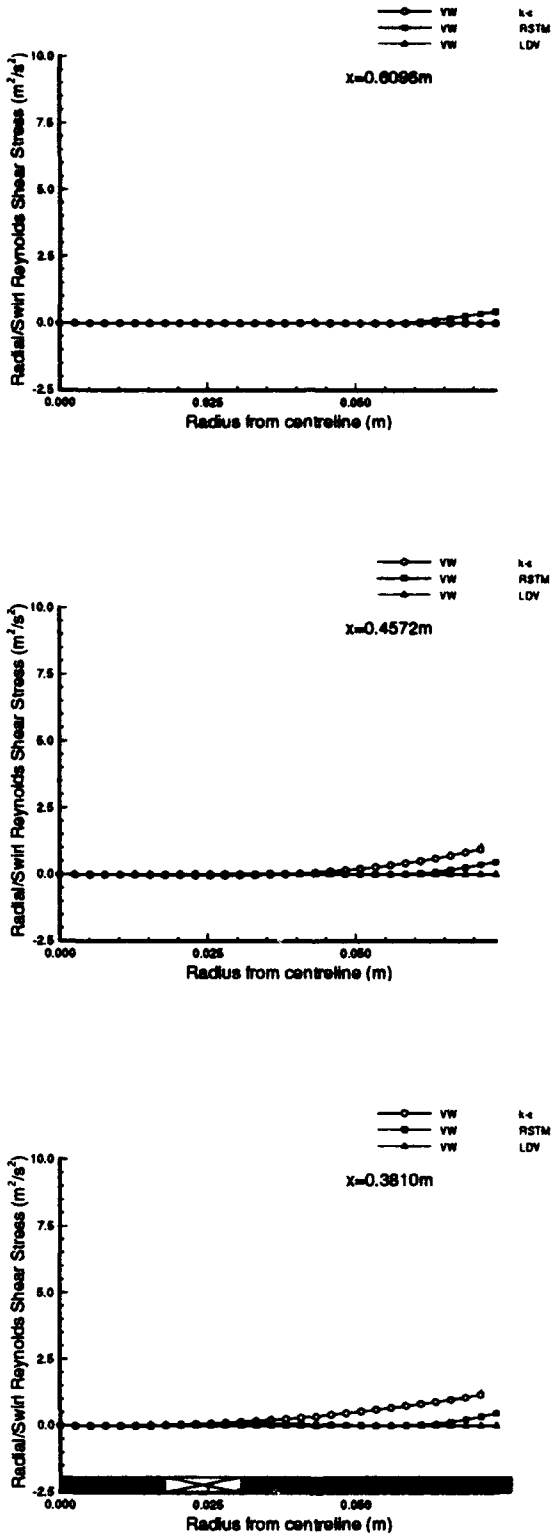

Figure 58c Predicted – Radial/Swirl Reynolds Shear Stress Profiles

☆U.S. Government Printing Office:1993—750-113/80535